UPPSALA
UNIVERSITET

Cold magnetospheric plasma flows: Properties and interaction with spacecraft

Licentiate Thesis
by

Erik Engwall
Department of Astronomy and Space Physics
Uppsala University
SE-75120 Uppsala, Sweden

March 10, 2006

Abstract

The ionosphere constantly loses matter to the surrounding magnetosphere through different outflow processes, and it is probably the main source of plasma supply to the magnetosphere. The ionospheric plasma has low energy and when flowing out from the Earth along diverging magnetic field lines, the density decreases. This will make the plasma ions difficult to detect with spacecraft, since the low density ensures a high spacecraft potential, which the low-energy ions will not be able to overcome. Therefore, only few observations of tenuous, cold plasma have been made, in spite of its abundance in the magnetosphere.

In this thesis, we present a new method for detecting and studying cold plasma with the double-probe electric field instrument EFW on the Cluster spacecraft. In cold flowing plasmas EFW observes a negatively charged spacecraft wake, which can be used to derive the flow speed of the cold plasma. The method has been verified for a case in the magnetotail at 18 R_{E} from the Earth, where a very special and unusual setup of the four Cluster spacecraft allowed simultaneous measurements of the ions with particle detectors. We have then applied the method for an initial statistical study of three months of Cluster data in the magnetotail lobes. The resulting flow parameters show agreement with previous measurements of ion outflow at lower altitudes, and the method opens up for observing cold flowing ions in regions where they previously have been inaccessible to spacecraft. To better understand the observed wake fields in EFW data, we have studied properties of enhanced wakes by numerical simulations, theoretical reasoning and data analysis. As an introduction to these new results, we have reviewed important measurements of cold magnetospheric plasmas, functioning of double-probe measurements, and spacecraft-plasma interactions, such as wake effects.

Erik Engwall
Department of Astronomy
and Space Physics,
Uppsala University
Box 515
SE-751 20 Uppsala
Sweden
`erik.engwall@irfu.se`

List of Papers

This thesis is based on the following papers:

Paper I

E. Engwall, A. I. Eriksson, J. Forest, *Wake formation behind positively charged spacecraft in flowing tenuous plasmas*, Phys. Plasmas, in review, 2006.

Paper II

E. Engwall, A. I. Eriksson, *Double-probe measurements in cold tenuous space plasma flows*, IEEE Trans. Plasma Sci., in review, 2006.

Paper III

E. Engwall, A. I. Eriksson, M. André, I. Dandouras, G. Paschmann, J. Quinn, and K. Torkar, *Low-energy (order 10 eV) ion flow in the magnetotail lobes inferred from spacecraft wake observations*, Geophys. Res. Lett., accepted, 2006.

iv

Contents

Chapter 1

Introduction

The light from the aurora has challenged the imagination of people of all times. This mainly green light emitted by excited atoms and molecules in the Earth's atmosphere can be seen as the messenger of phenomena occurring due to the interaction between the Sun and Earth. From the Sun a large amount of plasma, i.e. ionised gas, with high energy is constantly expelled out into the solar system. This is the *solar wind*. The Earth is protected from the solar wind mainly by its magnetic field, creating a shield around the Earth, called the magnetosphere. The solar wind and the magnetosphere are both highly dynamic regions, where a vast number of different processes occur, some of which creates the aurora.

The current knowledge of the processes in the magnetosphere, the solar wind and the areas in between, can to a large extent be attributed to the large number of scientific satellites, launched during the past 30 years[1]. All new experimental results presented in this thesis are based on measurements from the Cluster II mission, which is one of today's most ambitious projects, with four satellites flying in formation to explore some of the key regions in the near-Earth space. In our work, we have mainly used measurements from the two Cluster electric field instruments, and especially from the *Electric Fields and Waves instrument* (EFW) (*Gustafsson et al.*, 2001), which measures potential differences between two spherical probes.

A scientific spacecraft will always more or less affect the plasma environment it is sent out to investigate, since spacecraft interact with the surrounding plasma. One important example of spacecraft-plasma interaction is that spacecraft can charge to high negative potentials, which disturbs the electric fields in the plasma. Moreover, the spacecraft charging can be hazardous for the spacecraft itself, since uneven charging between different electrical elements of the spacecraft might lead to discharges possibly destroying critical systems on the spacecraft. Most magnetospheric spacecraft, like Cluster, will not experience such problems, as they are constructed with conductive surfaces and charge to positive potentials of the order of a few tens of volts because of photoelectron emission. However, this positive spacecraft potential makes it difficult to measure low-energy ions with energy less than the equivalent energy of the spacecraft potential, since these ions will not be able to climb the potential barrier. This is the case for cold, tenuous magnetospheric plasmas.[2] The ionosphere, which is the upper part

---

[1]Ground based measurements have also been of great importance for the exploration of the near-Earth space.

[2]In this thesis, we define *cold* as temperatures on the order of a few eV and *tenuous* as densities on

of Earth's atmosphere, is supposed to be the main source of magnetospheric plasma and the cold plasma in the magnetosphere is certainly of ionospheric origin *Chappell et al.* (1987); *Chappell et al.* (2000). To understand the plasma transport, as well as heating mechanisms in the magnetosphere, it is therefore important to study these cold plasmas. However, due to the positive potential on sunlit magnetospheric spacecraft few reliable observations of cold magnetospheric plasmas have been made.

Another spacecraft-plasma interaction problem is negatively charged wakes forming behind spacecraft in motion with respect to the plasma. These wakes may under certain circumstances grow big for positive spacecraft potentials and create large spurious electric fields, which has been observed in Cluster EFW data (*Eriksson et al.*, 2006a). Even though, in the beginning only seen as a contamination to the real electric field measurements, the wake spurious electric field can be used to detect and derive the flow velocity cold magnetospheric plasmas. Information on the functioning of probes and double-probe instruments, as well as how the wakes form is essential to understand these methods.

This thesis consists of two parts: a few introductory chapters accompanied by three scientific papers. Chapter 2 gives first an introduction to our space environment and some basic properties of a plasma. The rest of the chapter contains a more extensive treatment of observations and mechanisms for supply of cold magnetospheric plasmas. The starting point in chapter 3 is basic probe theory containing a detailed treatment of the currents to a probe in a plasma. Further, we examine the use of probes in different plasma instruments, focusing mostly on the operations and possible complications of double-probe instruments for measurements of electric fields. Chapter 4 treats two important phenomena of spacecraft-plasma interactions: spacecraft charging and wake effects. In chapter 5 we move on to the wake effects experienced by the EFW instrument on Cluster, starting with some general information on the Cluster spacecraft and their electric field instruments. In chapter 6, we present our new method for deriving the flow velocity of cold ions with electric field instruments, and show results for an initial statistical study of cold ions using this method. Finally, chapter 7 summarizes the three papers. The first paper (*Engwall et al.*, 2006b) treats the formation of enhanced wakes behind spacecraft, including numerical simulations and theoretical reasoning. The second paper (*Engwall and Eriksson*, 2006) includes detailed data analysis of the wake field detected by EFW. In the third paper (*Engwall et al.*, 2006a) we report cold ions in the magnetotail detected by two methods: (1) direct measurements with an ion detector, and (2) measurement of the wake electric field by EFW.

---

the order of tenths of cm^{-3}.

Chapter 2

Space plasma

2.1 The space environment

Space and phenomena in the sky have fascinated mankind for millennia. With the invention of the telescope and its further development, discoveries revealing some of the mysteries of our solar system, galaxy and the whole universe have been made. Nevertheless, it was not until the satellite era, which started with the launch of the Soviet satellite Sputnik 1 in 1957, that it was possible to explore the near-Earth space environment in detail. An adequate description of this environment is necessary to understand such a common and relatively close phenomenon as the aurora borealis. This section is intended to give a brief introduction to the space environment around us. For a more detailed description, books on space physics, for example *Kivelson and Russel* (1995), *Parks* (1991) and *Gombosi* (1998), are recommended.

The existence of the Sun is necessary, either directly or indirectly, for all life on Earth. As everybody knows, energy is transported from the Sun in form of electromagnetic radiation, which among others will give us enough heat and light and allow plants to grow. What is less known, is that as much as 1% of the energy from the Sun reaching the Earth is in form of charged particles (*Sandahl*, 1998). The Sun does, in fact, not only emit light, but also a high-speed stream of particles, at a rate of 1 million tons/s. This stream of plasma is called the *solar wind*. The solar wind plasma originates in the outer layers of the Sun, thus consisting mostly of protons, electrons and a small amount of helium ions. Some of these particles will eventually reach the Earth, but this is only a tiny fraction of all the particles in the solar wind, since the Earth is shielded by its magnetic field. This magnetic shield protects us from the highly energetic solar wind plasma, which has an average speed of 450 km/s and temperature of 100 000 K.

The solar wind is deflected around the Earth's magnetic field, compressing it in the sunward direction and extending it in the anti-sunward direction (see figure 2.1). Since the solar wind is supersonic at the orbit of the Earth, a shock wave will form around the Earth reducing the speed of the solar wind plasma to subsonic values. This happens at the *bow shock*. Shocked solar wind particles continue into the *magnetosheath*, where they are re-accelerated to supersonic flow velocities. The *magnetopause* is the border to the Earth's *magnetosphere*, which is the region dominated by the Earth's magnetic field. The solar wind experiences difficulties to enter the magnetosphere through the magnetopause. However, in the *cusp* regions the magnetic field lines of the solar wind

are connected to the Earth's magnetic field, which will allow solar wind plasma to penetrate the magnetosphere. The *magnetotail* is a cold tenuous region in the magnetosphere, extending from the dusk side of the Earth far out into the solar wind. Also in the *plasma sheet* the plasma density is low, but here the particle energies are high, making the plasma hot. The *plasmasphere* is the torus-shaped region closest to the Earth with a cold dense plasma. Above the geomagnetic poles, the *polar caps* are found. They are bounded by the auroral regions, where the aurora[1] appears, when charged particles (mostly electrons) from the magnetosphere enter the atmosphere of the Earth and collide with atoms and molecules, typically at an altitude of 100 km. In the collisions, the atmospheric atoms and molecules will be excited, and when de-excited, light will be emitted. This light can be seen in the sky at clear nights.

Current theories suggest that most of the plasma in the magnetosphere originates from the ionosphere (*Chappell et al.*, 1987; *Chappell et al.*, 2000). If the ionospheric plasma is sufficiently energised, it can escape into the magnetosphere by several different processes. An example of such a process is the *polar wind*, which is an up-flowing stream of ionospheric plasma along the open geomagnetic field lines in the polar cap. In section 2.3, we examine the different mechanisms of supply of ionospheric plasma, which is cold, to the magnetosphere.
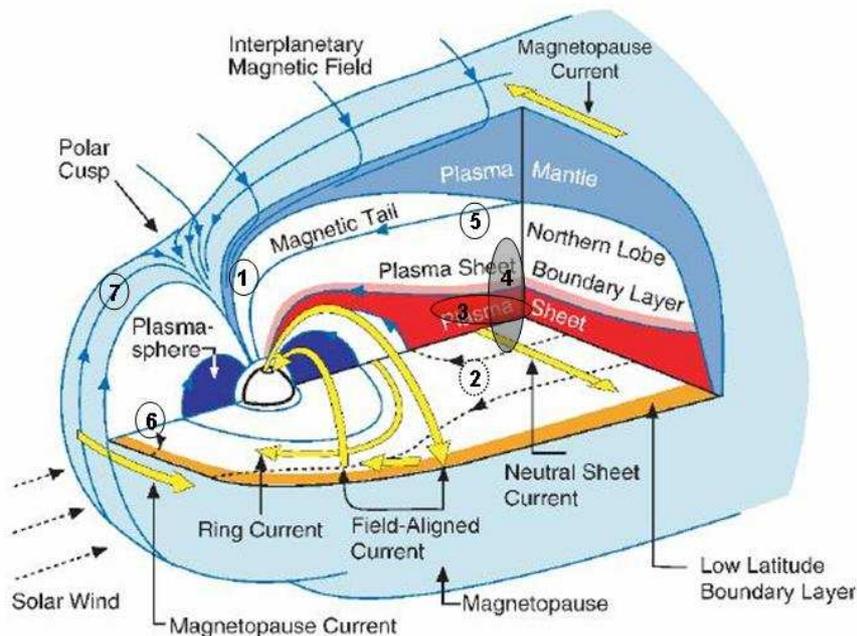
Figure 2.1: Schematic view of the magnetosphere. The numbers correspond to seven different observations of cold magnetospheric plasma presented in section 2.3.2. (Dashed ellipses represent observations in the southern hemisphere.) 1. High altitude polar wind studied by *Su et al.* (1998), *Moore et al.* (1997) and *Chappell et al.* (2000). 2-4. Cold plasma in the magnetotail observed by *Etcheto and Saint-Marc* (1985), *Seki et al.* (2003) and *Sauvaud et al.* (2004). 5. Cold ions in the magnetotail lobes studied by *Engwall et al.* (2006a). 6-7. Studies of cold plasma populations in the dayside magnetosphere by *Chen and Moore* (2004) and *Sauvaud et al.* (2001). (Original figure adapted from *Kivelson and Russel* (1995).)

---

[1]The aurora is often referred to as the northern lights or polar lights.

2.2   Properties of a plasma

Plasma is the dominating state of matter in the universe, estimated to comprise around 99% of all observable matter. The lower part of the Earth's atmosphere is one of the few exceptions, where plasma does not play an important role. Because of this abundance of plasma in the universe, we will need knowledge in plasma physics to understand phenomena in space. Even a short comprehensive summary of the theory of plasma physics is beyond the scope of this thesis[2]. However, we need to know some basic principles for the study of cold magnetospheric plasmas and its interaction with spacecraft.

One important feature of a plasma is that it will exhibit *collective behaviour*, which means that the plasma particles will be governed by the long-range electromagnetic forces instead of collisions like in a normal gas. The phenomenon of *Debye shielding* is a fundamental property of a plasma and gives an example of collective behaviour. When a charged object is immersed in a plasma, the potential around it will be shielded out by either the ions or the electrons. A positively charged object will namely attract a cloud of electrons, while a negatively charged object will be enclosed in an ion cloud. If the plasma is cold, the shielding will be perfect outside the cloud. For warmer plasmas, however, the small potentials at the edge of the clouds, will not be able to prevent the electrons or ions from escaping. To get a notion of the size of the shielding cloud, we introduce the *Debye length*, which is a characteristic length for the shielding of the potential around a charged object. The Debye length, λ_D, is defined by the expression

$$\lambda_D = \sqrt{\frac{\epsilon_0 K T_e}{n q_e^2}}, \tag{2.1}$$

where ϵ_0 is the constant of permittivity, K the Boltzmann constant, T_e the electron temperature, n the plasma density[3] at infinity and q_e the electron charge. It is worthwhile to note that the Debye length will increase when the temperature increases, which can be explained by the fact that the augmentation of the thermal motion of the plasma particles will make the shielding weaker. Conversely, a dense plasma will make the Debye length shorter, as there are more particles to shield out the potential. A criterion for a plasma is that it is *quasineutral*. This is fulfilled when the dimensions of the physical system are much larger than the Debye length, since every local concentration of charge will be shielded in a distance much smaller than the size of the system.

Considering only the individual plasma particles, we can find some useful relations for their motion in electromagnetic fields, here taken to be constant both in time and space. The equation of motion for a particle with mass m_α, charge q_α and velocity $\boldsymbol{v}_\alpha$ under the influence of an electric field $\boldsymbol{E}$, and a magnetic field $\boldsymbol{B}$ is given by

$$m_\alpha \frac{d\boldsymbol{v}_\alpha}{dt} = q_\alpha(\boldsymbol{E} + \boldsymbol{v}_\alpha \times \boldsymbol{B}) \tag{2.2}$$

If the electric field is zero ($\boldsymbol{E} = \boldsymbol{0}$) and $\boldsymbol{v}_\alpha$ is perpendicular to $\boldsymbol{B}$, equation 2.2 only describes a circular motion with the Lorentz force as the central force ($\boldsymbol{F_c} = q_\alpha \boldsymbol{v}_\alpha \times \boldsymbol{B}$).

---

[2] *Chen* (1984) gives a good introduction to plasma physics and is used as the main reference for this section.

[3] The plasma density is expressed in particles per unit volume.

The angular frequency of this motion is the *cyclotron angular frequency*, $\omega_c = \frac{|q_\alpha \boldsymbol{B}|}{m_\alpha}$, and the radius is the *Larmor radius*, $r_L = \frac{v_{\alpha,\perp}}{\omega_c}$. If the velocity has a component along the magnetic field, the particle will move in a spiral. The projection of the motion onto the plane perpendicular to $\boldsymbol{B}$ will, however, still be a circle with the same centre as before. For non-zero electric fields the particle will drift with a velocity $\boldsymbol{E} \times \boldsymbol{B}/B^2$, thus in a direction perpendicular to both the electric and magnetic fields.

An interesting property of a moving plasma is that, for slow time variations, the magnetic field lines follow the plasma motion, and they are thus referred to as *frozen-in field lines*. The volume bounded by a set of field lines is called a flux tube, and the frozen-in condition implies that particles initially linked to a certain flux tube remains fixed to it throughout the plasma motion. The frozen-in condition is satisfied if the plasma motion can be approximated by

$$\boldsymbol{E} + \boldsymbol{v} \times \boldsymbol{B} \approx 0, \tag{2.3}$$

where $\boldsymbol{v}$ is the velocity of the plasma, which will be equivalent to the single particle drift for non-zero electric fields, $\boldsymbol{E} \times \boldsymbol{B}/B^2$. For many applications in space physics, such as the description of plasma convection in the magnetosphere, the frozen-in condition is a very useful approximation.

Because of the electromagnetic properties of plasma, different types of oscillations will arise. The simplest type are the *plasma oscillations*. The light electrons will, because of their inertia, oscillate back and forth against a uniform background of massive immobile ions, with a characteristic frequency, the *plasma frequency*. The plasma frequency, ω_{pe} is given by

$$\omega_{pe} = \sqrt{\frac{n_0 e^2}{\epsilon_0 m}} \tag{2.4}$$

The quantity ω_{pe}^{-1} is often chosen as a characteristic time scale for plasmas.

2.3   Cold plasma in the magnetosphere

2.3.1   Mechanisms for supply of cold magnetospheric plasmas

The cold plasma in the magnetosphere is mainly of ionospheric origin. Ionospheric plasma has low energy, and if it is permitted to escape into the magnetosphere without significant heating, it will remain cold. The total outflow of ions from the ionosphere is estimated to approximately 1 kg/s. These outflows can be divided into two types (*Yau and André*, 1997):

1. Bulk ion outflows

2. Energisation processes where only a fraction of the ions are energised

Ion energisation processes include for example transversely accelerated ions, ion conics and ion beams. In these processes only a fraction of the ions participate in the

outflow. This is in contrast to the bulk ion outlows, where the whole particle distribution is moving. These outflows can thus contribute significantly to the population of cold magnetospheric plasma. The polar wind is an example of bulk ion outflow along magnetic field lines above the polar caps. However, bulk ion outflows occur at all latitudes; e.g. outflows of thermal O^+ in the topside auroral ionosphere, and the filling of the plasmasphere are both due to such processes. The bulk ion outflows are strongly dependent on the solar wind properties and the interplanetary magnetic field (*Cully et al.*, 2003).

Beside bulk ion outflows, the plasmasphere is an important supply of cold plasma to the rest of the magnetosphere. The plasmasphere is directly connected to the ionosphere and is thus filled with cold, dense plasma. At *plasmasphere detachments*, a part of the plasmasphere is ripped away and cold plasma is lost to the magnetosphere.

Polar wind

The polar wind, named after its similarities to the solar wind, was theoretically predicted by *Axford* (1968) and *Banks and Holzer* (1968) by arguing that the light ions in the ionosphere are too energised to be bound by gravity. The outflow is driven by the gradient in the electron pressure, which makes the electrons move upward. To maintain charge neutrality, an ambipolar electric field is built up and the ions are dragged upward along with the electrons. Thus, a larger outflow of electrons automatically gives rise to a larger outflow of ions. This is evident for example in the polar wind on field lines connecting to the sunlit ionosphere, where the outflows are significantly larger than on the nightside, due to escaping photoenergised atmospheric electrons (*Yau and André*, 1997; *Moore et al.*, 1999).

Auroral Bulk outflows

The outflows from the auroral regions are driven by the same processes as the polar wind. However, in these regions the ions are more strongly accelerated, as a result of parallel electric fields and particle-wave interactions (*Moore et al.*, 1999). Due to the acceleration, heavy ions are also allowed to escape from the ionosphere and the outflow contains a significant, if not dominant, fraction of O^+ (*Yau and André*, 1997; *Moore et al.*, 1999). The upflowing ions originating in the dayside auroral regions, *the cleft*, will be transported tailward by antisunward convection. This motion of ions forms the *cleft ion fountain* (*Lockwood et al.*, 1985).

Plasmasphere detachment

Cold dense plasma is at times observed in the dayside outer magnetosphere and at geosynchronous orbits. This plasma is released from the corotating plasmasphere at high geomagnetic activity and convected sunward and westward toward the magnetopause (see figure 2.2), forming the *detached plasmasphere* (or *plasmaspheric tail*). The detachment occurs in connection to increases of the dawn-to-dusk convection electric field in the magnetosphere, which together with the corotation electric field confines the plasma in the plasmasphere (*Matsui et al.*, 1999).
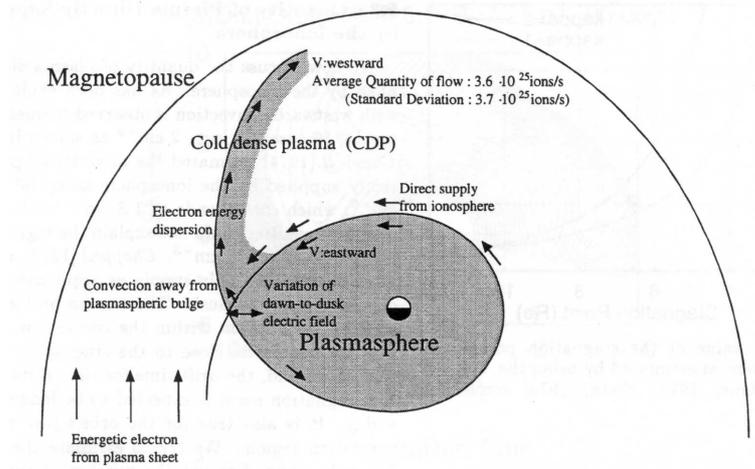
Figure 2.2: Schematic picture of a plasmaspheric detachment. (Adapted from *Matsui et al.* (1999).)

2.3.2 Observations of cold flowing plasmas in the magnetosphere

Observations of cold space plasmas with energies on the order of a few eV often encounter difficulties. The problems occur especially in low-density regions, where the spacecraft potential can reach several tens of volts (see section 4.1). Low-energy ions will be shielded out by the potential barrier and will never be able to reach any ion detector mounted on the spacecraft. This leads to the conclusion that there may exist a much larger fraction of cold plasma in the magnetosphere than has been revealed by previous and current spacecraft missions. In this section, we will investigate some important observations, where the geophysical setting or the spacecraft setup has allowed detection of cold plasmas in different regions of the magnetosphere. Figure 2.1 summarises where these observations have been carried out. References to other investigations of cold ions can be found in the introduction of Paper III (*Engwall et al.*, 2006a).

Polar regions

Measurements of the polar wind have indeed been problematic, due to its tenuous cold plasma. The first direct measurements of the polar wind was achieved in the late 1960's by Explorer 31, which found H^+ outflows at 500 and 3000 km with velocities up to 15 km/s (*Hoffman*, 1970). ISIS 2 confirmed the outflow of H^+, but also found evidence for outflows of He^+ and O^+. Oxygen was shown to be the dominant ion species at the satellite altitude (1400 km) during magnetically quiet times (*Hoffman et al.*, 1974; *Hoffman and Dodson*, 1980). The measurements from both Explorer 31 and ISIS 2 were carried out at low altitude, where the densities were high and thus the spacecraft potentials low. Contributions to the understanding of the polar wind have also been made by DE 1 (*Nagai et al.*, 1984). The current knowledge of the polar wind can mainly be attributed to studies by Akebono (*Abe et al.*, 1993, 1996) and Polar (*Su et al.*, 1998; *Moore et al.*, 1997; *Chappell et al.*, 2000). The Polar spacecraft was launched in 1996 into a polar ecliptical orbit with 9 R_E apogee (northern hemisphere) and 1.8 R_E perigee (southern hemisphere). Polar carries the ion detector TIDE (Thermal Ion Dynamics Experiment), which operates with good resolution in the 0.3-450 eV

energy range. Together with the Plasma Source Instrument (PSI), which reduces the spacecraft potential to approximately +2 V by creating a plasma cloud around the spacecraft, TIDE is able to measure low-energy ions. These two instruments have shed new light on the dynamism and composition of the polar wind at different altitudes, and also confirmed the existence of the high-altitude polar wind (*Moore et al.*, 1997).

Su et al. (1998) used Polar data to study the polar wind at two different altitudes: 8 R_E (apogee, northern hemisphere) and 5000 km (perigee, southern hemisphere). Figure 2.3 illustrates the observed characteristics of the high altitude polar wind. These polar wind observations reveals a faster, hotter and more rich in O^+ plasma than predicted by thermal outflow theories. The discrepancy between theory and observations was interpreted as a result of neglecting energy input in the topside auroral ionosphere (*Moore et al.*, 1999). At 5000 km, the H^+ are outflowing, but the mean velocity of O^+ is directed downward (see figure 2.4). The high altitude O^+ can thus not originate from the polar cap proper, but are transported into the polar cap from the dayside auroral zone by the cleft ion fountain (see section 2.3.1). Parts of the ion distribution are again trapped in the Earth's gravity field over the polar caps and flow downward.

The polar wind survey by *Su et al.* (1998) revealed the following parameters of the polar wind:

Density At 5000 km the dominant ion species is O^+ ($n_{\mathrm{O^+}} \approx 8$ cm^{-3}, $n_{\mathrm{H^+}} \approx 2$ cm^{-3}), whereas at 8 R_E the plasma is totally dominated by H^+ ($n_{\mathrm{O^+}} \approx 0.05$ cm^{-3}, $n_{\mathrm{H^+}} \approx 0.3$ cm^{-3}). He^+ only constitutes a small fraction of the total number of ions at both altitudes.

Flow speeds The polar wind exhibits a wide variation in flow speeds with altitude:

- *5000 km:* The H^+ ions are supersonic and upflowing with an average speed of 15 km/s, while the O^+ ions are subsonic and moving towards the earth with an average speed of 1 km/s.

- *8 R_E:* Both H^+ and O^+ are supersonic and flowing upwards. The average speed for H^+ is 45 km/s and for O^+ 27 km/s.

Su et al. (1998) admit that the results at 8 R_E are somewhat in contradiction with polar wind models. We would like to stress that the discrepancy between theory and observations to some extent could be explained by the fact that the lowest detectable flow speed for cold hydrogen ions with Polar is 20 km/s. This speed corresponds to a flow energy of 2 eV, which is the energy the ions need to surmount the potential barrier of the spacecraft at 2 V. If many ions have flow speeds below 20 km/s, which is expected from outflow theories and observations at lower altitudes, the statistics in panel 2 (left) in figure 2.3 will be wrong and the mean speed of hydrogen could be considerably smaller. This is not a problem for O^+ ions, since they are much more heavy. At 5000 km a large portion of the hydrogen ions are shielded as well, but these data has been corrected for the spacecraft potential using a bi-Maxwellian filling in procedure, explaining why it is possible to attain average velocities below 20 km/s.

Temperature At 5000 km the perpendicular temperatures are higher than the parallel temperatures for both ion species, which may indicate perpendicular heating by wave-particle interactions. At 8 R_E the parallel temperatures are higher than
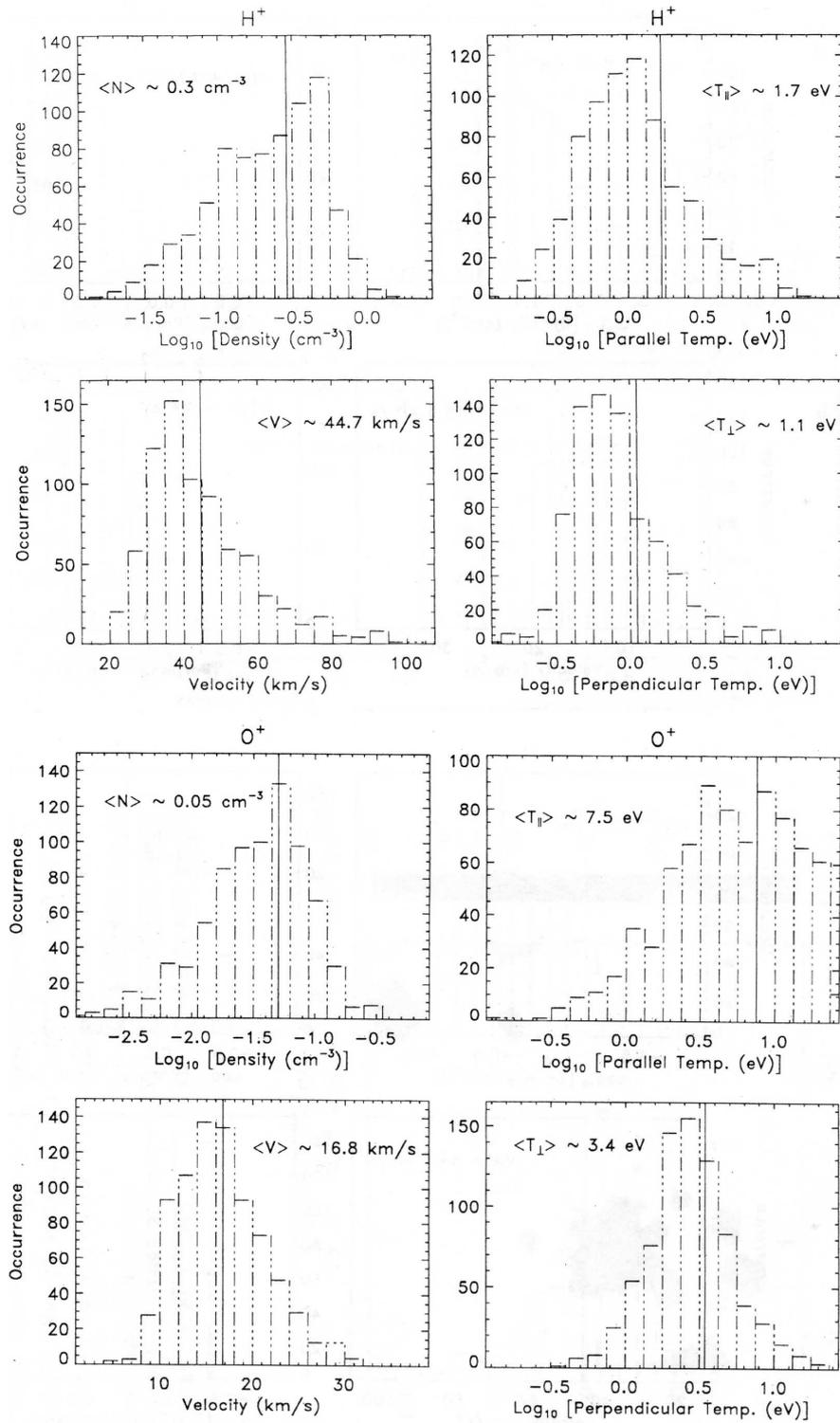
Figure 2.3: Observations of the high altitude polar wind, for H^+ (higher panels) and O^+ (lower panels). (Adapted from *Su et al.* (1998).)
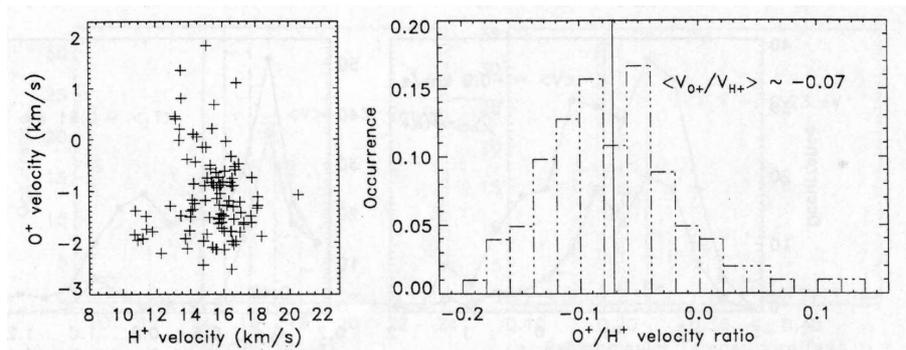
Figure 2.4: Polar wind flow velocities for H^+ and O^+ at 5000 km, where O^+ is on average downward moving. (Adapted from *Su et al.* (1998).)

> the perpendicular temperature, probably as a result of adiabatic conversion of perpendicular to parallel energy during outward motion along magnetic field lines. The temperature of O^+ is higher than of H^+ at both altitudes. In general, the temperatures are higher than predicted by thermal theories.

The outflowing polar wind contributes significantly to the magnetospheric plasma. Using Polar TIDE/PSI observations together with a particle trajectory code *Chappell et al.* (2000) suggested that low-energy polar wind ions (less than 10 eV) travel out through the lobes into the magnetotail to supply the plasma sheet (see figure 2.5). Moving into the plasma sheet the ions get heated fast to typical plasma sheet energies. (This result was obtained from the particle simulations, which only included the magnetic field of the neutral sheet and the dawn-to-dusk convection electric field, but not wave-particle interactions.) As depicted in figure 2.6, the energy of the outflowing ions changes also in the polar region itself. These changes occur mainly in the auroral regions, where parallel electric fields and wave-particle interactions are frequent (*Schunk*, 1999).
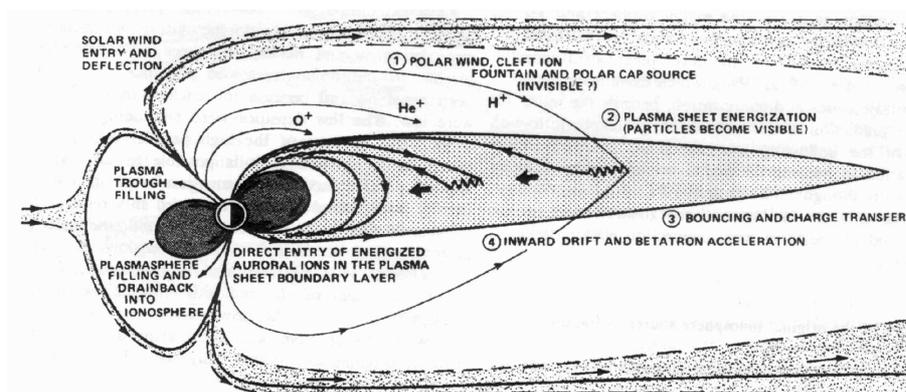
Figure 2.5: The polar wind supplies plasma to the magnetosphere. Cold polar wind ions drift in the lobes into the plasma sheet, where they get energised. (Adapted from *Chappell et al.* (2000).)

Magnetotail

As described in the previous section, outflowing cold ions from the polar regions are transported to the lobes and into the magnetotail. Such cold ions have been observed
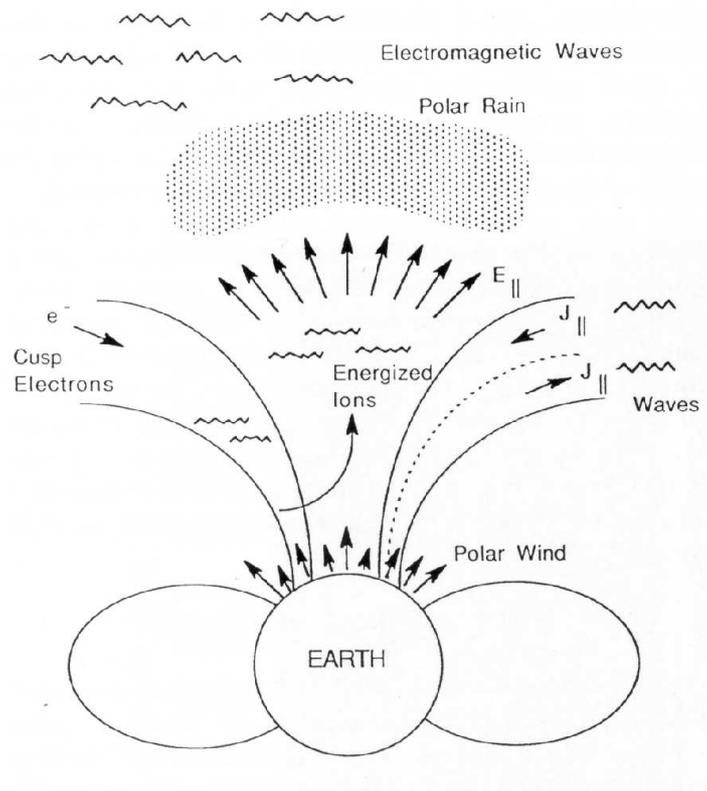
Figure 2.6: Schematic picture of different acceleration processes that can affect the polar wind. (Adapted from *Schunk and Sojka* (1997).)

in the lobes, the plasma sheet boundary layer (PSBL) and the plasma sheet (*Etcheto and Saint-Marc*, 1985; *Seki et al.*, 2003; *Sauvaud et al.*, 2004).

Seki et al. (2003) reported cold ions in the plasma sheet, which were exempted from heating. The observations were made by the GEOTAIL spacecraft at positions from 8 to 27 R_{E} from the Earth. At the time of observation the spacecraft was in eclipse behind the Earth, yielding a negative spacecraft potential as a result of inhibited photoelectron emission. The negative spacecraft potential allowed detection of all distributions of ions, regardless of temperature. The authors suggest that the cold ions may not have passed through the boundary heating region adjacent to the plasmasheet (the PSBL), but have directly flown out from the ionosphere. However, the gradual filling of a magnetic flux tube that has already passed the heating region would take several hours, which is much longer than the transport of the flux tube predicted by ordinary magnetic convection theory. If this interpretation is correct, ionospheric outflow fluxes predict that the conventional ideas of magnetospheric convection have to be reformulated.

In the PSBL *Etcheto and Saint-Marc* (1985) found "anomalously" high plasma densities (around 5 cm^{-3}) and low perpendicular energies (less than 30 eV) using measurements from a relaxation sounder on board the two ISEE spacecraft. The origin of the cold and dense plasma was not possible to deduce in this study, but the authors give two possible explanations:

1. *Detachments from the plasmasphere:* Cold plasmaspheric detachments are con-

vected into the nightside magnetotail.

2. *Outflowing ions from polar regions:* High density plasma in the polar ionosphere supplies the PSBL.

Sauvaud et al. (2004) have presented case studies of cold ions in the lobes, the plasma sheet and PSBL using the Cluster ion spectrometers (CIS). These ions have only been detected for high drift velocities, when the drift energy is high enough to overcome the spacecraft potential barrier. The study confirms the idea of transport of ionospheric ions into the magnetotail and show in particular that ions are massively injected from the nightside ionosphere into the tail during storms and substorms. One single injection can even account for over 80% of the plasma sheet O^+ population. Furthermore, the observations of a cold proton population inside the PSBL during quiet times preceding a substorm was reported. The cold ions are accelerated to several hundreds km/s as a result of fast flows in the PSBL[4], which allows to measure the density of this population precisely. The density of the cold population of around 0.1 cm^{-3} is almost comparable to the density of the hot plasma sheet ions, which reaches a maximum of 0.25 cm^{-3} in this study. Other examples, where accelerated cold ions in the magnetotail have been able to overcome the spacecraft potential barrier, are presented by *Orsini et al.* (1990) and *Seki et al.* (2002).

In Paper III (*Engwall et al.*, 2006a), we report cold ions in the magnetotail lobes at 18 R_E measured simultaneously with two alternative methods: 1. Ion detectors in combination with artificial spacecraft potential control. 2. Deriving ion flow velocity from electric field instruments. As far as we know, this is the first study of flow properties of low-energy ions below 50 eV beyond the Polar apogee of 8 R_E.

Dayside magnetosphere

Plasmaspheric detachments can expel large amounts of cold dense plasma into the dayside magnetosphere. This has been observed by many spacecraft[5]. This plasmaspheric plasma contributes to both microscale and macroscale physical processes. Recent observations with Polar (*Chen and Moore*, 2004) have revealed a large number of plasmaspheric ions flowing with high velocity towards the subsolar magnetopause. These fast flows seem to occur predominantly at southward IMF, which may suggest that they are related to the process of reconnection at the dayside magnetopause: the plasmaspheric detachment flows to fill the low density reconnection region, bringing its frozen in flux tubes towards the approaching solar wind, thus contributing to new reconnection processes.

Cold ions have also been observed by Cluster in the upper dayside magnetosphere adjacent to the magnetopause (*Sauvaud et al.*, 2001). These ions became visible to the ion instrument only when they were accelerated by intermittent motion of the magnetosphere. However, they were shown to exist at other times by simultaneous

---

[4]The occurrence of such fast flows in the PSBL can create Alfvén perturbations in the lobe, which have also been observed in the present study by *Sauvaud et al.* (2004). The authors argues that the flows could also trigger Kelvin-Helmholtz instabilities.

[5]e.g. Ogo 4, 5, and 6, Ariel 3, ATS and LANL geostationary satellites (see *Chen and Moore* (2004), and references therein).

observations with the WHISPER[6] experiment. The density of this cold ion population was found to be as high as 1 cm^{-3}, which is much higher than the surrounding local density of ions.

---

[6]Whisper of HIgh frequency and Sounder for Probing Electron density by Relaxation (*Décréau et al.*, 2001).

Chapter 3

Probe measurements of plasma

Many plasma instruments, e.g. for measurements of electric fields, density and temperature, are based on the Langmuir probe theory (*Mott-Smith and Langmuir*, 1926). These instruments use probes, which collect particles from the ambient plasma. To understand the functioning of the probe instruments, it is essential to quantify the particle currents to the probe, which will be the subject of the following section. For the interested reader, we will give the derivations of these currents in detail. However, to be able to follow the rest of the thesis, it is only important to note that the currents are exactly determined for spherical and cylindrical probes under certain conditions and that the currents are dependent on plasma density and temperature as well as on probe potential. The probe theory is also the basis for understanding spacecraft charging, which is treated in section 4.1.

3.1 Probe currents in Maxwellian plasmas

The quantification of the probe currents was first carried out theoretically by Mott-Smith and Langmuir (*Mott-Smith and Langmuir*, 1926) by using the *orbital motion limited theory* (OML). This theory is not based on plasma physics, but regards a distribution of particles moving in the vacuum field from the probe, thus obtaining trajectories determined only by conservation of energy and angular momentum. This approach can be adopted when the radius of the probe is much smaller than the Debye length. If the probe radius, on the contrary, is much larger than the Debye length, the probe will be efficiently shielded and *sheath limited theory* (SL) must instead be used. In the following, we will only regard OML theory in unmagnetised plasmas and apply it to spherical probes, noting that it is fully developed also for cylinders.

Mott-Smith and Langmuir (1926) treat the currents to a probe in an isotropic plasma. As a starting point, they examine the *random currents*, which are the currents to a probe at zero potential, and then continue with the currents to a charged probe (see sections 3.1.1 and 3.1.2). If the plasma is drifting with respect to the probe, the equations for the currents have to be modified to the form given in section 3.1.3. In addition to the currents from the ambient plasma to the probe, the photoelectron current often gets important in space for sunlit probes (see section 3.1.4). In section 3.1.5, we describe how all the currents balance at a certain potential, which is called the *floating potential* of the probe.

3.1.1   Random current

Consider a charged particle with orthonormal velocity components u, v and w at some distance r from an *uncharged* spherical probe with radius a. The component u gives the radial velocity, counted positive when directed towards the probe, while v and w are tangential velocity components. In a Maxwellian plasma the distribution function is then given by

$$f(u,v,w) = n \left(\frac{m}{2\pi KT} \right)^{3/2} e^{-\frac{m}{2KT}(u^2+v^2+w^2)}, \tag{3.1}$$

if we consider a region so far from the probe that absorption by the probe does not change the plasma.

The number of particles per unit volume in the velocity range $[u,\, u+du]$, $[v,\, v+dv]$ and $[w,\, w+dw]$ is

$$f(u,v,w)\, du\, dv\, dw = n \left(\frac{m}{2\pi KT} \right)^{3/2} e^{-\frac{m}{2KT}(u^2+v^2+w^2)}\, du\, dv\, dw. \tag{3.2}$$

Now, set $p = \sqrt{v^2 + w^2}$. Then, $v = p\cos\Psi$ and $w = p\sin\Psi$, where $\Psi = \arctan\left(\frac{w}{v}\right)$ ($p \in [0,\infty[$ and $\Psi \in [0,2\pi[$). This change of variables yields

$$f(u,v,w)\, du\, dv\, dw = g(u,p,\Psi) \left| \frac{\partial(v,w)}{\partial(p,\Psi)} \right| du\, dp\, d\Psi = g(u,p,\Psi)\, p\, du\, dp\, d\Psi, \tag{3.3}$$

where

$$g(u,p,\Psi) = n \left(\frac{m}{2\pi KT} \right)^{3/2} e^{-\frac{m}{2KT}(u^2+p^2)}. \tag{3.4}$$

The current to the probe from the plasma is created by plasma particles hitting the probe. Only particles with positive radial velocities, *i.e.* $u \in [0,\infty[$, will reach the probe and contribute to the current. Thus, the particle flux to the probe is

$$\Phi = \int_0^{2\pi} \int_0^{\infty} \int_0^{\infty} u\, g(u,p,\Psi)\, p\, du\, dp\, d\Psi = n\sqrt{\frac{KT}{2\pi m}}. \tag{3.5}$$

The number of particles per second hitting a spherical surface, S, centred at the probe is then given by $\eta = S\Phi$. The current to the probe is obtained by multiplying the above expression by the particle charge, q, *i.e.* $I = q\eta$. At the surface of the probe $S = 4\pi a^2$, which gives the final expression for the current:

$$\boxed{I = 4\pi a^2 nq \sqrt{\frac{KT}{2\pi m}} = 2nqa^2 \sqrt{\frac{2\pi KT}{m}} \equiv I_{\text{th}}.} \tag{3.6}$$

This is the *random current* to a probe in a Maxwellian plasma for the particle species of mass m and charge q.

3.1.2 Current to charged probe

In this section, we derive the current to a spherical probe charged to a potential V_{p} with respect to the plasma. As described in section 2.2, the potential from a charged object immersed in a plasma will be shielded by charges of opposite sign. A negatively charged object will for example be shielded by a cloud of positive ions. The shielding particles together form a *sheath*, beyond which the potential from the object will not reach. Now consider a particle at the sheath edge, s, with charge q, radial velocity u and tangential velocity components v and w. As in the previous section v and w are replaced by $p = \sqrt{v^2 + w^2}$ and the same transformation is performed for the distribution function: $f(u, v, w)\, du\, dv\, dw = g(u, p, \Psi)\, p\, du\, dp\, d\Psi$.

The probe current can be obtained through the particle flow to the probe, $I = q S_a \Phi_a$, where S_a is the surface area of the probe and Φ_a the particle flux to the probe at its surface ($r = a$). As in the derivation of the random current, $\Phi(r)$ can be integrated from the distribution function. Inside the sheath, the plasma has been disturbed by the potential from the probe, and the distribution function has to be derived from Liouville's theorem (*Goldstein et al.*, 2002), which states that the distribution function along a particle trajectory is constant. If we can trace a particle from the sheath to the probe surface, it is therefore possible to determine the current from the distribution function at s. Since the plasma is undisturbed outside the sheath, the distribution function at s is taken to be a common Maxwellian.

The tracing of the particles is performed by considering the principles of conservation of energy and angular momentum. If u_{a} and p_{a} are the radial and tangential velocity components, respectively, for a particle arriving at the probe surface ($r = a$), we obtain

$$\frac{1}{2}m(u^2 + p^2) = \frac{1}{2}m(u_{\mathrm{a}}^2 + p_{\mathrm{a}}^2) + qV_{\mathrm{p}} \qquad \text{(energy)} \tag{3.7}$$

$$ps = p_{\mathrm{a}}a \qquad \text{(angular momentum)}, \tag{3.8}$$

assuming zero potential at infinity.

Combining the equations yields

$$u_{\mathrm{a}}^2 = u^2 - \left(\frac{s^2}{a^2} - 1\right)p^2 - 2\frac{q}{m}V_{\mathrm{p}} \tag{3.9}$$

$$p_{\mathrm{a}} = \frac{s}{a}p. \tag{3.10}$$

To reach the probe the particle has to be approaching the probe, *i.e.* $u > 0$, since outside the sheath, there is no field that could attract the particle to the probe. Moreover, from a mathematical point of view, $u_{\mathrm{a}}^2 \geq 0$. Inserting the last condition into equation (3.9) leads to the following inequality for p:

$$p^2 \leq \frac{a^2}{s^2 - a^2}\left(u^2 - 2\frac{q}{m}V_{\mathrm{p}}\right). \tag{3.11}$$

Let $p_1 = \sqrt{\frac{a^2}{s^2 - a^2}\left(u^2 - 2\frac{q}{m}V_{\mathrm{p}}\right)}$, so that the range of p is $[0, p_1]$. Since $p^2 \geq 0$, inequality (3.11) also leads to an additional condition for u: $u^2 \geq 2\frac{q}{m}V_{\mathrm{p}}$, which is automatically

satisfied for attractive potentials ($qV_\mathrm{p} < 0$). We thus have $u \geq u_1$, where $u_1 = 0$ for attractive potentials and $u_1 = \sqrt{2\frac{q}{m}V_\mathrm{p}}$ for repulsive potentials. Now, we can calculate the flux at $r = s$ of particles which will eventually reach the probe and contribute to the current:

$$\Phi(s) = \int_0^{2\pi} \int_{u_1}^\infty \int_0^{p_1} u\,g(u,p,\Psi)\,p\,dp\,du\,d\Psi =$$

$$= n\sqrt{\frac{KT}{2\pi m}}e^{-\frac{m}{2KT}u_1^2}\left[1 - \left(\frac{s^2-a^2}{s^2}\right)\exp\left(\frac{a^2}{s^2-a^2}\left(\frac{qV_\mathrm{p}}{KT} - \frac{m}{2KT}u_1^2\right)\right)\right]$$

(3.12)

The current to the probe then is

$$I(s) = qS\Phi(s)$$

$$= q4\pi s^2 n\sqrt{\frac{KT}{2\pi m}}e^{-\frac{m}{2KT}u_1^2}\left[1 - \left(\frac{s^2-a^2}{s^2}\right)\exp\left(\frac{a^2}{s^2-a^2}\left(\frac{qV_\mathrm{p}}{KT} - \frac{m}{2KT}u_1^2\right)\right)\right]$$

(3.13)

Letting the sheath expand to infinity, equation (3.13) takes the form

$$I_\infty = \lim_{s\to\infty} I(s) = 4\pi a^2 nq\sqrt{\frac{KT}{2\pi m}}e^{-\frac{m}{2KT}u_1^2}\left(1 - \frac{qV_\mathrm{p}}{KT} + \frac{m}{2KT}u_1^2\right) =$$

$$= I_\mathrm{th}e^{-\frac{m}{2KT}u_1^2}\left(1 - \frac{qV_\mathrm{p}}{KT} + \frac{m}{2KT}u_1^2\right)$$

(3.14)

In this limiting case there will be no shielding, which means that it corresponds to the current to a probe in vacuum, *i.e.* the OML approximation. Inserting the values for u_1, the current to the probe can be expressed as

$$I_\infty = \begin{cases} I_\mathrm{th}\left(1 - \frac{qV_\mathrm{p}}{KT}\right) & \text{(attractive potentials, } qV_\mathrm{p} < 0) \\[2ex] I_\mathrm{th}e^{-\frac{qV_\mathrm{p}}{KT}} & \text{(repulsive potentials, } qV_\mathrm{p} > 0) \end{cases}$$

(3.15)

where I_th is the random current as shown in equation (3.6). When $V_\mathrm{p} = 0$, $I_\infty = I_\mathrm{th}$ as expected.

3.1.3   Probe current in flowing plasma

Medicus (1961, 1962) treats the current to a probe in a flowing plasma. In this case, a particle far away from the probe with velocity v and impact parameter d is considered (see figure 3.1). The particle is outside the sheath surrounding the probe, and thus feels no electrical force. Furthermore, the sheath is assumed to be large compared to

the probe so that OML is applicable and all particles that enter the sheath will not reach the probe. This allows *grazing incidence*, which means that also particles with zero radial velocity at the probe surface contribute to the current.[1]
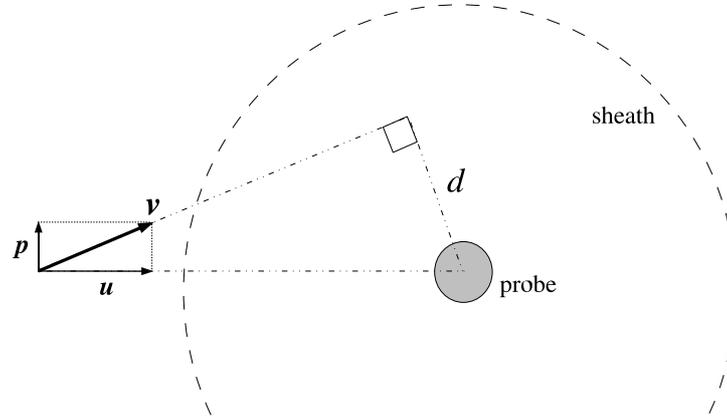
Figure 3.1: *Probe in a flowing plasma.* The velocity outside the sheath is v, which can be decomposed into the radial component u and the tangential component p. The sheath is assumed to be much larger than the probe. d is the impact parameter.

Since no fields are present outside the sheath, the velocity at the sheath edge is v (the same as far away from the probe). Let u and p be the radial and tangential velocity components respectively of v. The velocities at the probe surface ($r = a$) are denoted by subscript a.

As before, the constraints are set up by the principles of conservation of energy and angular momentum:

$$\frac{1}{2}m(u^2 + p^2) = \frac{1}{2}m(u_a^2 + p_a^2) + qV_p \qquad \text{(energy)} \qquad (3.16)$$

$$p_a a = ps = vd \quad \text{(angular momentum)} \qquad (3.17)$$

In the case of grazing incidence, we have $u_a = 0$ and the *limiting impact parameter*, d_g, is then given by

$$d_g^2 = a^2 \left(1 - 2\frac{qV_p}{mv^2}\right). \qquad (3.18)$$

For repulsive potentials qV_p is positive, which means that there is a lower limit on v, since $d_g^2 > 0$. In other words, the velocity of the particle has to be sufficiently high to enable it to overcome the potential barrier and reach the probe. This lower limit is given by

---

[1]This is a simplified treatment compared to Medicus, who also treats the sheath limited case, where any particle entering the sheath will reach the probe.

$$v_1 = \sqrt{\frac{2qV_{\mathrm{p}}}{m}}. \tag{3.19}$$

For accelerating potentials d_{g}^2 is positive for any $v \in [0, \infty[$. All particles with a smaller impact parameter than d_{g} will reach the probe. The current to the probe is then given by the flow through the circle with radius d_{g}:

$$dI = \pi d_{\mathrm{g}}^2 q v F(v) dv,$$

$$= \pi a^2 q \left(1 - 2\frac{qV_{\mathrm{p}}}{mv^2}\right) v\, F(v)\, dv \tag{3.20}$$

$$I = \pi a^2 q \int_{v_1}^{\infty} \left(1 - 2\frac{qV_{\mathrm{p}}}{mv^2}\right) v\, F(v)\, dv, \tag{3.21}$$

where n is the number density, $F(v)$ the speed distribution[2] and v_1 the minimum speed, which is 0 for accelerating potentials and given by equation (3.19) for repulsive potentials. For a drifting plasma with zero temperature, $F(v) = n\delta(v - v_{\mathrm{d}})$, where v_{d} is the drift velocity. The current is then

$$I = \pi a^2 q n \int_{v_1}^{\infty} \left(1 - 2\frac{qV_{\mathrm{p}}}{mv^2}\right) v\delta(v - v_{\mathrm{d}})\, dv = \begin{cases} \pi a^2 q n v_{\mathrm{d}} \left(1 - 2\frac{qV_{\mathrm{p}}}{mv_{\mathrm{d}}^2}\right) & (v_{\mathrm{d}} \geq v_1) \\ 0 & (v_{\mathrm{d}} < v_1) \end{cases} \tag{3.22}$$

The first result holds for all accelerating potentials and for repulsive potentials when the drift velocity is larger than v_1. It is interesting to compare the equations to a charged probe in a non-drifting Maxwellian plasma (equation (3.15)) with equation (3.22). For the attractive potential, the functional forms are identical, with the drift energy $\frac{1}{2}mv_{\mathrm{d}}^2$ replacing the thermal energy KT and $\pi a^2 q n v_{\mathrm{d}}$ replacing the random current $4\pi a^2 q n \sqrt{\frac{KT}{2\pi m}}$, which is easy to understand from a basic consideration of the situation. In the random current, the thermal velocity $\sqrt{\frac{KT}{2\pi m}}$ is replaced by the drift velocity v_{d} and $4\pi a^2$ is replaced by πa^2, since for the flowing plasma a probe at zero potential collects current only from one direction. For repulsive potentials, equation (3.22) is actually consistent with the limit $T \to 0$ of (3.15).

In the case of a drifting Maxwellian plasma the three dimensional velocity distribution is given by

$$f(v_x, v_y, v_z) = n \left(\frac{m}{2\pi KT}\right)^{\frac{3}{2}} e^{-\frac{m}{2KT}[v_x^2 + v_y^2 + (v_z - v_{\mathrm{d}})^2]} \tag{3.23}$$

---

[2]It may at first seem counterintuitive that we can use a scalar argument v in the distribution function $F(v)$, since the drift clearly produces an anisotropy. However, there is no feedback from the particle distribution on the fields in the OML limit, and therefore the anisotropy is not important for the total current to the probe. To put it simply, the probe doesn't care about what direction the particle arrives from. If plasma effects are important, the sheath becomes anisotropic and the present analysis does not hold.

for a drift in the z-direction with velocity v_{d}. Changing to spherical coordinates we get

$$f(v, \theta, \phi) = n \left(\frac{m}{2\pi KT} \right)^{\frac{3}{2}} e^{-\frac{m}{2KT}[v^2 + v_{\mathrm{d}}^2 - 2vv_{\mathrm{d}} \cos \theta]} \tag{3.24}$$

The speed distribution is

$$F(v) = \int_0^\pi \int_0^{2\pi} f(v, \theta, \phi) \, v^2 \sin \theta \, d\phi \, d\theta$$

$$= 2n \sqrt{\frac{m}{2\pi KT}} \frac{v}{v_{\mathrm{d}}} e^{-\frac{m}{2KT}[v^2 + v_{\mathrm{d}}^2]} \sinh \frac{mvv_{\mathrm{d}}}{KT} \tag{3.25}$$

Inserting equation (3.25) into equation (3.21) yields

$$I = qna \sqrt{\frac{2\pi KT}{m}} \left[e^{-\frac{m}{2KT}(v_1^2 + v_{\mathrm{d}}^2)} \left(\frac{v_1}{v_{\mathrm{d}}} \sinh \left(\frac{mv_{\mathrm{d}}v_1}{KT} \right) + \cosh \left(\frac{mv_{\mathrm{d}}v_1}{KT} \right) \right) \right.$$

$$\left. + \sqrt{\frac{KT}{2mv_{\mathrm{d}}^2}} \left(\frac{mv_{\mathrm{d}}^2}{KT} + 1 - \frac{2qV_{\mathrm{p}}}{KT} \right) \mathrm{E} \left(\sqrt{\frac{m}{2KT}}(v_1 - v_{\mathrm{d}}), \sqrt{\frac{m}{2KT}}(v_1 + v_{\mathrm{d}}) \right) \right] \tag{3.26}$$

where $\mathrm{E}(a, b) = \int_a^b e^{-y^2} dy$. In the limit $v_{\mathrm{d}} \to 0$, equation (3.26) reduces to

$$I = qna \sqrt{\frac{2\pi KT}{m}} e^{-\frac{m}{2KT}v_1^2} \left(\frac{mv_1^2}{KT} - \frac{2qV_{\mathrm{p}}}{KT} + 2 \right). \tag{3.27}$$

Inserting $v_1 = 0$ for accelerating potentials and $v_1 = \sqrt{\frac{2qV_{\mathrm{p}}}{m}}$ for repulsive potentials, we retrieve the classical Langmuir results for a non-drifting plasma (see equation (3.15)). For large drift velocities ($v_{\mathrm{d}} \to \infty$) both the ion and electron current will approach $qna^2\pi v_{\mathrm{d}}$ and the total current will thus vanish.

3.1.4 Photoelectron current

For sunlit probes, in addition to plasma ion and electron currents, we have to regard the photoelectron current[3]. In magnetospheric plasmas the photoelectron current is dominating, which brings the probe to a positive potential. The photoelectron current depends on the projected area of the probe to the sun, A_{p}, the surface properties of the probe, local plasma conditions, distance to the Sun and the solar spectrum. Because of these different dependences, there are many different expressions used for the photoelectron current. *Pedersen* (1995) has used measurements to fit an analytical expression to satellite data. In this treatment, we adopt the theoretical expressions for spherical probes derived by *Grard* (1973).

For *negative potentials* all photoelectrons can escape from the probe and the photoelectron current will be saturated at the constant value I_{ph}^0:

---

[3]In a rigorous treatment other effects, such as secondary electron emission, should also be treated (*Garrett*, 1981; *Eriksson et al.*, 1999). These currents are mentioned in section 4.1.

$$I_{\mathrm{ph}} = I_{\mathrm{ph}}^0 = A_{\mathrm{p}}j_{\mathrm{ph}}^0, \qquad V_{\mathrm{p}} < 0 \tag{3.28}$$

where j_{ph}^0 is the photoelectron current density, which has to be estimated from satellite data. The current density shows large variations and can be in the range $j_{\mathrm{ph}}^0 = 1.5 - 8$ nA cm^{-2} for a probe operating in space for a long period (*Laakso et al.*, 1995, and references therein).

Probes at *positive potentials* will recollect some of the photoelectrons, the more the higher the potential is. The photoelectron current for a spherical probe at positive potential can be approximated by the analytic function (*Grard*, 1973)

$$I_{\mathrm{ph}} = I_{\mathrm{ph}}^0 \left(1 + \frac{eV}{KT_{\mathrm{ph}}} \right) \exp -\frac{eV}{KT_{\mathrm{ph}}} \qquad V_{\mathrm{p}} < 0, \tag{3.29}$$

assuming that the probe is smaller than the Debye length and that the photoelectron distribution is Maxwellian. T_{ph} is the photoelectron temperature, which is of the order of 1.5 eV.

3.1.5   Current balance

Combining the photoelectron current with the expressions for the electron and ion currents, current-voltage relations for the probes can be derived. At equilibrium, the currents will balance each other ($\sum_n I_n = I_{\mathrm{e}} + I_{\mathrm{i}} + I_{\mathrm{ph}} = 0$) and the probe will attain its *floating potential*. For sunlit probes operating above Earth's ionosphere, the ion current is negligible and the floating potential is in practice obtained by balancing the current of escaping photoelectrons and impinging plasma electrons. In the magnetosphere, the floating potential is normally a few volts positive (*Pedersen et al.*, 1984). Figure 3.2 shows the current balance for ambient plasma electrons (blue) and escaping photoelectrons (red) to a probe (radius 4 cm) in a magnetospheric plasma of temperature 10 eV and density 10 cm^{-3}. The photoelectron current density is assumed to be 6 nAcm^{-2}. The currents balance each other at approximately 9.3 V positive.

For a probe in shadow, the situation becomes very different. In this case the probe will be at negative potential and if the ion and electron temperatures are equal the current balance equation reduces to

$$Me^x + x - 1 = 0, \tag{3.30}$$

where $x = eV_{\mathrm{p}}/KT_{\mathrm{e}}$ and $M = \sqrt{m_i/m_e}$, m_e and m_i being the electron and ion mass respectively. The numerical solution of the equation is $x = eV_{\mathrm{p}}/KT_{\mathrm{e}} \approx -2.5$. The negative potential can be explained by the fact that, when the electron and ion temperatures are equal, the electrons will move faster than the ions and thus hit the probe more frequently.

3.2   Probe measurements of densities and temperatures

Langmuir probes have been used for measurements of among other plasma densities, temperatures and electric fields in space since the beginning of the space era, and
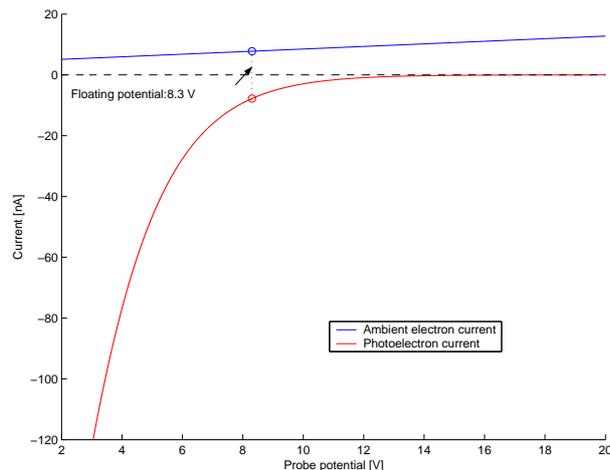
Figure 3.2: Current balance of impinging plasma electrons and escaping photoelectrons to a probe of radius 4 cm. The temperature of the plasma is 10 eV and the density is 10 cm^{-3}. The photoelectron current density is 6 nAcm^{-2}. In such a tenuous plasma the ion current is negligible. The floating potential is around 8.3 V.

even earlier in laboratory plasmas. Still, they form the basis in many dominating measurement techniques. In this thesis, we will focus on double-probe electric field instruments, but probe measurements of densities and temperatures also deserve a brief introduction.

To measure the temperatures and densities in a plasma (n_i, n_e, T_i and T_e) a method of *voltage sweeps* is used. In this mode the bias voltage applied to the Langmuir probe is varied, while the total current to the probe is measured, which produces a current-voltage curve. Fitting the analytical expressions for the electron, ion and photoelectron currents (see e.g. equations 3.15, 3.28 and 3.29) to this measured curve, we can retrieve estimates of the densities and temperatures.

Currently, two large spacecraft missions implement Langmuir probes for density and temperature measurements: the Cassini and Rosetta spacecraft. Cassini explores the surroundings of the giant planet Saturn, its ring planes and its largest moon Titan. The first data from the Cassini Langmuir probe, collected during 2005, have provided new exciting results on among others the cold plasma in the ionosphere of Titan (*Wahlund et al.*, 2005). Rosetta is sent out to follow a comet on its journey from far out in the solar system towards the hot Sun, where large parts of the icy nucleus have been vaporised. The Langmuir probe will measure the densities and temperatures in the coma of the comet (*Eriksson et al.*, 2006b).

3.3 Electric field measurements with double probes

Measurements of electric fields are crucial to understand the environment in space. Together with the magnetic fields, the electric fields determine the motion of the plasma particles. One of the most common techniques for electric field measurements is the double probe technique, which has been well summarised by *Pedersen et al.* (1998). Additional information can be found in *Pedersen et al.* (1984), *Mozer* (1973), and *Fahleson* (1967).

3.3.1 Measurement technique

The double-probe instrument uses a conceptually simple technique of measuring the potential difference between two probes in a plasma. A simplified picture of the double-probe electrical system is given in figure 3.3. For electric field measurements, we are interested in the potential difference $\Phi_1 - \Phi_2$. The electric field is obtained by dividing this difference with the probe separation. However, it is only possible to measure the quantity $U_1 - U_2$, which equals $(\Phi_1 - \Phi_2) + (V_1 - V_2)$, where V_1 and V_2 are the potentials of the probes with respect to the plasma. The double-probe technique is based on the assumption that the coupling between plasma and probe is the same at the two probes, *i.e.* $V_1 = V_2$, so that

$$U_1 - U_2 = \Phi_1 - \Phi_2. \tag{3.31}$$
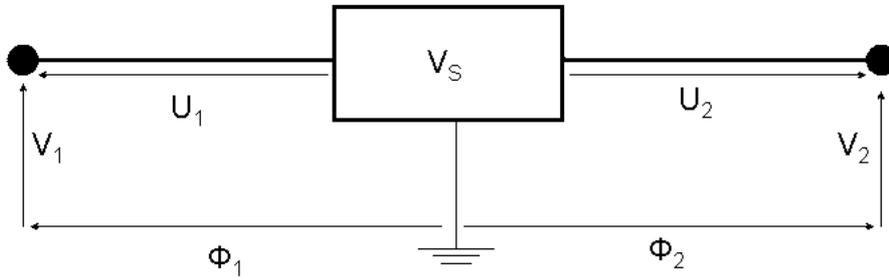
Figure 3.3: Simplified electrical schema of the double-probe/spacecraft system. U_1 and U_2 are the potentials between spacecraft and probes, V_1 and V_2 the potentials between probes and plasma and $\Phi_1 - \Phi_2$ the real potential difference in the plasma. The ground point is of course arbitrary.

To achieve this situation there are some requirements that have to be fulfilled (*Pedersen et al.*, 1998; *Fahleson*, 1967):

1. *Equally shaped probes.* The probes should be equally shaped to avoid that the probe sheaths become different.

2. *Large probe separation.* The separation between the probes should be large to avoid that the probes disturb each other or more likely are affected by the spacecraft. The only practical solution is to mount the probes on wire booms, which are deployed from a spinning spacecraft (*Pedersen et al.*, 1998). A spinning spacecraft leads to other requirements: If we do not want the photoemission to vary with the spin, the probes should be spherical.

3. *Same material and electrical loading.* The probes should be constructed with the same surface material and same electrical loading.

The measured electric field from a double-probe instrument is not the actual electric field in the plasma, since the spacecraft and probes are moving with respect to the plasma (*Fahleson*, 1967; *Mozer*, 1973). The electric field in the Earth's rest frame, $\boldsymbol{E}$, is obtained from the measured electric field, $\boldsymbol{E'}$, using the formula

$$\boldsymbol{E} = \boldsymbol{E'} - \boldsymbol{v} \times \boldsymbol{B}, \tag{3.32}$$

where $\boldsymbol{v}$ is the velocity of the satellite in the Earth system and $\boldsymbol{B}$ is the Earth's magnetic field. This means that for measurements of the electric field in a frame of reference independent of the spacecraft motion, we also need detailed measurements of $\boldsymbol{v}$ and $\boldsymbol{B}$. For a rotating spacecraft with radially deployed probes, it is the spin plane component of the electric field that is measured. To obtain the full electric field vector, it is normally a good assumption to take $E_\perp \gg E_\parallel$, at least for quasi-DC fields. If $\boldsymbol{B}$ is not too close to the spin plane, the total field can be constructed from the spin plane component and the relation $\boldsymbol{E} \cdot \boldsymbol{B} = 0$. One double-probe system on a spinning spacecraft is thus normally sufficient to determine the full electric field vector. However, it will take one spin period, which will prevent measurements of rapidly varying electric fields. If two double-probes are used instead, the total electric field vector can be determined immediately and the only limitation is probe function and telemetry (*Pedersen et al.*, 1998).

For measurements in a dense plasma the electron and ion currents are sufficiently high to give a good coupling between probe and plasma. In a tenuous plasma, photoemission is essential for satisfactory probe-plasma coupling, which means that the probes have to be sunlit to function. As can be seen in figure 3.2, the probes float at a relatively high potential where the slope of the photoelectron current is small. This means that a small spurious current to one of the probes can result in a large false electric field. It is therefore desirable to bring the probe closer to the plasma potential, where the current-voltage curve is steeper, which can be achieved by applying a bias current from the probe to the spacecraft (see figure 3.4).
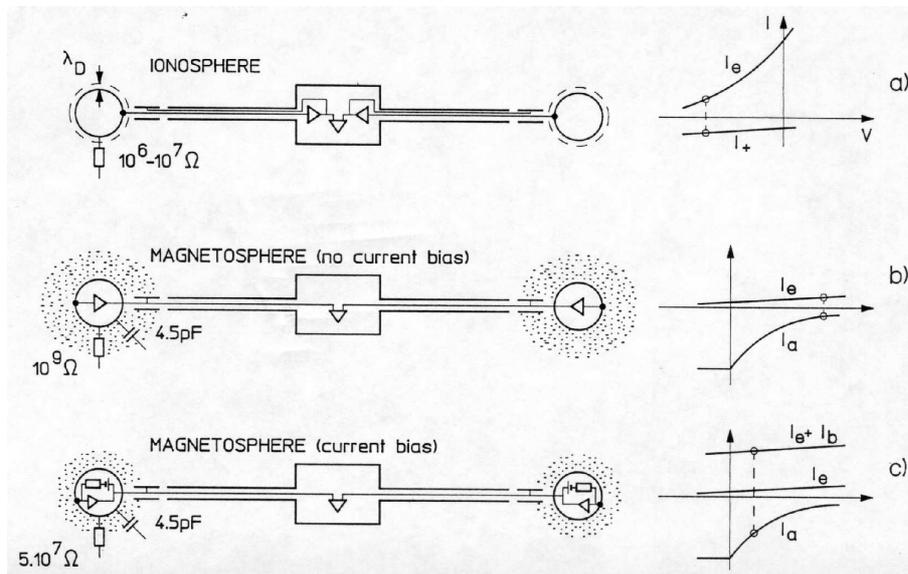
Figure 3.4: The double-probe instrument in different environments: a) The ionosphere, b) The magnetosphere, c) The magnetosphere with bias current. The bias current brings the probe potential closer to the plasma potential, where small spurious currents will not influence the potential of the probe. (Adapted from *Pedersen et al.* (1998))

Even though the photoemission provide the necessary coupling between probe and plasma, it also introduces new errors in the measurement: If the booms are at the same potential as the spacecraft, which is normally the case, the probe furthest away from the Sun will lose more photoelectrons to the booms than the probe closest to the Sun (see figure 3.5). This phenomenon creates a spurious sunward electric field. To reduce

this asymmetric current of photoelectrons, the booms are commonly constructed with a negatively biased *guard* close to the probe (*Pedersen et al.*, 1984). The guard will also decrease leakage currents from the spacecraft photoelectrons to the probes and too much influence from the boom potential on the electric field measurement. Thus, the guard reduces the effects of photoelectrons, but nevertheless there will always be a small sunward offset in double-probe data. For Cluster this offset is around 1 mV/m. This offset is analysed in paper 3.

The surface of the spacecraft has to be sufficiently conductive to serve as a good reference for the double-probe instrument and the current bias system. In addition, a less conductive surface would create differential charging of the satellite, giving rise to a spurious anti-sunward electric field (*Pedersen et al.*, 1984). For a sufficiently conductive surface, the double-probe instrument also provides two useful by-products (*Pedersen et al.*, 1984, 2001):

- *The spacecraft potential.* The spacecraft potential can be determined with a accuracy of $\pm$ 1.0 V from the potential between the probe and the spacecraft. This is useful for interpreting data from particle instruments, and can also be used to derive the plasma density (see below).

- *The plasma density.* The plasma density can be related to the spacecraft potential[4] through the current relations derived in section 3.1. To get an empirical relation between the plasma density and the spacecraft potential for a specific satellite, the spacecraft potential is compared to the plasma density derived from an on-board density instrument (*Pedersen*, 1995; *Pedersen et al.*, 2001; *Escoubet et al.*, 1997). The advantage of using the spacecraft potential for density measurements is the high sampling frequency and the simplicity to interpret the resulting data. It should be noted that the density alone does not determine the spacecraft potential: the temperature is also a factor, so the temperature has to be assumed to stay within some range for a plasma density-spacecraft potential calibration to be valid.
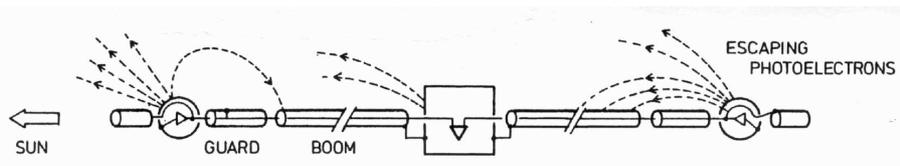
Figure 3.5: The probe furthest away from the Sun will lose more photoelectrons to the positively charged booms than the probe close to the Sun, which will cause a spurious sunward electric field. The errors can be decreased by applying a negatively biased guard near the probes. (Adapted from *Pedersen et al.* (1984).)

3.3.2   Complications

Known sources of spurious electric fields influencing measurements by double-probe instruments include:

---

[4]The floating potential of the spacecraft will be very close to that of an unbiased probe, as we will see in section 4.1.

1. Asymmetries of the probes.

2. Coupling between probes and boom tips.

3. Wake effects.

4. Magnetisation.

5. Plasma density gradients.

How to prevent effects of the two first causes has already been treated in the previous section. The influence of wakes is covered in section 5.3.

Magnetisation could complicate the measurements, when the electron gyroradius is comparable to or smaller than the probe dimensions (*Fahleson*, 1967). In such a case, the probes will mostly collect electrons from a column parallel to the magnetic field. Gradients in the plasma density along the boom direction will cause spurious electric fields, since the basis of the assumption $V_1 = V_2$ is that the plasma is homogeneous. This error can be reduced by applying an appropriate bias current (*Laakso et al.*, 1995).

A problem with a spinning double-probe system, not related to spurious electric fields, is that we are able to measure the parallel electric field only when the spin axis is perpendicular to $\boldsymbol{B}$. In many cases it would also be interesting to measure parallell electric fields (*Fahleson*, 1967), *e.g.* in the auroral acceleration regions.

Chapter 4

Spacecraft-Plasma Interactions

Spacecraft interact with the particles in the surrounding plasma, which has many consequences for both the spacecraft itself and the plasma environment. One of the phenomena of great importance is *spacecraft charging*. Another effect, which has already been mentioned briefly in connection with complications for double-probe electric field instruments, is *wakes* behind spacecraft.

4.1   Spacecraft charging

The area of spacecraft charging has been subject to extensive research, especially for commercial satellites, since the potential of a spacecraft in a dense plasma with very energetic (~ 10 keV) electrons can reach high negative values on the order of kV. If the spacecraft is charged unevenly, hazardous electrostatic discharges between different parts of the spacecraft may occur, which will affect the performance of the satellite. The problem of uneven charging can often be solved by using a conductive surface on the spacecraft. Nevertheless, spacecraft charging and discharges remain an issue, especially for certain elements, which for some reason are isolated, and for specifically vulnerable parts of the spacecraft, such as solar panels. The term *spacecraft charging* has mainly been attributed to cases with high negative potentials. In this section we will treat the process behind all types of charging of spacecraft, regardless of the resulting potential.

What makes the spacecraft charge at all? The process of spacecraft charging can be understood by probe theory: we just exchange the probe for the much larger spacecraft and the qualitative picture of currents to the probe/spacecraft remains the same. However, we have no exact analytical expression for the currents in this case, since spacecraft seldom are perfectly spherical or cylindrical. To get quantitative estimates of the spacecraft charging level we therefore have to go to numerical simulations.

As we saw for the probes, an object immersed in a plasma will be hit by the plasma particles due to their thermal motion. The particles are collected by the object, and at thermal equilibrium it will become negatively charged, since the electron current exceeds the ion current at zero potential and equal ion and electron temperatures. This can be explained by the fact that ions and electrons have the same energy at thermal equilibrium, but the electrons move faster, because of their much lower mass. This results in the electrons hitting the probe more frequently, leading to a net negative charge. As was stated in section 3.1.4, photoemission is important in sunlit parts

of the magnetosphere. There exist also further charging effects, which can become important in special cases. Including these additional charging effects, the current balance equation (see section 3.1.5) takes the form

$$\sum_n I_n = I_e + I_i + I_{bse} + I_{se} + I_{si} + I_{ph} + I_b = 0. \tag{4.1}$$

I_e, I_i and I_{ph} are, as in the probe case, the electron, ion and photoelectron current, respectively. The term I_{bse} is the current of backscattered electrons due to I_e. The currents I_{se} and I_{si} consist of secondary electrons, emitted when electrons and ions hit the spacecraft.[1] In most cases for sunlit magnetospheric spacecraft, the secondary electron emission is negligible compared to the photoelectron current I_{ph}. In sunlit magnetospheric plasmas, the photoelectron current will be dominant over all other currents and the spacecraft will reach a positive potential, where most of the photoelectrons are recollected by the spacecraft, and it is only the small fraction of high energy photoelectrons escaping into the ambient plasma that will establish an equilibrium with the other currents (*Torkar et al.*, 1998). I_b, finally, is the current from a possible active ion source installed on the spacecraft, which is used for example for propulsion or potential control. An example is the potential control device on-board Cluster, called ASPOC[2] (*Torkar et al.*, 2001), which operates successfully to reduce the several tens of volts positive spacecraft potential to constant values of a few volts. The potential control makes it possible to measure low energy ions. In addition to these currents, there could also be currents between adjacent surfaces, if they are charged to different potentials. One may also have to consider displacement currents for time-dependent problems.

As was mentioned in section 3.3.2, the spacecraft potential can be used to measure the plasma density. *Pedersen et al.* (2001) have been able to extract a potential-density relation for the Cluster spacecraft, which is shown in figure 4.1. A general remark, is that the potential increases with decreasing density. This is due to the fact that the photoelectron current becomes more and more dominant, when the density and thus the electron current decreases.

4.2 Wake effects

How does a wake form behind a spacecraft in a flowing plasma? A necessary condition for wake formation is that the flow is *supersonic* with respect to the ions, i. e. the flow kinetic energy of the ions, E_k^i, exceeds their thermal energy, KT_i. When an object is placed in a supersonic ion flow, a wake void of ions will be created behind the object. This arises from the fact that the spacecraft is acting as an obstacle to the flowing ions, and since their thermal speed is lower than the speed of the flow, the cavity will not be filled immediately. Figure 4.2 gives a schematic illustration of this phenomenon. If the flow is not only supersonic for the ions, but also *subsonic* for the electrons ($E_k^e < KT_e$), the electrons will be able to access the wake region, thus giving rise to a negatively charged wake behind the spacecraft[3]. This is the case for the motion of a spacecraft

---

[1]The currents I_{bse}, I_{se} and I_{si} should be included also for the probes in section 3.1.5, but were omitted for simplicity.

[2]Active Spacecraft Potential Control.

[3]If the thermal energy of the electrons is close to the ion kinetic energy, the negative charge will affect the motion of the ions considerably, thus changing the shape of the wake.
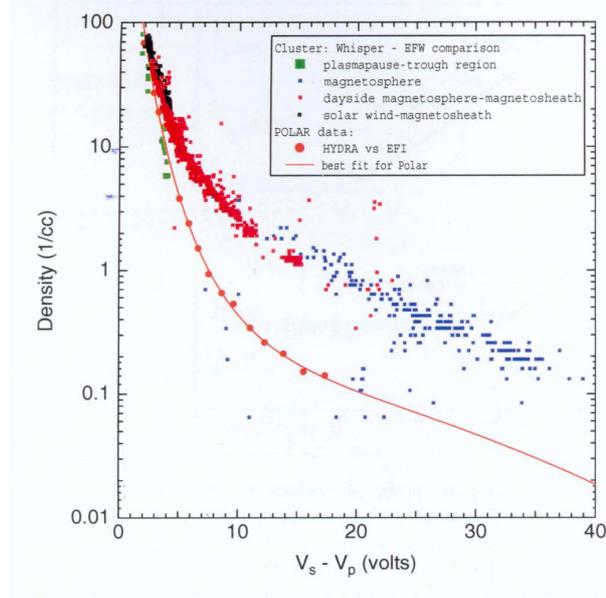
Figure 4.1: Spacecraft potential-density relation for the Cluster spacecraft. (Adapted from *Pedersen et al.* (2001)).

in the polar wind, but also in the dense solar wind and in the ionosphere, where wakes normally have been studied. The high plasma density in the solar wind makes it different from the tenuous polar wind, however, since it will ensure a low spacecraft potential. Thus, in the solar wind the spacecraft potential, V_s, will not exceed the ion flow energy, E_k^i ($eV_s < E_k^i$). Therefore the ions will only see the spacecraft body as the obstacle. In the ionosphere, the spacecraft potential is even more dense, and the spacecraft will therefore charge negatively. This will focus the ions into the wake, enhancing the filling-in process of the wake.
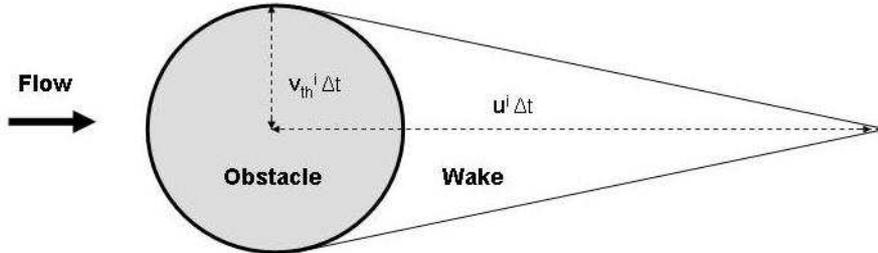
Figure 4.2: Schematic picture of a wake, where $eV_s < E_k^i$. The speed of the ion flow is higher than the ion thermal speed, which will lead to a region void of ions behind the obstacle. The time Δt is the time for the ions to fill the space behind the obstacle due to their thermal speed, v_{th}^i. In this time the ions will travel a distance $u_i\Delta t$ in the flow direction, where u_i is the flow speed. This process will cause the wake behind the spacecraft. If the electrons are subsonic, they will fill the wake, which will obtain a negative net charge.

In cold tenuous plasmas the situation can be quite different, since the low-density plasma ensures such a high spacecraft potential that it may exceed the ion kinetic energy. In such a case, the ions will be prevented from reaching the spacecraft and a supersonic ion flow will obey the following inequality:

$$KT_i < E_k^i < eV_s. \tag{4.2}$$

This means that the potential structure, rather than the physical shape of the space-craft, will act as an obstacle for the ions. Moreover, the ions will be deflected by the spacecraft potential like in Rutherford scattering. These two factors will enhance the wake behind the spacecraft body (see figure 4.3). A large negatively charged wake will therefore be formed behind the spacecraft.
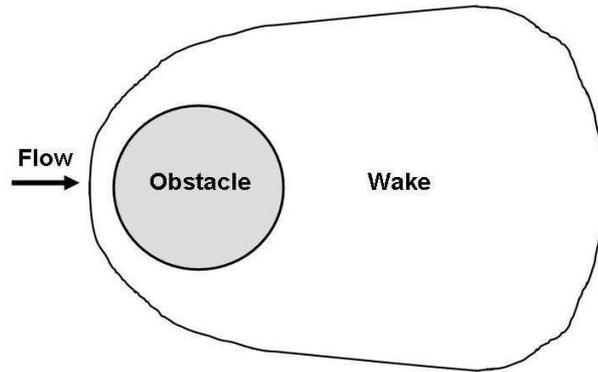
Figure 4.3: Schematic picture of an *enhanced* wake. The ions are deflected by the positive potential of the spacecraft, which is higher than the kinetic energy of the ions ($eV_s > E_k^i$). As for the wake in figure 4.2, this wake will be negatively charged, if the electrons are subsonic.

Chapter 5

Wake effects in Cluster electric field data

5.1 The Cluster satellites

The Cluster mission consists of four identical scientific spacecraft investigating space- and time-varying phenomena in the Earth's magnetosphere (*Escoubet et al.*, 2001). In 1996 the first four Cluster satellites (Cluster I mission) were launched with the first Ariane-5 rocket. Unfortunately, this mission met a premature end, when the rocket exploded only 37 seconds after launch. The second attempt in the summer of 2000 was more successful and the Cluster II mission has now been fully operational for more than five years, and the mission has been extended four years until the end of 2009. The Cluster mission is regarded as a key mission for the European Space Agency, ESA, and has up to date provided a vast range of revealing data.
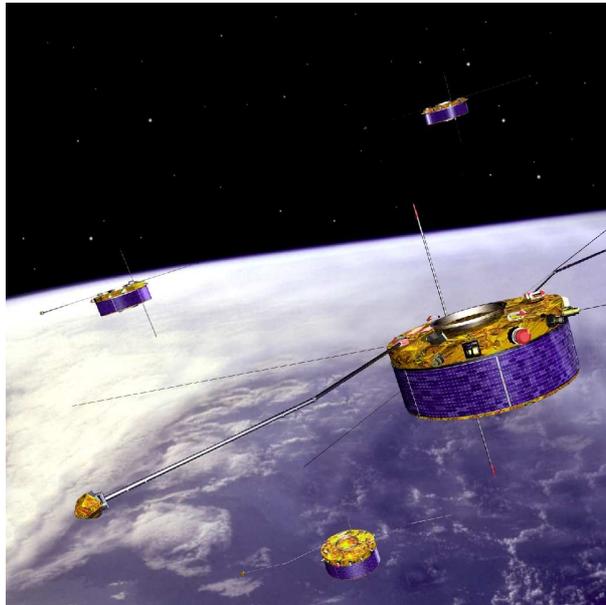
Figure 5.1: An artistic impression of the four Cluster satellites (from *http://sci.esa.int*).

The four satellites are orbiting the Earth in a formation, which is tetrahedral for as large

part of the orbit as Kepler's laws permit, allowing simultaneous measurements at different locations in the magnetosphere. Each satellite carries 11 instruments for charged particle detection and field and waves measurements. The main goal of the Cluster mission is to investigate phenomena in the following key regions of the magnetosphere: *the solar wind, the bow shock, the magnetopause, the polar cusp, the magnetotail* and *the auroral zones.* To achieve this goal, the satellites have elliptical polar orbits with perigee at 4 R_E and apogee at 19.6 R_E[1], thus passing through all the key regions in a period of 57 h (see figure 5.2). The satellites are cylindrical with a height of 1.3 m and diameter of 2.9 m. Their launch mass was 1200 kg, of which 650 kg was propellant and 71 kg scientific payload. The satellites are spinning with a period of 4 s.
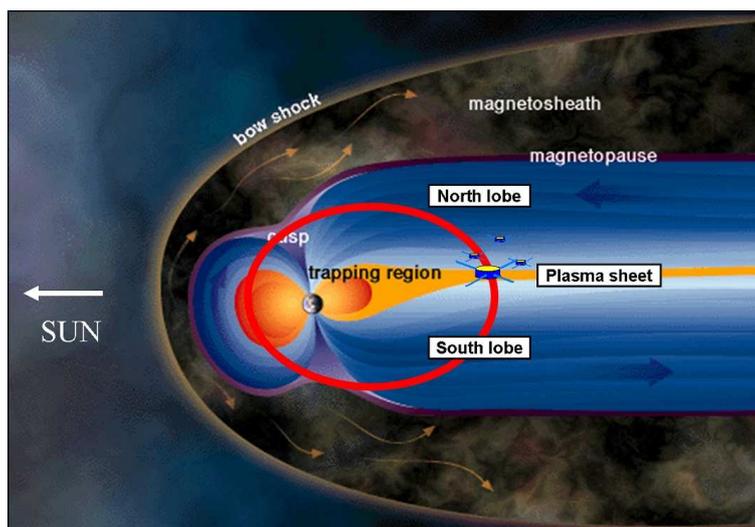
Figure 5.2: The orbit of the four Cluster satellites (from *http://sci.esa.int*). Two of the key regions for the Cluster mission are pointed out: 1. The bow shock. 2. The magnetopause.

5.2 Electric field measurements from Cluster

The Cluster satellites are equipped with two instruments for electric field measurements using different techniques: the Electric Fields and Waves instrument (EFW) (*Gustafsson et al.*, 1997, 2001) and the Electron Drift Instrument (EDI) (*Paschmann et al.*, 1998, 2001). EFW is a double-probe instrument, the principles of which have been thouroughly treated in section 3.3. The EFW probes are mounted on thin wire booms, which are deployed radially by the spinning energy of the spacecraft, resulting in a probe-to-probe separation of 88 m. (Since the probes are confined to the spin plane, the data from EFW provides only information about the component of the electric field in this plane.) The probes are 8 cm in diameter and the diameter of the wire booms is 2.2 mm. Each of the satellites carries two pairs of probes with the booms perpendicular to each other, to be able to measure the electric field up to high frequencies. A bias current is applied between the spacecraft and the probes, which brings the potential to around +1 V. On the booms a guard is placed to prevent asymmetric currents of photoelectrons to the booms. More information about the operational principle of EFW can be found in *Pedersen et al.* (1998).

---

[1]The nominal value of the radius of the Earth (R_E) is 6371.2 km.

Electron drift instruments are based on a technique determining the drift of high-energetic electrons in a magnetised plasma (see figure 5.3). Two beams of keV electrons are emitted from electron guns on the spacecraft. If a sufficiently strong (at least 30 nT) magnetic field is present, the electrons will experience a magnetic force strong enough to make it possible to regain the electrons at detectors on the spacecraft. The electrons will also feel a force from the electric field in the plasma, which will lead to a drift of the electrons at a velocity of $\boldsymbol{E} \times \boldsymbol{B}/B^2$ (see section 2.2). Detecting this drift from the two electron beams, the electric field can be extracted from magnetic field data.
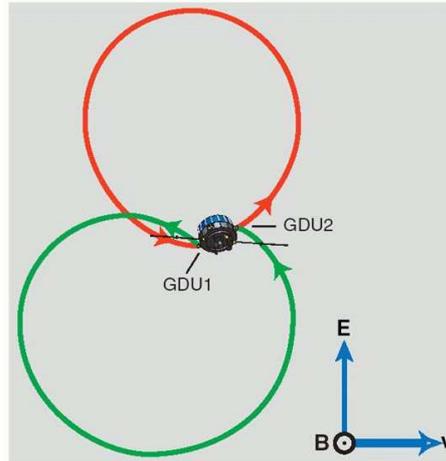
Figure 5.3: The Electron Drift Instrument uses the drift of electrons in a magnetised plasma to measure the electric field Two high energetic electron beams are emitted from the spacecraft to measure the drift. (Adapted from *Paschmann et al.* (2001)).

Both of the instruments experience problems in some regions of the magnetosphere. Fortunately, the problems occur in different regions for the two instruments, making them complement each other well. An extensive comparison between EDI and EFW has recently been carried out by *Eriksson et al.* (2006a). In short, EDI will evidently not function for too weak magnetic fields. It will also have problems for rapidly varying magnetic and electric fields, which can be encountered for example in the aurora regions. In these regions, EDI often also have problems with naturally accelerated auroral electrons of keV energy swamping the EDI detectors, thus making it impossible to identify the emitted beam electrons. EFW will have no problems in these regions, due to the construction with two spinning crossing booms, which allow high frequency measurements. On the other hand, EFW measurements can be affected by the influence of the positive potential of the satellite on the plasma environment. This is especially the case in cold, tenuous plasmas, where enhanced wakes may form.

5.3   Influence of wake on Cluster EFW

Comparisons with electron drift instruments on different spacecraft have shown that formation of a wake behind the spacecraft and booms can severely affect the measurement from double probe instruments (*Pedersen et al.*, 1984; *Bauer et al.*, 1983; *Eriksson et al.*, 2006a). The plasma is in most cases flowing perpendicular to the ambient electric field (in the $\boldsymbol{E} \times \boldsymbol{B}$ direction and also parallel to $\boldsymbol{B}$), which means that the spurious

wake electric field will be in this direction, *i.e.* transverse to the real ambient electric field (assuming the parallel electric fields are negligible).The wake will thus normally have more influence on the direction than of the amplitude of the measured transverse electric field. However, the wake induced field along $\boldsymbol{B}$ may be many orders of magnitude above any real parallel electric field. This is the case in *e.g.* the polar wind, where spurious electric fields due to wakes have been observed in Cluster data (*Eriksson et al.*, 2006a).

Wakes behind Cluster are common in the double-probe data, both in the solar wind and in outflowing cold tenuous plasma with ionospheric origin. As was described in section 4.2, the wakes in the solar wind are narrow and can therefore be easily detected in EFW data as a distinct peak when one of the probes passes the wake. In cold tenuous plasmas, where the wakes are enhanced, the situation is completely different: the wakes are so wide that the wake field cannot easily be sorted out from the background field and the EFW data is contaminated by the wake field. However, if EDI is operating well, it is possible to determine the size of this spurious field, which in some regions can reach up to 10 mV/m. In figure 5.4 electric field data from Cluster in the polar cap at a geocentric distance of 8.6 R_E is shown. In the upper panel the spacecraft potential is displayed, while the two lower panels show the electric field components E_x and E_y for EDI (blue) and EFW (red). The component E_x is almost aligned with the magnetic field lines, in the direction of the polar wind. E_y is perpendicular to E_x and consequently also roughly perpendicular to the polar wind. As can easily be seen, the measurements from EFW is mainly disturbed for E_x, thus in the direction of the polar wind. The errors also grow when the spacecraft potential increases. These two facts provide evidence for an enhanced wake behind the spacecraft, creating the spurious electric field in the EFW data.
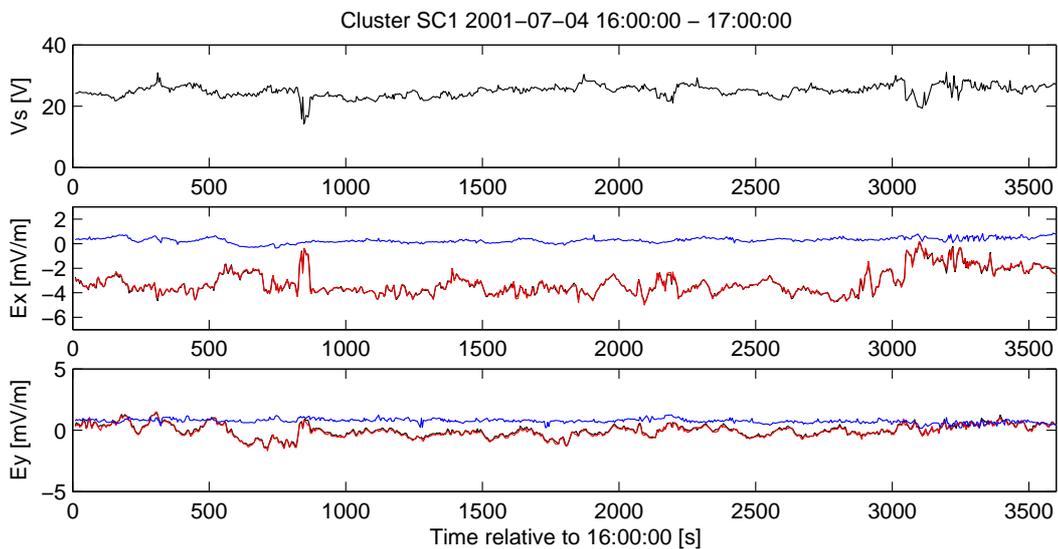
Figure 5.4: Electric field data from the polar cap at a geocentric distance of 8.6 R_{E}. The upper panel shows the spacecraft potential and the two lower panels show comparisons between two components of the electric field measured by EFW (red) and EDI (blue). E_x is in this case approximately aligned with the direction of the polar wind, while E_y is roughly perpendicular to this direction. Note that EFW experiences problems mainly in the E_x-direction and that the errors grow whe the spacecraft potential is high.

The formation of enhanced wakes and its influence on the EFW instrument is the subject of Paper I (*Engwall et al.*, 2006b) attached to this thesis. In this paper, we have made rough theoretical estimates of the size of the wake and performed numerical simulations of the wake formation. In Paper II (*Engwall and Eriksson*, 2006), we investigate in detail the influence of the wake on the spin signatures of EFW, the results of which can be useful for detection of wake fields in EFW data. The wake studies have paved the way for a new method using the spurious electric field, which was first seen merely as a complication, as a means to study cold ions. This method is described in Paper III (*Engwall et al.*, 2006a), as well as in chapter 6, where we also present results from a preliminary statistical study of the plasma flow in the magnetotail lobes. All three papers are summarized in more detail in chapter 7.

Chapter 6

Studying cold plasma flows with electric field instruments

6.1 A new method for measuring plasma flows

As has been described in section 2.3, it is difficult to measure the properties of magnetospheric low-energy ions, since they often do not possess enough energy to surmount the positive satellite potential. In the geomagnetic lobes, to date only *Su et al.* (1998) have been able to measure cold ion outflow at high altitude (8 R_{E}) using the Polar spacecraft.

By exploiting the wake forming behind the Cluster spacecraft, we have used electric field measurements to detect a large amount of cold flowing ions in the lobes from a few R_{E} from the Earth to as far as almost 20 R_{E}. We have also developed a new method for deriving the ion flow speed, based on the combination of a simple model of the wake electric field, $\mathbf{E}^{\mathrm{w}}$, and electric field data from EFW and EDI. This model requires that the ions are unmagnetised on the wake length scale, so that the wake field is in the flow direction,

$$\mathbf{E}^{\mathrm{w}} = \mathbf{E}^{\mathrm{EFW}} - \mathbf{E}^{\mathrm{EDI}} = g\mathbf{u}, \qquad (6.1)$$

where $\mathbf{u}$ is the flow velocity and the scalar g may be a function of, for example, the spacecraft potential, the ion temperature and the flow speed u, but should be independent of the flow direction. Moreover, we assume that the frozen-in condition apply and that EDI data and magnetic field data are good, so that the perpendicular drift velocity of the ions, $\mathbf{u}_\perp$, is given by

$$\mathbf{u}_\perp = \mathbf{E}^{\mathrm{EDI}} \times \mathbf{B}/B^2. \qquad (6.2)$$

Decomposing the wake field (equation 6.1) in a parallel and perpendicular component, we obtain

$$\mathbf{E}^{\mathrm{w}} = \mathbf{E}^{\mathrm{EFW}} - \mathbf{E}^{\mathrm{EDI}} = g\mathbf{u}_\perp + gu_\parallel \frac{\mathbf{B}}{B}. \qquad (6.3)$$

Since EFW and EDI have two common measured components (E_x and E_y), equation 6.3 yields two equations for the two unknowns g and $u_\parallel$:

$$\begin{cases} g = \frac{(\mathbf{B} \times \mathbf{E}^{\mathrm{w}})_z}{E_z^{\mathrm{EDI}}} = \frac{B_x E_y^{\mathrm{w}} - B_y E_x^{\mathrm{w}}}{E_z^{\mathrm{EDI}}} \\ u_{\parallel} = \frac{\mathbf{B} \cdot \mathbf{E}^{\mathrm{w}}}{gB} = \frac{E_x^{\mathrm{w}} B_x + E_y^{\mathrm{w}} B_y}{B_x E_y^{\mathrm{w}} - B_y E_x^{\mathrm{w}}} \frac{E_z^{\mathrm{EDI}}}{B} \end{cases} \tag{6.4}$$

This method can now be applied to cold plasma flows to derive the flow speed. In Paper III (*Engwall et al.*, 2006a), we present the method in more detail and apply it on a case in the geomagnetic tail at a geocentric distance of 18 R_{E}. At the same time, a particular spacecraft configuration, made it possible to measure the flow speed with the ion spectrometer CIS (*Rème et al.*, 2001) on-board another of the Cluster satellites. The results from our method and from the particle detector show good agreement, and even though we have only been able to make simultaneous measurements for one event, this is enough to confirm that the method actually works.

6.2   Initial statistical study of cold plasma flows

We have used our new method to make an initial statistical study of the cold plasma flows in the magnetotail lobes. The data is collected by Cluster SC1 during three months from August to October 2002, when the Cluster apogee is in the tail. We only consider data points in the orbit 20 hours before and after apogee. A limitation of the method is that EDI data is not always accessible for all passes through apogee, because of the low magnetic field strength in the central plasma sheet (see page 34). Figure 6.1 shows all data points[1], where we have been able to detect cold ions by examining the wake field. Our criterion for detection of cold ions is that the wake field, $\mathbf{E}^{\mathrm{w}} = \mathbf{E}^{\mathrm{EFW}} - \mathbf{E}^{\mathrm{EDI}}$, exceeds 2 mV/m. Black dots represents the events, where no cold ions have been detected, while the red dots show the detected cold ions. We have chosen to present these results in the GSM coordinate system, as the ion outflow mainly is along the magnetic field[2]. As we can see there is a large fraction of cold ions in the lobes.

In figure 6.2(a), we show the fraction of all events, where cold ions have been detected with two different criteria:

1. $\mathbf{E}^{\mathrm{w}} > 2$ mV/m (yellow and blue),

2. $\mathbf{E}^{\mathrm{w}} > 2$ mV/m, and $u_{\parallel} > 25$ km/s (yellow).

At high values of $|Z_{\mathrm{GSM}}|$ and with criterion 1, more than 80 % of the investigated data points show evidence of cold flowing ions. At lower values of $|Z_{\mathrm{GSM}}|$, there are fewer data points (see figure 6.1), since EDI data is missing to a large extent due to weak magnetic fields. However, of the observed data points in the central region, very few (around 15%) contain cold flowing ions. Thus, few wakes are detected in the plasma sheet, which is expected, as it is mainly filled with highly energetic plasma. The presence of a high energy plasma is likely to bring down the spacecraft potential and thus inhibit the formation of an enhanced wake which our method relies on. The yellow bars in figure 6.2(a) display cold ions detected with criterion 2, which shows that the velocity is higher for higher values of $|Z_{\mathrm{GSM}}|$.

---

[1]Each data point corresponds to 1 spacecraft spin.

[2]Note that the points in figure 6.1 do not show the ion orbits, but the parts of the Cluster orbits in GSM coordinates, where cold ions are observed.
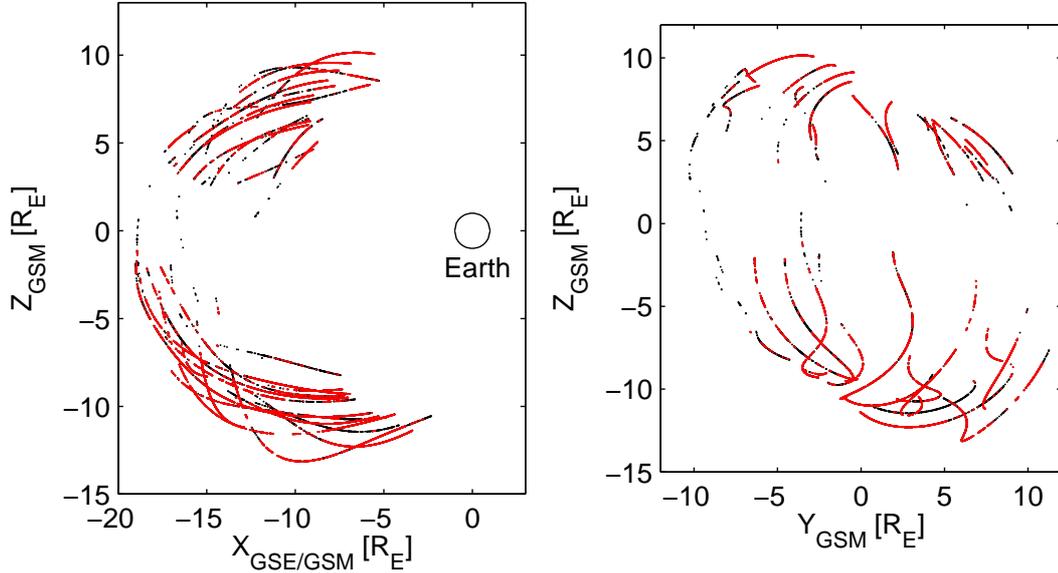
Figure 6.1: Detection of cold ions in the geomagnetic tail. Red dots show where cold ions have been detected with the method described in 6.1, while the black dots represent no detected ions. In a majority of the events, we detect cold ions.

In figure 6.2(b), we present the outward velocity distribution along the magnetic field. The mean speed is 29.4 km/s (red line) and the median speed is 21.8 km/s (green line). Figure 6.3(a) shows the corresponding outward flux of cold ions. The plasma density is inferred from the spacecraft potential measured by EFW (see figure 4.1) (*Pedersen et al.*, 2001)[3]. Both the outward speed and flux are close to the values from the polar wind survey with the Polar spacecraft reported by *Su et al.* (1998), even though our values are somewhat lower. One explanation for the lower speed in our study is that *Su et al.* (1998) probably miss a large part of the low-energy ions, as discussed in section 2.3.2.

The ionospheric mass loss of protons, M_{H+}^{Isph}, corresponding to the outward proton flux, F_{H+}, can be estimated as

$$M_{H+}^{Isph} = 2F_{H+}A_o, \qquad (6.5)$$

where F_{H+} is the observed flux and A_o the equivalent polar cap area at the observation site. The factor 2 accounts for the two polar caps. A_o is given from the conservation of magnetic flux, $A_o = A_{pc}\frac{B_{pc}}{B_o}$, where A_{pc} is the area of one polar cap, B_{pc} and B_o are

---

[3]It should be noted that there is some uncertainty in the relation between the plasma density and the spacecraft potential in tenuous plasmas, and the values of the outward flux should be taken as order of magnitude estimates. In an extended study, a more accurate calibration of the plasma density should be included.
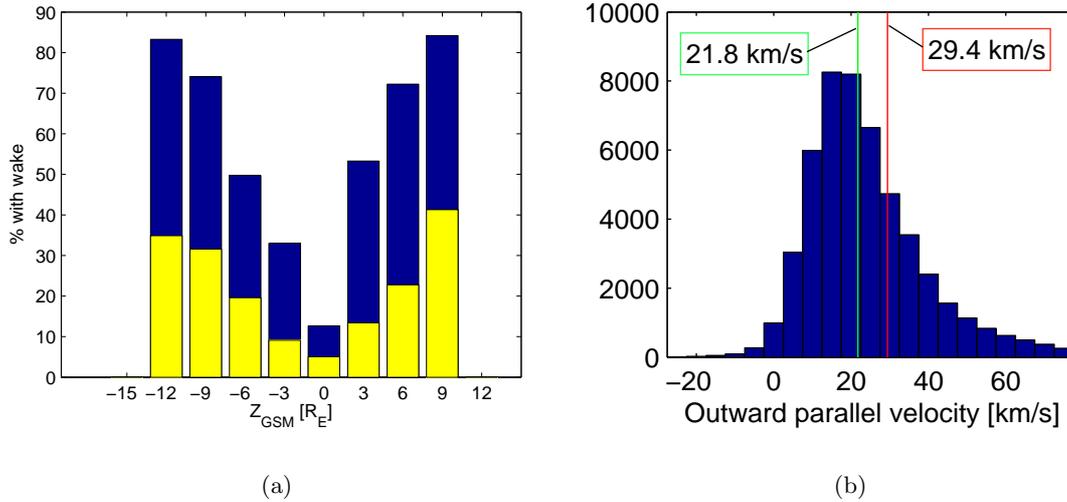
Figure 6.2: (a) Fraction of all events where cold ions have been detected as a function of Z_{GSM} using two different criteria: 1. $\mathbf{E}^{\mathrm{w}} > 2$ mV/m (yellow and blue), and 2. $\mathbf{E}^{\mathrm{w}} > 2$ mV/m, and $u_\parallel > 25$ km/s (yellow). (b) The outward velocity distribution along the magnetic field. The mean (red line) and median (green line) values are displayed.

the magnetic field strengths at the polar cap and at the observation site. In a rough estimation, we take $A_{\mathrm{pc}} = \pi(R_{\mathrm{E}} \sin 15°)^2$, $B_{\mathrm{pc}} = 31000$ nT and $B_{\mathrm{o}} = 20$ nT. With a flux around $4 \times 10^5 \mathrm{cm}^{-2}\mathrm{s}^{-1}$, we get a total mass loss close to the predicted 1 kg/s (see section 2.3.1).

To investigate the dependence of ionospheric outflows with magnetic activity, we have sorted the outflow data after K_{p} index[4]. As shown in figure 6.3(b), there is a strong dependence between outward flux and K_{p}, with higher outflow rates for high values of K_{p}. This is in accordance with the study of low-energy ion outflow between 6000 and 10000 km using the Akebono spacecraft (*Cully et al.*, 2003).

Even though we have only made a preliminary statistical investigation, the character of the results clearly shows the power of the method. When collecting our data set, we used only one of the four spacecraft and three months of operation, but nevertheless this provided us with 70,000 data points in the geomagnetic tail. For comparison, the total high-altitude database used by *Su et al.* (1998) contains less than 1000 data points. In addition, the Cluster data already holds the potential for investigating the outflows during half a solar cycle. Therefore, this study should be extended in future work. With four spacecraft and five years of data, our method opens up for new interesting information on cold plasma flows, such as the polar wind. The Cluster mission with its polar orbit is well suited to study the high-altitude polar wind, from the cleft to the far magnetotail. Such a study could well be important for the understanding of the dynamics of magnetospheric plasmas, as well as the total ion content in the magnetosphere.

---

[4]K_{p} index is a measurement of magnetic fluctuations and ranges from 0 (low activity) to 9 (high activity).
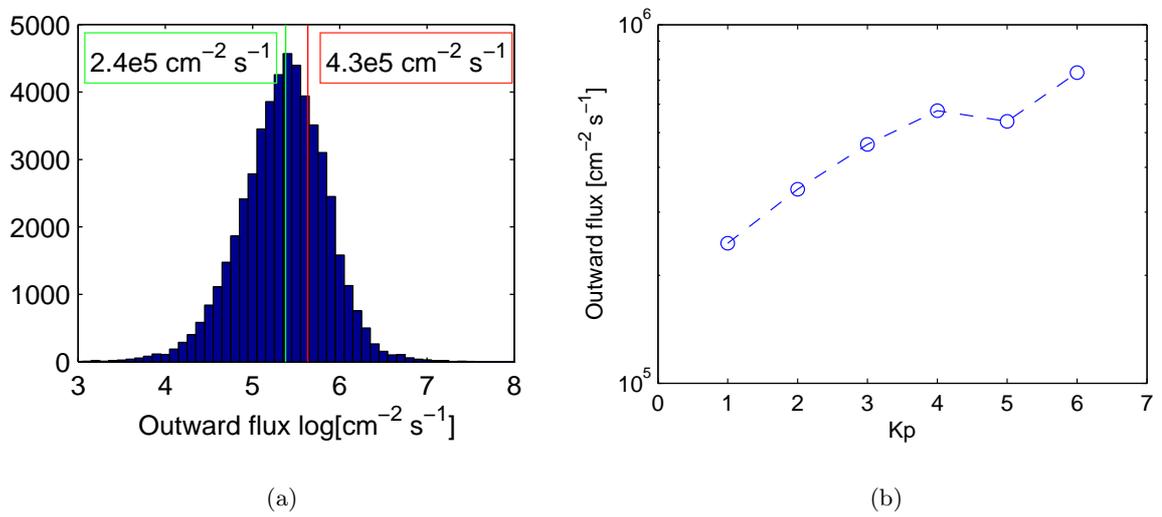
Figure 6.3: (a) The outward cold ion flux along the magnetic field. The mean (red line) and median (green line) values are displayed. (b) Outward flux as a function of K_p index.

Chapter 7

Summary of publications

7.1 Paper I: *Wake formation behind positively charged spacecraft in flowing tenuous plasmas*

Authors: E. Engwall, A. I. Eriksson, and J. Forest

Journal: *Physics of Plasmas*

Status: In review

We report results from a study of enhanced wake formation behind positively charged spacecraft in flowing tenuous plasmas using rough analytical estimates and numerical simulations. For the numerical simulations we have used the code package PicUp3D run on a common desktop PC.[1] These simulations have provided new knowledge on the size and shape of the wake, as well as scaling to different plasma parameters. The most evident results are that (a) a low ion temperature causes a large ion wake, and (b) a high electron temperature leads to a more negative potential in the wake. We have modeled the spacecraft body and the spacecraft booms separately, which makes it possible to investigate which part creates the largest wake. Even for very thin wire booms (thickness on the order of a few millimeters), the wake can grow very big, since the potential structure around the booms will increase the effective size of the obstacle to the plasma flow with three orders of magnitude. Around the spacecraft body the potential decreases much more quickly. This was evident in the simulations, showing a much more negative wake potential behind the booms than behind the spacecraft body.

Moreover, we have compared the simulation results to measurements from the Cluster double-probe instrument EFW, where we suspect influence from an enhanced wake (*Eriksson et al.*, 2006a). We have seen that the magnitude of the suspected wake field detected by EFW is consistent with the simulation results. The wake spin signatures of EFW have also been well reproduced by the simulations, further supporting the idea of enhanced wake formation behind Cluster.

---

[1] The PIC method and the PicUp3D code are described in more detail in *Engwall* (2004).

7.2 Paper II: *Double-probe measurements in cold tenuous space plasma flows*

Authors: E. Engwall and A. I. Eriksson

Journal: *IEEE Trans. Plasma Sci.*

Status: In review

In this paper we discuss the two main sources for spurious electric fields in double-probe measurements in cold flowing tenuous space plasmas: 1. asymmetric photoemission between probes and other electrical elements of the spacecraft, and 2. enhanced wakes. By performing a Fourier analysis of EFW spin data, we have found that the photoasymmetric field, E_{a}, can be represented by

$$E_{\mathrm{a}}(\theta) = E_{\mathrm{a}}^0 \cos\theta, \tag{7.1}$$

where θ is the angle between the boom and the direction to the Sun. The photoasymmetric field is often referred to as *apparent sunward field* or *sunward offset*. In the case of Cluster its amplitude is typically around 1 mV/m.

Furthermore, we assume that the wake field can be written as

$$E_{\mathrm{w}} = a_{\mathrm{w1}} \cos\theta_{\mathrm{b}} + a_{\mathrm{w3}} \cos(3\theta_{\mathrm{b}}) + a_{\mathrm{w5}} \cos(5\theta_{\mathrm{b}}), \tag{7.2}$$

where θ_{b} is the angle between the boom and the wake direction. Now, Fourier analysis of EFW spin data including wake effects makes it possible to determine the angle of the wake, as well as the Fourier coefficients a_{w1}, a_{w3} and a_{w5}. We have seen that the Fourier coefficients are dependent on satellite potential: the signatures become more sinusoidal for higher satellite potentials, which is expected for an enhanced wake field.

7.3 Paper III: *Low-energy (order 10 eV) ion flow in the magnetotail lobes inferred from spacecraft wake observations*

Authors: E. Engwall, A. I. Eriksson, M. André, I. Dandouras, G. Paschmann, J. Quinn, and K. Torkar

Journal: *Geophysical Research Letters*

Status: Accepted

We present a case study of cold ions in the magnetotail lobes at 18 R_{E} detected by Cluster. The ions are so low in energy (order 10 eV) that they are not normally detectable by ordinary particle instruments due to high positive spacecraft potentials (40-60 V). However, for this event, artificial spacecraft potential control reduces the spacecraft potential to around +7 V and the Cluster ion detector is in a special low-energy mode, making it possible to measure the cold ions. At the same time we are able to detect and derive the flow velocity of the cold ions using electric field instruments. The method is based on the fact that an enhanced wake is formed behind a positively charged spacecraft in a flowing tenuous plasma as described in section 6.1.

The flow measurements using both methods are in accordance with the polar wind survey at 8 R_E by *Su et al.* (1998), confirming the continuation of low-energy ion outflows to at least 18 R_E. The good agreement between the two methods shows that a simple model of the wake field in combination with electric field data from double-probe and electron drift instruments can be used to estimate the flow velocity of low-energy, supersonically flowing ions.

Acknowledgements

Bibliography

Abe, T., B. A. Whalen, A. W. Yau, R. E. Horita, S. Watanabe, and E. Sagawa, EXOS-D (Akebono) SMS observations of the polar wind, *Journal of Geophysical Research*, *98*, 11,191–11,203, 1993.

Abe, T., S. Watanabe, B. A. Whalen, A. W. Yau, and E. Sagawa, Observations of polar wind and thermal ion outflow by Akebono/SMS, *Journal of Geomagnetism and Geoelectricity*, *48*, 319–325, 1996.

Axford, W. I., The polar wind and the terrestrial helium budget, *Journal of Geophysical Research*, *73*, 6855–6859, 1968.

Banks, P. M., and T. E. Holzer, The polar wind, *Journal of Geophysical Research*, *73*(21), 6846–6854, 1968.

Bauer, O. H., R. Grard, G. Haerendel, and A. Pedersen, Influence of wake and photoemission on electric field measurements with a double probe on GEOS-2, in *Spacecraft/Plasma Interactions and their Influence on Field and Particle Measurements*, ESA SP-198, pp. 51–56, 1983.

Chappell, C. R., T. E. Moore, and J. H. Waite, The ionosphere as a fully adequate source of plasma for the Earth's magnetosphere, *Journal of Geophysical Research*, *92*(11), 5896–5910, 1987.

Chappell, C. R., B. L. Giles, T. E. Moore, D. C. Delcourt, P. D. Craven, and M. O. Chandler, The adequacy of the ionospheric source in supplying magnetospheric plasmas, *Journal of Atmospheric and Solar-Terrestrial Physics*, *62*, 421–436, 2000.

Chen, F. F., *Introduction to Plasma Physics and Controlled Fusion*, 2nd ed., Plenum Press, New York, 1984.

Chen, S.-H., and T. E. Moore, Dayside flow bursts in the Earth's outer magnetosphere, *Journal of Geophysical Research*, *109*, doi: 10.1029/2003JA010007, 2004.

Cully, C. M., E. F. Donovan, A. W. Yau, and G. G. Arkos, Akebono/Suprathermal Mass Spectrometer observations of low-energy ion outflow: Dependence on magnetic activity and solar wind conditions, *Journal of Geophysical Research*, *108*, doi: 10.1029/2001JA009200, 2003.

Décréau, P. M. E., et al., Early results from the WHISPER instrument on Cluster: an overview, *Annales Geophysicae*, *19*, 1241–1258, 2001.

Engwall, E., Numerical studies of spacecraft-plasma interaction: Simulations of wake effects on the Cluster electric field instruments EFW, *IRF Scientific Report 284*, Swedish Institute of Space Physics, http://www.irf.se/Publications/, 2004.

Engwall, E., and A. I. Eriksson, Double-probe measurements in cold flowing tenuous space plasmas, *IEEE Trans. Plasma Sci.*, in review, 2006.

Engwall, E., A. I. Eriksson, M. André, I. Dandouras, G. Paschmann, J. Quinn, and K. Torkar, Low-energy (order 10 ev) ion flow in the magnetotail inferred from spacecraft wake observations, *Geophysical Research Letters*, accepted, 2006a.

Engwall, E., A. I. Eriksson, and J. Forest, Wake formation behind positively charged spacecraft in flowing tenuous plasmas, *Physics of Plasmas*, in review, 2006b.

Eriksson, A., et al., Electric field measurements on Cluster: Comparing the double-probe and electron drift technique, *Annales Geophysicae*, in press, 2006a.

Eriksson, A. I., L. Wedin, J.-E. Wahlund, and B. Holback, Analysis of Freja charging events: Modelling of Freja observations by spacecraft charging codes, *IRF Scientific Report 252*, Swedish Institute of Space Physics, 1999.

Eriksson, A. I., et al., RPC-LAP: The Rosetta Langmuir probe instrument, *Space Sci. Rev., in review*, 2006b.

Escoubet, C. P., A. Pedersen, R. Schmidt, and P. A. Lindqvist, Density in the magnetosphere inferred from ISEE 1 spacecraft potential, *Journal of Geophysical Research*, *102*, 17,595–17,609, 1997.

Escoubet, C. P., M. Fehringer, and M. Goldstein, The Cluster mission, *Annales Geophysicae*, *19*, 1197–1200, 2001.

Etcheto, J., and A. Saint-Marc, Anomalously high plasma densities in the plasma sheet boundary layer, *Journal of Geophysical Research*, *90*, 5338–5344, 1985.

Fahleson, U., Theory of electric field measurements conducted in the magnetosphere with electric probes, *Space Science Reviews*, *7*, 238–262, 1967.

Garrett, H. B., The charging of spacecraft surfaces, *Reviews of Geophysics and Space Physics*, *19*(4), 577–616, 1981.

Goldstein, H., C. Poole, and J. Safko, *Classical Mechanics*, 3rd ed., Addison Wesley, San Fransisco, 2002.

Gombosi, T. I., *Physics of the Space Environment*, Cambridge University Press, Cambridge, 1998.

Grard, R. J. L., Properties of the satellite photoelectron sheath derived from photoemission laboratory measurements, *Journal of Geophysical Research*, *78*, 2885–2906, 1973.

Gustafsson, G., et al., The Electric Field and Wave Experiment for the Cluster Mission, *Space Science Reviews*, *79*, 137–156, 1997.

Gustafsson, G., et al., First results of electric field and density observations by Cluster EFW based on initial months of operation, *Annales Geophysicae*, *19*, 1219–1240, 2001.

Hoffman, J. H., Studies of the composition of the ionosphere with a magnetic deflection mass spectrometer, *International journal of mass spectrometry and ion physics*, *4*, 315–322, 1970.

Hoffman, J. H., and W. H. Dodson, Light ion concentrations and fluxes in the polar regions during magnetically quiet times, *Journal of Geophysical Research*, *85*(14), 626–632, 1980.

Hoffman, J. H., W. H. Dodson, C. R. Lippincott, and H. D. Hammack, Initial ion composition results from the ISIS 2 satellite, *Journal of Geophysical Research*, *79*(18), 4246–4251, 1974.

Kivelson, M. G., and C. T. Russel, *Introduction to Space Physics*, Cambridge University Press, Cambridge, 1995.

Laakso, H., T. L. Aggson, and R. Pfaff Jr., Plasma gradient effects on double probe measurements in the magnetosphere, *Annales Geophysicae*, *13*, 130–146, 1995.

Lockwood, M., M. O. Chandler, J. L. Horwitz, J. H. Waite Jr., T. E. Moore, and C. R. Chappell, The cleft ion fountain, *Journal of Geophysical Research*, *90*, 9736–9748, 1985.

Matsui, H., T. Mukai, S. Ohtani, K. Hayashi, R. C. Elphic, M. F. Thomsen, and H. Matsumoto, Cold dense plasma in the outer magnetosphere, *Journal of Geophysical Research*, *104*, 25,077–25,095, 1999.

Medicus, G., Theory of electron collection of spherical probes, *Journal of Applied Physics*, *32*, 2512–2520, 1961.

Medicus, G., Spherical Langmuir probe in "drifting" and "accelerated" Maxwellian distribution, *Journal of Applied Physics*, *33*, 3094–3100, 1962.

Moore, T. E., et al., High-altitude observations of the polar wind, *Science*, *277*, 349–351, 1997.

Moore, T. E., et al., Polar/TIDE results on polar ion outflows, in *Sun-Earth Plasma Connections*, Geophysical Monograph 109, pp. 87–101, American Geophysical Union, 1999.

Mott-Smith, H., and I. Langmuir, The theory of collectors in gaseous discharges, *Physical Review*, *28*, 727–763, 1926.

Mozer, F. S., Analyses of techniques for measuring DC and AC electric fields in the magnetosphere, *Space Science Reviews*, *14*, 272–313, 1973.

Nagai, T., J. H. Waite, J. L. Green, C. R. Chappell, R. C. Olsen, and R. H. Comfort, First measurements of supersonic polar wind in the polar magnetosphere, *Geophysical Research Letters*, *11*, 669–672, 1984.

Orsini, S., M. Candidi, M. Stockholm, and H. Balsiger, Injection of ionospheric ions into the plasma sheet, *Journal of Geophysical Research*, *95*, 7915–7928, 1990.

Parks, G. K., *Physics of Space Plasmas*, 2nd ed., Addison Wesley, Redwood City, 1991.

Paschmann, G., C. E. McLlwain, J. M. Quinn, R. B. Torbert, and E. C. Whipple, The Electron Drift Technique for Measuring Electric and Magnetic Fields, in *Measurement Techniques in Space Plasmas: Fields*, Geophysical Monograph 103, pp. 29–38, American Geophysical Union, 1998.

Paschmann, G., et al., The Electron Drift Instrument on Cluster: overview of first results, *Annales Geophysicae*, *19*, 1273–1288, 2001.

Pedersen, A., Solar wind and magnetosphere plasma diagnostics by spacecraft electrostatic potential measurements, *Annales Geophysicae*, *13*, 118–121, 1995.

Pedersen, A., C. A. Cattell, C.-G. Fälthammar, V. Formisano, P.-A. Lindqvist, F. Mozer, and R. Torbert, Quasistatic electric field measurements with spherical double probes on the GEOS and ISEE satellites, *Space Science Reviews*, *37*, 269–312, 1984.

Pedersen, A., F. Mozer, and G. Gustafsson, Electric field measurements in a tenuous plasma with spherical double probes, in *Measurement Techniques in Space Plasmas: Fields*, Geophysical Monograph 103, pp. 1–12, American Geophysical Union, 1998.

Pedersen, A., P. Décréau, P. Escoubet, G. Gustafsson, H. Laakso, P.-A. Lindqvist, B. Lybekk, F. Mozer, and A. Vaivads, Four-point high time resolution information on electron densities by the electric field experiments (EFW) on Cluster, *Annales Geophysicae*, *19*, 1483–1489, 2001.

Rème, H., et al., First multispacecraft ion measurements in and near the Earth's magnetosphere with the identical Cluster ion spectrometry (CIS) experiment, *Annales Geophysicae*, *19*, 1303–1354, 2001.

Sandahl, I., *Norrsken - Budbärare från rymden*, Atlantis, Stockholm, 1998.

Sauvaud, J.-A., et al., Intermittent thermal plasma acceleration linked to sporadic motions of the magnetopause, first Cluster results, *Annales Geophysicae*, *19*, 1523–1532, 2001.

Sauvaud, J.-A., et al., Case studies of the dynamics of ionospheric ions in the Earth's magnetotail, *Journal of Geophysical Research*, *109*, doi: 10.1029/2003JA009996, 2004.

Schunk, R. W., Ionospheric outflow, in *Sun-Earth Plasma Connections*, Geophysical Monograph 109, pp. 195–206, American Geophysical Union, 1999.

Schunk, R. W., and J. J. Sojka, Global ionosphere-polar wind system during changing magnetic activity, *Journal of Geophysical Research*, *102*, 11,625–11,651, 1997.

Seki, K., R. C. Elphic, M. F. Thomsen, J. Bonnell, J. P. McFadden, E. J. Lund, M. Hirahara, T. Terasawa, and T. Mukai, A new perspective on plasma supply mechanisms to the magnetotail from a statistical comparison of dayside mirroring O^+ at low altitudes with lobe/mantle beams, *Journal of Geophysical Research (Space Physics)*, *107*, 7–1, doi:10.1029/2001JA900122, 2002.

Seki, K., et al., Cold ions in the hot plasma sheet of Earth's magnetotail, *Nature*, *422*, 589–591, 2003.

Su, Y.-J., J. L. Horwitz, T. E. Moore, B. L. Giles, M. O. Chandler, P. D. Craven, M. Hirahara, and C. J. Pollock, Polar wind survey with the Thermal Ion Dynamics Experiment/Plasma Source Instrument suite aboard POLAR, *Journal of Geophysical Research*, *103*, 29,305–29,337, 1998.

Torkar, K., et al., An experiment to study and control the Langmuir sheath around INTERBALL-2, *Annales Geophysicae*, *16*, 1086–1096, 1998.

Torkar, K., et al., Active spacecraft potential control for Cluster - implementation and first results, *Annales Geophysicae*, *19*, 1289–1302, 2001.

Wahlund, J.-E., et al., Cassini measurements of cold plasma in the ionosphere of Titan, *Science*, *308*, 986–989, 2005.

Yau, A. W., and M. André, Sources of ion outflow in the high latitude ionosphere, *Space Science Reviews*, *80*, 1–25, 1997.

Paper I
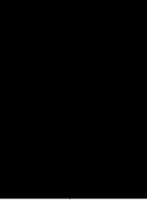
Wake formation behind positively charged spacecraft in flowing tenuous plasmas

E. Engwall

Department of Astronomy and Space Physics, Uppsala University, Sweden and
Swedish Institute of Space Physics, Uppsala, Sweden

A. I. Eriksson

Swedish Institute of Space Physics, Uppsala, Sweden

J. Forest

Swedish Institute of Space Physics, Kiruna, Sweden and
Artenum Company, Paris, France
(Dated: March 10, 2006)

Spacecraft in tenuous plasmas become positively charged because of photoelectron emission. If the plasma is supersonically drifting with respect to the spacecraft, a wake forms behind it. When the kinetic energy of the positive ions in the plasma is not sufficient to overcome the electrostatic barrier of the spacecraft potential, they scatter on the potential structure from the spacecraft rather than get absorbed or scattered by the spaceraft body. For tenuous plasmas with Debyelenghts much exceeding the spacecraft size, the potential structure extends farfram the spacecraft, and consequently the wake is in this case of transverse dimensions much larger than the spacecraft. This enhanced wake formation process is demonstrated by theoretical analysis and computer simulations. Comparison to observations from the Cluster satellites show good agreement.

I. INTRODUCTION

When a spacecraft moves through a plasma at a relative speed exceeding the ion thermal speed in the plasma, a wake will form behind it. Since in the space plasmas where this happens usually $T_i \sim T_e$, so that the spacecraft also moves faster than ion acoustic waves, we refer to this motion as supersonic. Motion supersonic with respect to electrons as well as ions is rare: the typical case is the mesosonic flow, where the spacecraft is supersonic with respect to the ions but subsonic with respect to the electrons. The wake thus becomes negatively charged, due to the thermal motion of the electrons.

Mesosonic spacecraft motion, and hence the occurrence of a negatively charged wake behind the spacecraft, is very common. The prime examples are the ionosphere and solar wind. In the ionosphere, typical spacecraft move at speeds around 7 km/s in a plasma with ion thermal speed on the order of 4 km/s for protons and 0.25 km/s for oxygen. In the solar wind, a flow speed of 400 km/s and proton thermal speed of 40 km/s are typical values. Less obvious regions of mesosonic spacecraft motion are the polar cap and tail lobes of the Earth's magnetosphere. These regions are sometimes thought of as essentially void of plasma, but are often filled with a very tenuous (~ 0.1 cm^{-3}) but mesosonic cold plasma outflow from the ionosphere, driven by e.g. the polar wind or cleft ion fountain[1–3]. Electric field measurements on the Cluster satellites have shown regular occurrence of wakes in these regions[4].

The three regions mentioned presents three different regimes for wake formation. In the ionosphere, the spacecraft potential with respect to the surrounding plasma, V_{sc}, usually is negative and a few times the electron temperature T_e in magnitude, due to the higher mobility of

electrons. This case has been studied for a long time, and a substantial literature has built up over the years. An old, but still very useful summary was provided by *Al'pert et al.*[5], with a review of later work given by *Hastings*[6]. One of the results is that the negative potential structure, from the spacecraft itself as well as from the negatively charged wake, focuses ions into the wake, enhancing the filling-in of the wake.

The solar wind is much more tenuous than the ionosphere (typically 5 cm^{-3}), implying that the electrons randomly collected by the spacecraft gives a current much smaller than the photoemission current from the sunlit spacecraft. The result is positive values of V_{sc}, typically on the order of 5 - 10 V. This is so much lower than the ion flow kinetic energy of typically 1 keV (protons) that the charge of the spacecraft is quite irrelevant for the wake formation, and the elongated wake forming behind the spacecraft has its width determined by the spacecraft dimensions [see Figure 1(a)]. Much existing work on theory and simulation of wake formation behind ionospheric spacecraft is relevant for this situation as well.

The case of tenuous mesosonic plasma flows in the terrestrial magnetosphere is quite different. In the very tenuous plasmas of the polar cap and tail lobe regions (~ 0.1 cm^{-3} or less), the spacecraft potential often goes above 20 V positive, sometimes as high as 50 V or more[7]. Ion flow energies often stay at much lower values, around 10 eV, with temperatures of a few eV[3]. In this case, i.e. when

$$KT_i < \frac{m_i u^2}{2} < eV_{sc}, \qquad (1)$$

the ions will scatter on the repulsive potential distribution from the spacecraft. The wake size transverse to the
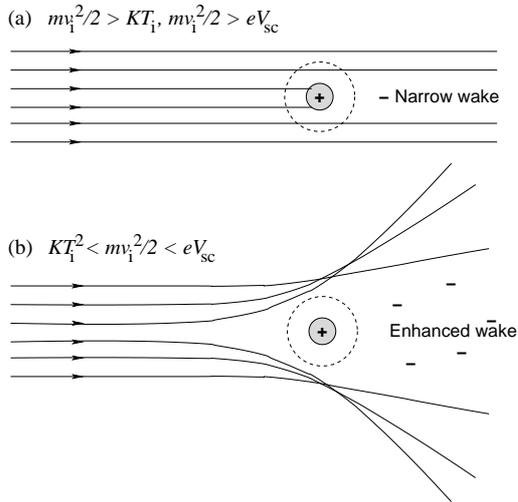
FIG. 1: Sketch of wake formation in mesosonic flows. (a) For ion flow energies higher than the spacecraft potential, V_{sc}, the wake has the typical transverse size of the spacecraft (narrow wake case). (b) For ion flow energy below V_{sc}, ions will scatter off the positive electrostatic potential from the spacecraft, creating an enhanced wake.

flow can thus be substantially larger than the spacecraft body itself [see Figure 1(b)]. We call such a wake an enhanced wake.

In contrast to the large literature on wakes behind negatively charged spacecraft, relevant to the ionosphere, very few studies address wake formation behind positive spacecraft, and only one of them concerns the case described by relation 1. The very earliest theoretical studies on spacecraft wake formation treated the case of a wake behind a point charge[8] or line charge[9] in a mesosonic plasma flow in a formalism appliccable also for positive charges. As the obstacles in these cases are infinitesimally small, while the calculated wake has a Debye scale width, these studies catch an important feature of the enhanced wake discussed above. However, the assumption of small potentials, $|V_{sc}| \ll m_i u^2/2$, means that they cannot be directly used for quantitative study of wakes in the situation described by relation 1. The same limitation applied to the laboratory study of wakes behind thin cylinders by *Hester and Sonin*[10], which included an experiment with positive cylinder potentials, $eV_{sc} \approx 3\,KT_e \approx 300\,KT_i \approx m_i u^2/20$. Despite the low potential of the obstacle, they detected an ion void significantly larger than the geometrical size of the obstacle. The elements of an enhanced wake, still in the small potential limit, can also be seen in the results of a simulation of a spherical Langmuir probe in a flowing plasma by *Singh and Chagani*[11]. The only studies of the case 1 that we are aware of are the simulations of spacecraft in the polar wind flow by *Zinin et al.*[12] and in a cometary coma by *Roussel and Berthelier*[13]. However, in both cases the plasma has a Debye length much below the spacecraft size, which means that the wake is not significantly en-

hanced by the electrostatic field around the spacecraft.

In spacecraft applications, the possibility of enhanced wakes was suggested by *Bauer et al.*[14] and *Pedersen et al.*[15] to explain particular features of electric field data from the ISEE (International Sun-Earth Explorer) and GEOS (GEOstationary Scientific Satellite) satellites. More recently, *Eriksson et al.*[4] established the presence of enhanced wakes in electric field data from the Cluster satellites. In parallel, we have done the numerical simulations presented in the present paper, using the Cluster data for comparison and verification.

Following this introduction, we discuss enhanced wake formation in Section 2, and the results from the computer simulations are presented in Section 3. In Section 4 we compare the results from theory and simulations to Cluster data in which the wake is detected.

II. ENHANCED WAKE FORMATION

The condition for enhanced wake formation (see Equation 1) ensures that the size of the wake will not be determined directly by the spacecraft's physical structure, but by the equipotential surface, where $\Phi \approx m_i u^2/(2e)$, which few ions can overcome. If we assume vacuum conditions, the characteristic transverse dimension of a spherical spacecraft of radius r at 20 V in a plasma with a flow energy of 5 V will increase from πr^2 to $16\pi r^2$, because the 5 V equipotential is at a distance of $4\,r$ from the center of the spacecraft. This 16-fold increase in obstacle area may seem dramatic, but even more so is the effect on long booms, with which many spacecraft are equipped mainly for measurements of electric fields. Assuming these booms behave like infinite cylinders of radius a in vacuum, except that the potential goes to exactly zero at a distance of $g\lambda_D$, where $g > 1$ is a real number, the potential field at a radial distance r from a wire boom at potential V is:

$$\Phi(r) = V\frac{\ln(r) - \ln(g\lambda_D)}{\ln(a) - \ln(g\lambda_D)}. \qquad (2)$$

From this, we can obtain the radial distance r_b at which $\Phi(r_b) = bV$, where $0 < b < 1$, as

$$r_b = a^b (g\lambda_D)^{(1-b)}. \qquad (3)$$

As an example, let us consider the Cluster wire booms with 88 m tip-to-tip separation and $a = 1.1$ mm, a Debye length of 15 m, and an arbitrary but reasonable choice of $g = 2$. This gives $r = 2.3$ m for the 5 V equipotential around a wire boom at 20 V. The effective size of the booms at right angles to the flow therefore increases from 2.2 mm to 4.6 m, i.e. by three orders of magnitude. This increase depends to some extent on the choice of g, but the effect is certainly significant for all realistic values of g. It is therefore possible that long antennas, which

normally are negligible due to their small thickness, can become significant obstacles to the plasma flow in the conditions described by Equation (1).

How large can the potentials be in the cold, tenuous plasma wake behind the booms? Considering a wake of slab-like geometry with thickness $d \ll \lambda_{\mathrm{D}}$, we may assume perfect exclusion of ions and no effect on the electrons. Solving Poisson's equation gives a maximum potential in such a wake of $\Phi_{\mathrm{wake}} = (d/\lambda_{\mathrm{D}})^2 KT_{\mathrm{e}}/e$. For a wake of thickness $d \sim \lambda_{\mathrm{D}}$ or larger, the potential saturates at $\Phi_{\mathrm{wake}} \sim KT_{\mathrm{e}}/e$, as further accumulation of electrons is inhibited at larger potentials. The small wake arising behind the booms, for which d is on the order of millimeters, in for example the solar wind ($\lambda_{\mathrm{D}} \sim 1$ m), thus cannot give rise to appreciable potentials. However, significant wake charging will arise in the case of $KT_{\mathrm{i}} < \frac{m_{\mathrm{i}} u^2}{2} < eV_{\mathrm{sc}}$. This wake field may significantly affect the measurements made by a double-probe instrument, as will be discussed in Section IV. To provide a more reliable basis for estimates regarding wake formation behind booms and its size, we must turn to simulations. Simulations also provide information on the more geometrically complex wake structure behind the spacecraft body itself.

III. SIMULATIONS OF THE ENHANCED WAKE FORMATION

A. Code and modeling

For modeling of the wake effect behind positively charged spacecraft, we used the open source simulation JAVA-based code package PicUp3D[19], which implements the Particle-In-Cell method (PIC)[20] to solve electrostatic spacecraft–plasma interaction problems. PicUp3D is designed for desktop PCs and was run on a dual-processor computer (2×2.40 GHz) with 2 GB RAM. A number of simulations were carried out to examine the wake formation. Results are presented for simulations with two different spacecraft geometries. In the first simulations we modeled only the spacecraft body, while in the other simulations we investigated the effects of long booms, neglecting the effects of the spacecraft body. We used the dimensions of the Cluster spacecraft in our simulations. They are cylindrical with a radius of 1.45 m and a height of 1.5 m. The distance between the boom tips is 88 m. Both the spacecraft surface and a large part of the booms are conductive, so that they are at the same potential (henceforth denoted spacecraft potential, V_{sc}). The last 3 m of the booms closest to the probes consists of different electrical elements at potentials closer to the plasma potential, in order to make the electric field measurements more accurate[21].

The input parameters for the simulations are chosen to be consistent with high altitude polar wind conditions derived from the POLAR satellite data presented by *Su et al.*[3] as well as with Cluster observations in the polar wind[22]. Table I gives the implemented simulation parameters. With these plasma parameters the Debye length is in the range $\lambda_{\mathrm{D}} \approx 12 - 24$ m and the electron plasma frequency $\omega_{\mathrm{pe}}/2\pi \approx 4 - 6$ kHz. The ion flow defines the positive y-direction. The integration time steps of all simulations were chosen in such a way that $v_{\mathrm{max}} \Delta t < 0.25 \Delta r$, where v_{max} is the maximal velocity of any particle, and Δr and Δt the spatial and temporal step sizes, respectively. This ensures that no particle can cross a cell in less than a few time steps. The presented results are averaged over 30 $\omega_{\mathrm{pe}}^{-1}$ when the solution has reached steady state in order to reduce statistical noise. To speed up the simulations we used a mass ratio of $m_{\mathrm{i}}/m_{\mathrm{e}} = 100$, while the ion kinetic energy remains unchanged. As will be shown in section 3.4, this does not change the wake structure close to spacecraft, but only the filling-in of ions farther downstream.

Plasma density, n_0 [cm^{-3}]	0.2, 0.4
Electron temperature, KT_{e} [eV]	1.0, 2.0
Ion temperature, KT_{i} [eV]	1.0, 2.0
Ion drift kinetic energy, $m_{\mathrm{i}} u^2/2$ [eV]	10
Spacecraft potential, V_{sc} [V]	20, 35
Magnetic field, B [nT]	0

TABLE I: Simulation parameters.

The magnetic field in magnetospheric regions with cold, tenuous plasmas is normally very low (typically 100 nT) and was neglected in the simulations. This can be justified by the very large Larmor radii (several km) for the two dominant ion species in the polar wind (H$^+$ and O$^+$). The electron Larmor radius of a few tens of meters is closer to the scale of the problem. Assuming the electrons to be unmagnetized may lead to overestimation of the electron densities in the wake. Since the flow of electrons is subsonic, this problem should, however, be small.

For simplicity, in none of the cases were photoelectrons included in the simulations. This approximation can be justified by the high potential of the spacecraft ($20 - 35$ V), which means that it will recollect most of the emitted photoelectrons, whose typical energies are a few eV[23]. The photoelectrons will thus never build up any appreciable space charge around the spacecraft, and therefore the vacuum potential is a very good approximation.

PicUp3D uses a rectangular grid and Dirichlet boundary conditions, which have a great advantage in their easy implementation, but special care must be taken to ensure that the final results are not influenced substantially. The Dirichlet boundary conditions on the walls of the computational box ($\Phi_b = 0$) can affect the derivation of the potential in the rest of the box, if the walls of the box are too close to the spacecraft. Theoretically, the walls should not be closer to the spacecraft than a few λ_{D}, in order to allow the Debye shielding to decrease the potential to a satisfactorily low level. This assump-

tion was verified numerically for different sizes of computational boxes. On the inner boundary, i.e. at the spacecraft border, the potential is set as an input parameter, and is not calculated self-consistently. The fixed spacecraft potential is of no concern in our case, as the spacecraft potential is related to the plasma density. For Cluster, *Pedersen et al.*[7] extracted a density–potential relation from data. We can thus choose a potential which is consistent with this relation. The rectangular grid can be problematic, since the grid size should be sufficiently small in order to reflect the details of the spacecraft–plasma interactions. On the other hand, the computational box has to be sufficiently large due to the impact on the potential distribution of the Dirichlet boundary conditions. For a detailed description, a large number of computational cells are therefore needed, which leads to long computational times. Thus, the grid size is a compromise between the requirement for a detailed description and reasonable computational times. To be able to resolve finer structures of the booms we implemented an analytical approximation, namely the *effective potential*, which is discussed in Section III C

B. Spacecraft body simulations

To obtain an idea of the wake formation behind the spacecraft body, we ran six reference simulations with different polar wind parameters (see Table II). The drift energy of the ions was 10 eV for all simulations, which is well below the values of the spacecraft potential in Table II. To ensure small effects of the boundary conditions on the final results, the size of the computational box was chosen such that its walls were at least 3 λ_D from the satellite and 1 λ_D from the points where the booms would end if they were included. (The reason for considering the booms, althought they are not included in these calculations, was that we wanted to see the signature that would be obtained in a double-probe electric field instrument, which uses such wire booms.) In the downstream direction the wall was placed at least 10 λ_D away from the satellite to avoid effects of the boundaries on the wake at large distances from the spacecraft.

In all simulations the grid size was $2.7 \times 2.7 \times 1.35$ m^3, resulting in different numbers of computational cells for different Debye lengths. The spacecraft was modeled as a rectangular box with the same dimensions as the grid, which approximates the cylindrical Cluster spacecraft with a diameter of 2.9 m and height of 1.5 m fairly well. In general, the average number of particles per cell is 8, which gives a reasonable accuracy. For the first simulation the number of particles was increased to 100 particles per cell to investigate the effects of particle number on numerical noise. The overall picture remained the same, while the detailed structure of the wake was smoother due to better statistics. Since the computational time increases with increasing number of macroparticles, while the noise is proportional to $1/\sqrt{N_{\text{macro}}}$[24],

it is costly to reduce the noise. For our purposes, 8 particles per cell gives sufficient accuracy.

Figure 2 shows results from Simulation 1 in Table II. As expected, there is a clearly visible wake in the ion density behind the spacecraft. The dominating potential structure is the decaying potential around the spacecraft, giving essentially spherical equipotentials down to 1 V. Behind the spacecraft a negatively charged wake is formed, reaching a minimum potential of -0.34 V.
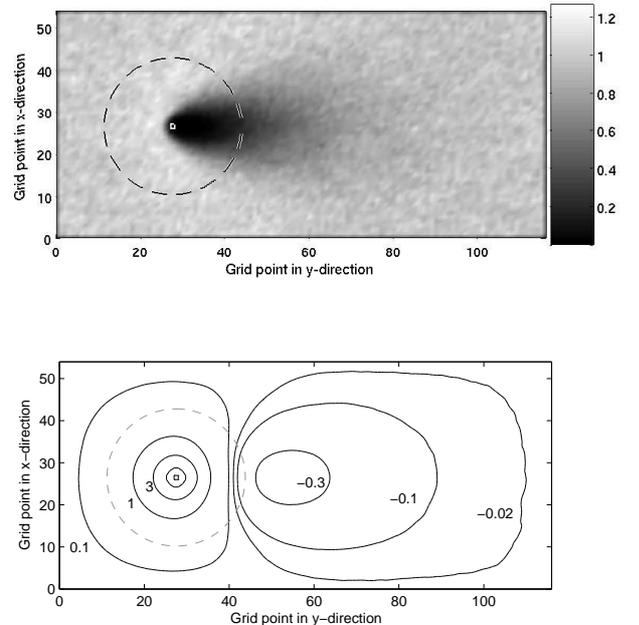
FIG. 2: Averaged normalized density of ions and potential between 20 ω_{pe}^{-1} and 50 ω_{pe}^{-1}. The dashed circles show the location of the Cluster EFW probes throughout a spin period. (The grid spacing is 2.7 m.) (a) Ion density in the $x-y$-plane through the spacecraft. (The white square shows the location of the spacecraft.) (b) Potential in the $x-y$-plane through the spacecraft ($V_{\text{sc}} = 35$ V). The minimum value of the potential in the wake is -0.34 V. Equipotential contours are given at -0.3, -0.1, -0.01, 0.1, 1, 3, 10 and 35 V.

The results from all six simulations are shown in Table II, where characteristics of the wake, such as depth (in volts), length, width, and height (in meters), are given. We defined two different criteria to determine the borders of the wake, using the potential (Φ) and the ion density (n_i). For the ion density, the surface where the ion density has decreased to 75 % of its background density was used, whereas for the potential we used the equipotential of -0.1 V.

It can clearly be seen that the size of the wake decreases with increasing ion temperature and decreasing electron temperature, which is as expected. A high ion temperature allows the ions to diffuse behind the spacecraft more quickly. Low electron temperatures result in a smaller potential in the wake. Moreover, at low electron

Simulation	n_0 [cm^{-3}]	V_{sc} [V]	KT_e [eV]	KT_i [eV]	Depth [V]	Length [m]		Width [m]		Height [m]	
						Φ	n_i	Φ	n_i	Φ	n_i
1	0.20	35	2.0	2.0	-0.37	132	113	97	62	96	55
2	0.20	35	1.0	1.0	-0.39	143	151	84	65	78	57
3	0.20	35	2.0	1.0	-0.60	170	154	111	73	107	65
4	0.20	35	1.0	2.0	-0.23	81	105	62	54	58	49
5	0.40	20	2.0	2.0	-0.32	86	78	68	41	62	36
6	0.40	20	1.0	1.0	-0.35	97	103	57	43	53	39

TABLE II: Plasma parameters and results from six different simulations.(The lengths of the wakes shown in the table are underestimated, due to the use of artificial mass ratio (see Section III D.)

temperatures the satellite potential is shielded more efficiently, decreasing the size of the obstacle to the flowing ions. This effect can be seen when comparing the size of the ion wake in Simulations 1 and 4. The depths of the wake are relatively large for simulations 5 and 6, although the length, width and height for both the ion and potential wake are comparably small. This is due to the lower spacecraft potential, which will decay faster and thus has less compensating influence where the negative charge accumulation in the wake is strongest.

C. Boom simulations

For the simulations with only booms we present one specific run with the following plasma parameters: $n_0 = 0.20$ cm^{-3}, $KT_e = KT_i = 2.0$ eV, $E_k^i = 10$ eV. The grid size was $4 \times 4 \times 4$ m^3 and the number of grid-steps in each direction was $N_x = 60$, $N_y = 120$, $N_z = 60$. The boom was assumed to be in the $x-y$-plane at $z = 120$ m at an angle of $45°$ relative to the flow, which is in the y-direction. As PicUp3D includes no explicit provisions for modeling booms, we have instead fixed the potential of 17 discrete grid points, corresponding to a length of 90.5 m, close to the actual length of 88 m. Each grid point on the boom was set to the potential $+20$ V. (The electrical elements close to the probe described in Section III A are thus not represented.) To ensure the validity of a simulation where the booms are represented as discrete grid-points, the ion energy should be well below 20 eV, so that no ions can come close to the poorly resolved booms at potential 20 V. In our case, this is not a problem, since the flow energy is 10 eV and the maximum temperature 2 eV.

The ion density and the potential for this simulation are shown in Figure 3, where it can be seen that the booms indeed play an important role in the formation of an enhanced wake behind the spacecraft. The minimum potential in the wake is -0.80 V, which is substantially larger than for the simulation with spacecraft body (see Section III B) with the same plasma parameters.

Solving Poisson's equation on a grid with a spacing of 4 m will result in the potential close to the boom attaining larger values than expected from a wire boom at 20 V, due to the problem of resolving fine structures with a large grid. A few Debye lengths, and hence many grid steps, away from the boom, we may expect the distance dependence on the potential to be realistic, but close to the boom, the simulated potential will decay too slowly with distance. To compensate for this discrepancy, an effective boom potential was calculated by comparison with analytical models. At high potentials close to the boom, the Debye shielding has only small effects and the boom potential can be compared to the vacuum potential of a thin cylinder. The vacuum potential of a thin cylinder at a potential V can be approximated by[25]

$$\Phi(\tilde{x}, \tilde{y}, \tilde{z}) = \frac{V}{2 \ln \left(\frac{l}{a}\right)} \ln \left(\frac{d - \tilde{x} + r_1}{-d - \tilde{x} + r_2}\right), \qquad (4)$$

where l is the length of the cylinder, which is aligned with the $\tilde{x}$-axis and centered on the origin, a is its radius, $d = l/2$, $r_1 = \sqrt{(\tilde{x} - d)^2 + \tilde{y}^2 + \tilde{z}^2}$ and $r_2 = \sqrt{(\tilde{x} + d)^2 + \tilde{y}^2 + \tilde{z}^2}$. We now look for a value of V in this expression that results in a potential approximating the simulation result around 10 V and a few volts below, as this should be the most sensitive region for the dynamics of the ions whose drift energy is 10 eV. In Figure 4 the simulated potential (dashed blue line) is plotted together with the results of the analytical model for a thin boom ($a = 1.1$ mm) potential of 35 V (black line), as a function of radial distance from the midpoint of the boom. It can be seen that this indeed approximates the simulated potential field around and below 10 V, and we may thus assume that the potential of 20 V applied to the point cluster simulating the booms corresponds to an actual potential as high as 35 V for a real wire boom.

Further away from the boom, Equation (4) does not give the correct picture, because of the Debye shielding in the plasma. Therefore, at large distances from the boom, it is adequate to compare the simulated boom potential to that of a Debye-shielded infinite cylinder at potential V,

$$\Phi(r) = V \frac{K_0 \left(\frac{r\sqrt{2}}{\lambda_D}\right)}{K_0 \left(\frac{a\sqrt{2}}{\lambda_D}\right)}, \qquad (5)$$

FIG. 4: Comparison between the potential obtained from the simulation (dashed blue line) and analytical models. The red line corresponds to an infinite Debye-shielded cylinder and the black line to the model presented by $Hallén^{25}$. The horizontal axis gives the radial distance from the center of the boom in the boom-flow plane [r in Figure 7(b)].

and $2.7 \times 2.7 \times 1.35 \text{ m}^3$). In the first simulation the spacecraft is at 20 V. Using the concept of effective potential, we can expect this to correspond to a potential of $\sqrt[3]{4 \times 4 \times 4/(2.7 \times 2.7 \times 1.35)} \times 20\text{V} \approx 37$ V for a spacecraft with dimensions $2.7 \times 2.7 \times 1.35 \text{ m}^3$, assuming scaling of the potential as $1/r$. In the second simulation the spacecraft potential was set to 35 V. The two simulations give essentially the same potential pattern from a few meters outside the spacecraft, which confirms that the use of effective potentials is acceptable.

D. Accuracy of the simulations

Before comparing the simulation results to spacecraft data, the accuracy of the simulations should be discussed. In terms of basic modelling, two potentially important factors not included in the simulations are the magnetization of electrons (see Section III A) and the emission and exchange of photoelectrons by different electrical elements on the spacecraft. It is, for example, possible that the wake is filled to a large extent by photoelectrons emitted from the probes (as noted in Section III A photoelectrons from the spacecraft can never contribute much to the electron density due to the high spacecraft potential), rather than by natural plasma electrons. However, the photoelectron temperature is on the order of a few eV, close to the temperature of the ambient plasma electrons. Therefore, the charge in a wake filled with photoelectrons should not be very different from the resulting charge in the simulations.

Numerical problems that might influence the final results are the unphysical mass ratio, the Dirichlet boundary conditions and the modelling of the wire booms as discrete grid points.

FIG. 3: Averaged results from the boom simulation between $30 \, \omega_{\text{pe}}^{-1}$ and $60 \, \omega_{\text{pe}}^{-1}$. (The grid spacing is 4 m.) (a) Ion density in the $x-y$-plane through the boom. (b) Ion density in the $y-z$-plane through the boom. (c) Potential in the $x-y$-plane cutting the boom. The minimum value of the potential in the wake is -0.80 V. Equipotential contours are given at -0.7, -0.5, -0.3, -0.1, -0.01, 0.1, 1, 5, and 10 V.

where K_0 is a modified Bessel function of the second kind. The Debye-shielded potential is plotted in Figure 4 in red with $a = 1.1$ mm and $V = 35$ V. As expected, the simulated potential and the shielded cylinder approach each other far from the boom. Closer to the boom, the Debye shielding expression (5) breaks down due to violation of the assumption $e\Phi \ll KT_e$ inherent in the linear Debye shielding law. The influence of the wake on the potential can clearly be seen in the difference in the upstream and downstream directions in the simulation data.

To verify the validity of the effective potential we used two simulations with the spacecraft body for the same plasma parameters but different dimensions ($4 \times 4 \times 4 \text{ m}^3$

1. Mass ratio

Using an artificial mass ratio between ions and electrons in the PIC simulations, will not significantly influence the wake close to the spacecraft, since the wake potential is small relative to the spacecraft potential distribution. The orbit of a charged particle in any central field is determined completely by its kinetic energy per charge[26], in analogy with how the Keppler motion in a central gravitational field depends only on kinetic energy per mass, i.e. velocity squared. Deflection in such a potential is therefore accurately represented in a simulation where the kinetic energy is correctly represented, irrespective of the mass actually used. The potential around the spacecraft body can be well approximated as radially symmetric. For the potential around the finite booms, there is no perfect plane of symmetry, but at least for Debye lengths well below the boom length should radial symmetry be a good approximation in the central part of the boom.

We therefore expect the artificial mass ratio to have impact mainly on the filling-in of the wake at large distances from the spacecraft, where the space charge in the wake will dominate the potential, and only if the potential reaches values on the order of the ion temperature. The effect of the mass ratio has been examined by performing simulations 1 to 4 for the spacecraft body with both real $(m_i/m_e = 1836)$ and $(m_i/m_e = 100)$ mass ratios. The length of the wake is in average 45% longer for the real mass ratio. However, as expected, the wake structure close to the spacecraft is only marginally affected. This is evident when we examine the simulated signature of a double-probe instrument (see Section IV B). The dependence of wake length on mass ratio implies that, for equal flow energies, a wake in an oxygen-dominated plasma will be longer than in a hydrogen-dominated plasma. However, we should also note that at the same flow velocity oxygen ions are 16 times as energetic as protons, meaning that relation 1 often is not satisfied and thus do not contribute to the wake formation. In the high-altitude polar wind, where many enhanced wakes are observed, the plasma is dominated by protons[3].

2. Dirichlet conditions

The Dirichlet conditions of the PicUp3D code at the boundaries of the computational box (see Section III A) affect the potential close to the boundaries. In the presented simulations, the box was chosen to be sufficiently large to achieve a good overall picture. The potential deep inside the wake is then only marginally affected. As can be seen in Figures 2(b) and 3(a), the ion density is not significantly influenced by the Dirichlet conditions, due to the ion energy being high compared to the wake potentials. In a sense the ions just scatter off the vacuum field of the spacecraft or booms. To verify that the Dirichlet conditions do not constitute a significant error source, we have performed test simulations with 50% larger computational boxes showing that only the potential structures close to the boundaries are affected in the presented simulations.

3. Wire booms

Numerical modeling of 88 m wire booms with a radius of a few millimeters is a computational challenge. We have modeled the booms as a cluster of discrete grid points and compared the potential around the boom to results from analytical models to be able to estimate an *effective potential* for the boom. As described in the previous section, the validity of this effective potential was confirmed for the spacecraft body. For the booms, the method could be verified by comparison to adaptive-grid codes.

IV. COMPARISON TO DATA FROM THE CLUSTER SPACECRAFT

A. Cluster data

The Cluster mission is designed for four-point measurements in key regions of the terrestrial magnetosphere and its adjacent environment in the solar wind, in particular boundary layers such as the bow shock and the magnetopause[27]. Thanks to their polar orbits with perigee at 4 R_E and apogee at 19.6 R_E, the Cluster satellites sample a broad range of plasma regions, from the cold, dense plasmasphere to the hot, tenuous plasma sheet. The four spacecraft were designed with identical payloads, each carrying complete instrumentation for the study of particles and fields. For electric field measurements, Cluster includes two instruments using different techniques. The Electric Fields and Waves instrument (EFW) employs the well-known technique of measuring the voltage between spherical electrostatic probes at the ends of wire booms in the spacecraft spin plane[21]. The technique allows sampling at essentially unlimited frequencies, and can operate under widely varying plasma conditions, although great care is needed in the instrument design in order to minimize electrostatic disturbances from the spacecraft and the probe supports. EFW has two pairs of spherical probes (8 cm in diameter) separated by 88 m wire booms (2.2 mm diameter). In addition to the electric field, EFW provides a measurement of the spacecraft potential with respect to the ambient plasma, V_{sc}. The spin frequency of the satellites is 4 s.

The Electron Drift Instrument (EDI) uses a completely different technique[28], relying on observing the $\boldsymbol{E} \times \boldsymbol{B}$ drift of electron beams emitted from the spacecraft and returned by the ambient magnetic field, which thus has to be sufficiently strong for the method to work. Using electrons in the keV range, this technique is quite immune

to asymmetric electrostatic potentials on the order of a few volts arising close to the spacecraft.

We obtained evidence of the enhanced wake mechanism in Cluster data by studying the wake-induced field variations as a function of spacecraft potential. Figure 5 presents data studied in more detail by[4]. In the two upper panels it can be seen that the data from the EDI and the EFW instruments differ substantially when the spacecraft potential is high. The dependence on spacecraft potential is evident during periods when the artificial potential control instrument, ASPOC[29] is operating. By emitting a current, typically around 10 μA, of keV ions in a direction normal to the spin plane, ASPOC stabilizes the spacecraft potential at around 7 V. When ASPOC is not operating, V_{sc} reaches values up to +40 V in order to neutralize the photoelectron current emitted by the spacecraft. Figure 5 shows data from two of the Cluster satellites, spacecraft 1 (henceforth denoted SC1) in the top two panels and SC3 in the lower two. At the time in question, Cluster was above the northern polar cap at (-2.5, 1.4, 4.9) R_E in GSE coordinates (GSE X points towards the Sun and GSE Z towards the ecliptic north pole). On SC3 ASPOC was activated at around 04:25, resulting in the immediate and clearly visible stabilization of V_{sc}. In the SC1 data, EFW and EDI are seen to differ by up to 10 mV/m from 04:20. Only E_X is shown, as almost all the wake-induced field was found in this component in this case. The same EDI-EFW discrepancy was seen initially in the SC3 data, but when ASPOC was activated, the difference was greatly diminished. This is exactly the behavior we would expect from a wake created by the spacecraft potential distribution, as discussed above: i.e. when V_{sc} decreases, so does the size of the wake and, hence, the perturbation it causes to the potential field around the spacecraft. The clear relation between the natural variations in spacecraft potential and the wake-induced field that can be seen in the SC1 data indicates that V_{sc} is the controlling parameter, regardless of whether it is regulated by the plasma environment or by ASPOC.

Since the ions emitted by ASPOC are highly energetic, they will travel far from the spacecraft, and the asymmetries introduced in the sheath around the spacecraft because of the ion beam do not substantially affect the EFW measurements. A complete analysis of the effects on EFW due to the operation of ASPOC is beyond the scope of this paper, but we point out that the effects other than the stabilization of the spacecraft potential are relatively small. ASPOC is therefore quite different from the PSI (Plasma Source Instrument) on the POLAR satellite, which creates a cloud of cold plasma around the spacecraft and has been reported to introduce spurious signals in electric field measurements[30,31].

From the theoretical estimates of the size of the wake potential in Section II, we can obtain an upper limit for the magnitude of the effect on the EFW double-probe instrument. Assuming that the potential in the wake is maximal (i.e. on the order of KT_e) and that one probe
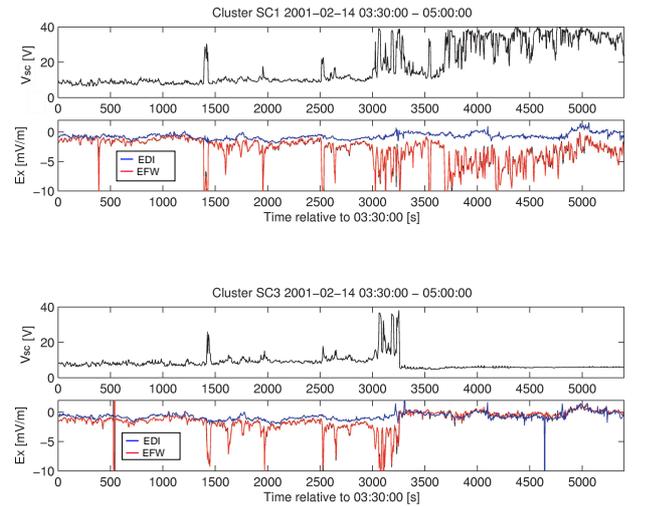
FIG. 5: EFW and EDI electric field data from SC1 (top two panels) and SC3 (lower two). For each spacecraft, the top panel shows the spacecraft potential V_{sc}, while the lower panel displays the EDI (dashed line) and EFW (solid line) estimates of the sunward component of the electric field. The difference between the two electric field instruments increases when V_{sc} is high. The jump in V_{sc} for SC3 at 04:25 is due to the activation of ASPOC. Large discrepancies between the EDI and EFW electric field estimates can be seen from around 04:20. For SC1, they continue throughout the interval, while they almost disappear from the SC3 data when ASPOC is activated.

experiences the full wake potential and the other nothing, there would be a wake-induced electric field signal in the double-probe instrument of the order of $KT_e/(2le)$, where $2l$ is the separation between the two probes, i.e. 88 m for EFW. In the polar wind, with KT_e values on the order of a few eV, we find that wake-induced fields up to a few tens of mV/m could indeed be possible, which is actually observed. To obtain more precise estimates of the wake effect on the double-probe instrument, we use the results from the two types of simulations.

B. Comparison to spacecraft body simulations

First, we examined the effect of the spacecraft body. To obtain an estimate of the influence of the wake on the double-probe instrument we considered the potential difference between two points on opposite sides of the spacecraft separated by the boom length of 88 m. An advantage of only considering the wake effect of the spacecraft body, is that we do not have to fix the angle of the booms relative to the flow. We can therefore plot the potential difference between the probes as a function of the angle of the virtual booms relative to the flow. Figure 6(a) shows such plots for the four first simulations in Table II together with EFW data from one spin.

As expected, the plot in Figure 6(a) is periodic with
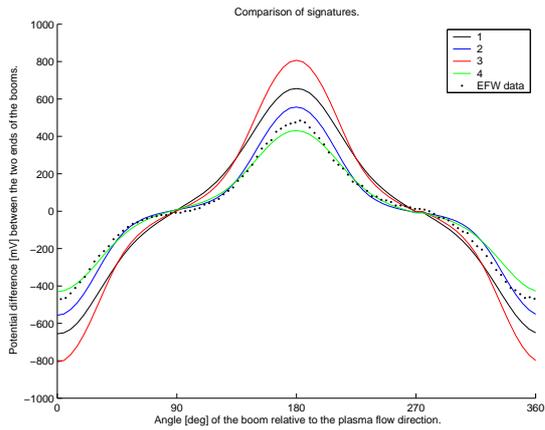
(a)
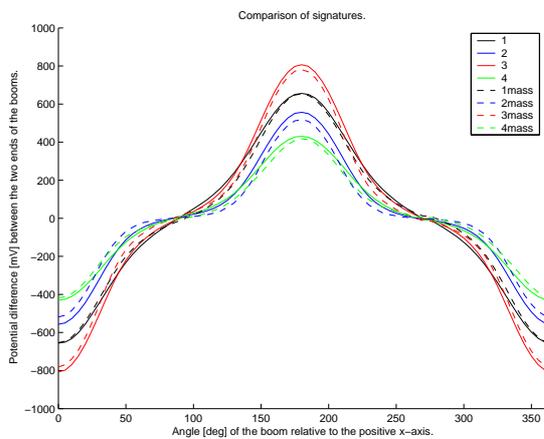
(b)

FIG. 6: (a) [Color] Potential difference between the probes at different angles of the boom relative to the flow for the four first simulations (solid lines) together with electric field measurements (dotted lines) from the pair of probes 34 of the EFW instrument on SC3 during one spin period (4 s) at 2002-02-13 01:48:06-10. (b) [Color] Simulations 1-4 with real (dashed lines) and unphysical (solid lines) mass ratio. The signatures are only marginally effected by the unphysical mass ratio.

maximum differences at 0° and 180° relative to the flow, and minimum differences at 90° and 270°. It can be seen that the agreement between the EFW data and the results from simulations is good in this case. Comparison between the simulation and data plots provides clarification of the previously unexplained signature in the satellite data. From the simulation it can be seen that an inflection point arises when the probes change the roles of being the closest or furthest away from the wake. The magnitude of the potential difference is also consistent with Cluster measurements in tenuous plasmas, where

spurious electric fields on the order of $5-10 \, \mathrm{mV/m}$ can be detected[4]. The shape of the signatures from the double-probe instrument is dependent on the plasma parameters. Thus, the wake field signatures could possibly be used to derive the properties of the plasma. Figure 6(b) shows the signature from a double-probe instrument for simulations with both real and unphysical mass ratios. It can clearly be seen that the double-probe instrument signature is only marginally affected by the choice of mass ratio, as expected (see Section III D).

C. Comparison to boom simulations

As for the spacecraft, we will now use the boom simulations to quantify the effect of the boom wake field on the double-probe electric field instrument. In Figure 7(a), the difference in potential between two probes at the same distance from the opposite ends of the wire boom is plotted as a function of the distance from the boom ends. The maximum potential difference is approximately 520 mV. As expected, the difference is zero far away from the booms, where there is an unperturbed plasma, and also at the boom tips, which are at satellite potential. As mentioned in Section III A, the Cluster EFW probes are 3 m outside the part of the wire booms that are at spacecraft potential. One grid spacing distance (4 m) away from the boom on each side, which is close to the relevant 3 m, the observed potential difference is 460 mV. Dividing this by 90.5 m, we find that EFW could be expected to show an apparent electric field of 5 mV/m due to the boom wake. However, since the virtual probes in this case are so close to the boom potential, they will be affected by the boom potential, and the 5 mV/m should be regarded as an order of magnitude estimate of the apparent electric field. Another limitation of the boom simulation in comparison to the setup of the Cluster satellites, is that we have only modeled one of the boom pairs. The wake effect should be even greater with two crossed booms. Comparing the resulting potential difference from the boom simulation to the spacecraft body simulation at 45° with the same plasma parameters (Simulation 1), we see that the 460 mV from the boom simulation is substantially larger than from the spacecraft body, which results in a potential difference of 250 mV.

From comparing the potential patterns in Figures 2(b) and 3(c), we can immediately see that the dominating source for the potential at the probes is the booms, not the spacecraft body. Also, the wake is much larger in the boom simulation than in the spacecraft simulation. When the spacecraft and booms spin, the wake and its associated potential should change, and hence also the wake signal detected by a double-probe instrument. So can it be reasonable to assume that the spin signature for a double probe instrument, derived from the simulation without booms and shown in Figure 6, should represent reality?
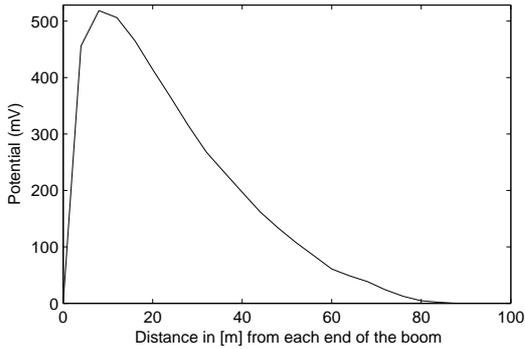
(a)
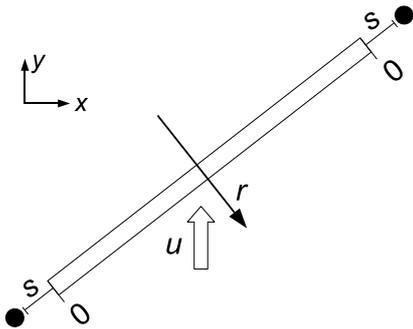
(b)

FIG. 7: (a) Difference in potential between the ends of the boom inferred from the simulation with booms only. The maximum potential difference is 520 mV. (b) Schematic picture of the boom explaining the horizontal axis of (a): s is the distance from the boom end to the probe. (The coordinate r is the radial distance from the midpoint of the boom used in Figure 4.)

If we first consider the question of spin variation of the wake itself, we can note that this could be a problem mainly if the flow direction is in the spin plane, so that the obstacle, i.e. the $\Phi = \frac{1}{2} m_i u^2 / e$ equipotential, as seen from the direction of the approaching ions would vary significantly in size and shape: small and circular when the boom is aligned to the flow, much elongated when the angle of attack is oblique. However, as the real Cluster spacecraft have two orthogonal pairs of wire booms, the obstacle seen by the approaching ions will always be elongated, regardless of spin phase. We therefore do not expect the non-variation of the wake with spin phase to be a significant error source in the spacecraft body simulations.

But could not the shape of the spin signature presented in Figure 6 be influenced by the local potential close to the probe, which is certainly drastically changed when the booms are included? Close to the booms, the charge

density is low, and the potential is mainly the vacuum potential, which is symmetric between the two probes and hence does not affect the voltage measured between them. Significant charge densities, distributed over regions of size on the order of λ_D so that they can give rise to any appreciable potentials, are found mainly in the wake, as is easily seen in Figures 2(b) and 3(c). The "distant" source of the wake is therefore the more important for the potential difference detected at the probes. As the presence of this source, albeit not its magnitude, is similar in the boom and spacecraft body simulations, we expect the shape of the spin variation shown in Figure 6 to be approximately the same also in the case of booms only. Nevertheless, this remains a point that should be clarified in future simulations (see Section V).

As for the magnitude of the wake effect, this is clearly larger for the boom simulations than for the case of the spacecraft body. This is clear from the minimum potentials observed in Figures 2(b) and 3(c) as well as from the comparison of the values at 45° that we discussed above. It is thus reasonable to expect the spacecraft body simulations to underestimate the magnitude of the wake effect on double-probe measurements. The good agreement between simulated and observed spin signatures in Figure 6(a) should then imply that some of the input parameters for the simulation do not reflect the real situation. The most likely error source would be an overestimate of the electron temperature T_e, for which we lack any experimental data and have only assumed a value on the order of T_i. Other parameters (n_e, T_i, v_i, V_{sc}) all have error sources associated, but their values are much better founded on measurements either from Cluster[22] or other spacecraft in the same region[3].

V. CONCLUSIONS

We have studied the wake formation behind positively charged spacecraft in cold, flowing, tenuous plasmas. Theoretical estimates together with simulations have given new information on the size of the wake. Data from the electric field instruments on board the Cluster spacecraft have provided experimental evidence of the wake formation in cold, flowing, tenuous plasmas. The wake will be enhanced in these regions, which is explained by the fact that $KT_i < m_i u^2 < eV_{sc}$. It was indeed found that the satellite potential, V_{sc}, controls the size of the wake, which is especially evident when the potential is reduced by the ASPOC instrument. More detailed analysis of the experimental data has been given by *Eriksson et al.*[4]. A simulation of the wake field detected by the Cluster electric field instrument EFW resulted in $5 - 10$ mV/m, which is close to observed magnitudes, and the variation on spacecraft spin was well represented. This was obtained from simulations of the spacecraft body and the booms separately. The combined effect of both should be somewhat higher.

In future work, an adaptive-grid code with the ability

to resolve finer structures, such as wire booms, should be used. Such a code would also allow to simulate any angle between the flow and the booms, making it possible to obtain more reliable spin signatures. It would also be rewarding to model a more realistic spacecraft geometry with both body and booms, including important electric elements close to the probes. The code should not be implemented only with Dirichlet conditions, but with more flexible boundary conditions. For this kind of problem, Neumann conditions on all sides except the inflowing boundary are better suited. An example of such a code is presented by *Roussel et al.*[32]. In spite of these desirable improvements, the present study has shown that a simple and open source simulation code package can be run on a common desktop PC to give quantitative results for this kind of spacecraft–plasma interaction problems. The main conclusions that can be drawn from this work are as follows.

1. The qualitative hypothesis of an electrostatic wake with dimensions determined by the spacecraft potential field forming in situations with $KT_i < m_i u^2 < eV_{sc}$ was quantitatively verified by simulations.

2. Both the spacecraft body and the wire booms create large enhanced wakes in these situations. The effective size of the wire booms transverse to the flow can be increased from millimeters to meters.

3. The size of the wake scales with the plasma parameters, of which the two most important features are:

    (a) low ion temperature causes larger ion wake, and

    (b) high electron temperature leads to more negative potential in the wake.

4. The signatures from the electric field data agree well with the simulations, and their shape and magnitude depends on plasma parameters. It is therefore in principle possible to derive plasma parameters from wake observations in electric field data. The first application of this has been presented by *Engwall et al.*[22]

[1] A. W. Yau and M. André, Space Sci. Rev. 80, 1 (1997).

[2] T. E. Moore, C. R. Chappell, M. O. Chandler, P. D. Craven, B. L. Giles, C. J. Pollock, J. L. Burch, D. T. Young, J. H. Waite Jr., J. E. Nordholt, M. F. Thomsen, D. J. McComas, J. J. Berthelier, W. S. Williamson, R. Robson, and F. S. Mozer, *Science* 277, 349 (1997).

[3] Y.-J. Su, J. L. Horwitz, T. E. Moore, B. L. Giles, M. O. Chandler, P. D. Craven, M. Hirahara, and C. J. Pollock, J. Geophys. Res. 103, 29 305 (1998).

[4] A. Eriksson, M. André, B. Klecker, H. Laakso, P.-A. Lindqvist, F. Mozer, G. Paschmann, A. Pedersen, J. Quinn, R. Torbert, K. Torkar, and H. Vaith, Ann. Geophys. (in press), (2006).

[5] Y. L. Al'pert, A. V. Gurevich, and L. P. Pitaevskii, Space Physics with Artificial Satellites (Consultants Bureau, New York, 1965).

[6] D. E. Hastings, J. Geophys. Res. 100, 14 457 (1995).

[7] A. Pedersen, P. Décréau, P. Escoubet, G. Gustafsson, H. Laakso, P.-A. Lindqvist, B. Lybekk, F. Mozer, and A. Vaivads, Ann. Geophys. 19, 1483 (2001).

[8] L. Kraus and K. W. Watson, Phys. Fluids 1, 480 (1958).

[9] S. Rand, Phys. Fluids 3, 588 (1960).

[10] S. D. Hester and A. A. Sonin, Phys. Fluids 13, 641 (1960).

[11] N. Singh and V. S. Chagani, J. Geophys. Res. 102, 195 (1997).

[12] L. Zinin, S. Grigoriev, and I. Rylina, Auroral phenomena and solar-terrestrial relations: Proceedings of the conference in memory of Yuri Galperin, 2004, edited by M. L.M.Zelenyi and J.H.Allen, Eds. CAWSES Handbook-001, 2004, pp. 76–83.

[13] J.-F. Roussel and J.-J. Berthelier, J. Geophys. Res. 109, A01104 (2004).

[14] O. H. Bauer, R. Grard, G. Haerendel, and A. Pedersen, "Influence of wake and photoemission on electric field measurements with a double probe on GEOS-2," in *Spacecraft/Plasma Interactions and their Influence on Field and Particle Measurements*, ser. ESA SP-198, 1983, pp. 51–56.

[15] A. Pedersen, C. A. Cattell, C.-G. Fälthammar, V. Formisano, P.-A. Lindqvist, F. Mozer, and R. Torbert, Space Sci. Rev. 37, 269 (1984).

[16] E. Engwall, A. Eriksson, A. Pedersen, J. Forest, G. Paschmann, J. Quinn, R. Torbert, and K. Torkar, "Wake effects on positively charged spacecraft in flowing tenuous plasmas: Cluster observations and modeling," in *Proceedings of the 8th Spacecraft Charging Technology Conference*, Huntsville, Alabama, 2003.

[17] E. Engwall and A. I. Eriksson, "Cold magnetospheric plasma flows and spacecraft wakes: PicUp3D simulations and Cluster data," in *Proceedings of the 9th Spacecraft Charging Technology Conference*, Tsukuba, Japan, 2005.

[18] E. Engwall, "Numerical studies of spacecraft-plasma interaction: Simulations of wake effects on the Cluster electric field instruments EFW," Swedish Institute of Space Physics," IRF Scientific Report 284, 2004, http://www.irf.se/Publications/.

[19] J. Forest, L. Eliasson, and A. Hilgers, "A new spacecraft plasma simulation software, PicUp3D/SPIS," in *7th Spacecraft Charging Technology Conference*, vol. SP-476. ESA, 2001, pp. 515–520.

[20] C. K. Birdsall and A. B. Langdon, Plasma Physics via Computer Simulations (Adam Hilger, Bristol, 1991).

[21] A. Pedersen, F. Mozer, and G. Gustafsson, "Electric field measurements in a tenuous plasma with spherical double probes," in *Measurement Techniques in Space Plasmas: Fields*, ser. Geophysical Monograph 103. American Geophysical Union, 1998, pp. 1–12.

[22] E. Engwall, A. I. Eriksson, M. André, I. Dandouras, G. Paschmann, J. Quinn, and K. Torkar, Geophys. Res.

Lett. (accepted), (2006).

[23] A. Pedersen, Ann. Geophys. 13, 118 (1995).

[24] R. D. Sydora, "Low noise electromagnetic δf particle-in-cell plasma simulation model and applications," in *Space plasma simulation: proceedings of the Sixth International School/Symposium*, 2001.

[25] E. Hallén, Electromagnetic Theory, (Chapman & Hall, London, 1962).

[26] L. D. Landau and E. M. Lifshitz, Course of Theoretical Physics, vol. 1: Mechanics, 3rd ed. (Pergamon Press, New York, 1976).

[27] C. P. Escoubet, M. Fehringer, and M. Goldstein, Ann. Geophys. 19, 1197 (2001).

[28] G. Paschmann, C. E. McLlwain, J. M. Quinn, R. B. Torbert, and E. C. Whipple, "The Electron Drift Technique for Measuring Electric and Magnetic Fields," in *Measurement Techniques in Space Plasmas: Fields*, ser. Geophysical Monograph 103. American Geophysical Union, 1998, pp. 29–38.

[29] K. Torkar, W. Riedler, C. P. Escoubet, M. Fehringer, R. Schmidt, R. J. L. Grard, H. Arends, F. Rüdenauer, W. Steiger, B. T. Narheim, K. Svenes, R. Torbert, M. André, A. Fazakerley, R. Goldstein, R. C. Olsen, A. Pedersen, E. Whipple, and H. Zhao, Ann. Geophys. 19, 1289 (2001).

[30] R. H. Comfort, T. E. Moore, P. D. Craven, C. J. Pollock, F. S. Mozer, and W. T. Williamson, J. Spacecraft and Rockets 35, 845 (1998).

[31] N. Singh, W. C. Leung, T. E. Moore, and P. D. Craven, J. Geophys. Res. 106(A9), 19179 (2001).

[32] J.-F. Roussel, F. Rogier, D. Volpert, J. Forest, G. Rousseau, and A. Hilgers, "Spacecraft plasma interaction software (SPIS): Numerical solvers methods and architecture," in *Proceedings of the 9th Spacecraft Charging Technology Conference*, Tsukuba, Japan, 2005.

Paper II
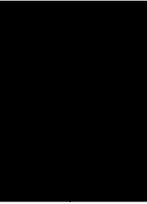
Double-probe measurements in cold tenuous space plasma flows

Erik Engwall
Department of Astronomy and Space Physics,
Uppsala University, Sweden

Anders I. Eriksson
Swedish Institute of Space Physics,
Uppsala, Sweden

Abstract— **Cold flowing tenuous plasmas are common in the terrestrial magnetosphere, particularly in the polar cap and tail lobe regions, which are filled by the supersonic plasma flow known as the polar wind. Electric field measurements with double-probe instruments in these regions suffer mainly from two error sources: 1. An apparent sunward electric field due to photoemission asymmetries in the probe-boom system. 2. An enhanced negatively charged wake forming behind the spacecraft, which will affect the probe measurements. We investigate these effects experimentally by Fourier analysis of the spin signature from the double-probe instrument EFW on the Cluster spacecraft. We show that while the signature due to photoemission asymmetry is very close to sinusoidal, the wake effect is characterised by a spectrum of spin harmonics. The Fourier decomposition can therefore be used for identifying wake effects in the data. As a spin-off, the analysis has also given information on the cold flowing ion population.**

I. INTRODUCTION

Electric field measurements are essential for the understanding of numerous processes in space plasmas. Instruments for measurement of the electric field, from DC up to kHz or even MHz frequencies, are thus carried on all satellite missions attempting to resolve space plasma dynamics. One of the most implemented techniques for measuring the electric field is by the use of double-probes, which has been used on e.g. GEOS-1 and ISEE-1 [1], Viking [2], Freja [3], Geotail [4], POLAR [5] and FAST [6]. Useful reviews of the double-probe technique are given by Pedersen et al. [7] and Maynard [8].

The most recent mission equipped with double probes is Cluster, where the Electric Fields and Waves (EFW) instrument measures the electric field by use of spherical probes at the ends of 42.5 m wire booms (probe-to-probe separation: 88 m) extended in a plane close to the ecliptic by the spacecraft spinning at a period of 4 s [7], [9]. EFW can sometimes reach an accuracy level of a fraction of one mV/m, as determined from comparisons to measurements by other techniques [10]. However, to reach such accuracies, it is necessary to have a quantitative understanding of various error sources to the same magnitude. A well known error source [7] is an apparent sunward electric field, caused by the inevitably asymmetric photoemission

currents flowing between the probes and their adjacent elements on the spacecraft. Only on spacecraft with sun-pointing spin axis can this effect be avoided.

Another error source is spacecraft wakes, which may form behind positively charged spacecraft in a tenuous plasma where the plasma flow speed relative to the spacecraft exceeds the ion thermal speed and ion acoustic speed, i.e. for supersonic ion flows. Supersonic ion flow around a spacecraft is very common, for example, due to high plasma flow speed in the solar wind, or due to fast spacecraft motion in the ionosphere. The electrons have a much higher thermal speed than the ions, so the electron flow around the spacecraft is always subsonic, resulting in electrons entering the ion wake behind the spacecraft due to random thermal motion, charging the wake negatively.

By comparing double-probe data from EFW to electric field data obtained with the other electric field instrument on Cluster, the Electron Drift Instrument (EDI) [11], it is possible to investigate this process in detail. EDI emits keV electrons into the plasma and detects them when returned to the satellite by the geomagnetic field, allowing the determination of the electric field from their drift. Through combination of results from the two instruments we will here derive detailed information on the wake electric field.

The electrostatic potential attained by the spacecraft plays an important role for measurement errors. Photoemission from a sunlit spacecraft in the tenuous plasmas of the outer magnetosphere normally brings the spacecraft potential to positive values of the order of tens of volts. This positive spacecraft potential can be expected to affect the flow of photoelectron currents around the spacecraft, and hence the apparent sunward electric field. In the supersonically flowing tenuous plasmas where spacecraft wakes form, local electric fields also depend on the spacecraft potential, as it regulates the size and charge of the wake [10], [12].

To fully exploit the possibilities of double-probe measurements it is important to have a detailed understanding of these error sources. This can be attained by computer simulations [12], [13], which we will show some examples of here, and by detailed experimental investigation, which is our prime aim in this paper. In particular, we show how

the errors may be identified by the Fourier decomposition of the observed spin signature.

In this paper we examine the apparent sunward field due to asymmetric photoemission and the wake field with the ambition to be able to identify and remove spurious fields from EFW data. We also retrieve information about the cold plasma flow from the wake field.

II. SPACECRAFT WAKE AFFECTING DOUBLE-PROBE INSTRUMENT

A. Evidence of wake in Cluster data

When operating in cold flowing plasmas, a direct interpretation of EFW data gives an electric field estimate differing from what is observed by EDI. An example from the polar wind is shown in Figure 1. In this Figure it can also clearly be seen that the problems grow when the spacecraft potential is high.

The explanation to the difference between the instruments is that an enhanced wake is formed behind the spacecraft [10]. This wake will be much larger than expected from the geometrical size of the spacecraft, if the flow energy of the ions, E_k^i, not only exceeds the ion thermal energy, but also is lower than the spacecraft potential, i.e. if the following inequality is satisfied

$$KT_i < E_k^i < eV_s, \tag{1}$$

where KT_i and V_s are the ion thermal energy and the spacecraft potential, respectively. For such conditions, the ions will be deflected by the potential structures rather than the geometrical shape of the spacecraft. In addition, not only the spacecraft body will contribute to the wake, but also the thin wire booms, since their effective size will grow from a few millimeters to the order of meters.

As the keV electrons emitted by EDI have a gyroradii much larger than the typical dimensions of any spacecraft wake size, and are only very weakly affected by the relatively small electrostatic potentials forming around the spacecraft, the electric field estimate from EDI is unaffected by the wake. On the other hand, the EFW probes, reaching only 44 m from the centre of the spacecraft, will often clearly pick up the wake signature.

B. Simulations of the wake

To study the wake formation behind Cluster and the effect on EFW, we have performed simulations with the code package PicUp3D [14]. The simulations may also provide some information on the dependence of the wake properties on plasma parameters such as ion temperature, which is useful since the cold ions are difficult to measure in situ with conventional ion detectors. We have run two types of simulations for typical polar wind conditions modelling the ions as protons (E_k^i=10 eV, KT_i=1-2 eV,

KT_e=1-2 eV, n_0=0.2 cm^{-3}, V_s=35 V.): The wake effect behind a) one pair of the wire booms only, and b) the spacecraft body only. This division is made to simplify the simulations, but also to better understand the contributions to the wake from different parts of the spacecraft system. The simulations with the booms have indeed shown that they can by themselves create a wake giving rise to a spurious electric field of over 5 mV/m, assuming the probes perfectly couple to the plasma [12]. This is comparable to the spurious electric field in EFW data of 5-10 mV/m.

In Figure 2(a) the ion density from one of the simulations with the spacecraft only is displayed, showing a clear depletion behind the spacecraft. This ion wake will to a large extent be filled with electrons, whose thermal speed greatly exceeds the flow speed, and a negatively charged wake is created behind the spacecraft, which can be seen in Figure 2(b), where the potential contours around the spacecraft are shown. The effect on the double-probe instrument mounted on a spinning spacecraft for different plasma parameters is shown in Figure 3, which indeed show the same overall shape as EFW data. From the simulations, it is evident that the size of the wake, as well as the signatures are dependent on the plasma parameters. (For more details on the simulations and the dependence of wake properties on different parameters, see *Engwall et al.* [12].) Thus, by careful examination of the signatures of the spurious EFW signal in combination with the simulation results, there is a potential to derive properties of the flowing plasma. By another method, it is possible to calculate the flow velocity only from comparison between EFW and EDI data, provided that certain conditions apply [15]. In section III-B we show that it is possible to determine the angle of the flowing plasma in the spin plane, and also the shape and depth of the wake by examination of the spin signature of the electric field data only. From the sounding experiment WHISPER on Cluster [16], as well as from measurements of the spacecraft potential, the plasma density can be estimated. The remaining two free parameters, the electron and ion temperatures, could possibly be obtained by careful examination of the signatures of the spurious EFW signal in comparison with the simulation results, assuming that the plasma flow consists of protons.

Eventhough protons consitute the dominant ion species in the polar wind, the O$^+$ content can be relatively high during magnetically active times. A flow rich in O$^+$ will certainly create another type of wake, since the O$^+$ ions are higher in energy than the protons [17]. This higher energy will give rise to a more narrow wake, and the signatures from the double-probe instrument should thus be affected. In principle, the signatures could therefore also tell something about the ratio of ion species in the cold plasma flow. However, it might be difficult to distinguish variations due to ion content from variations related to other plasma properties, such as proton and electron temperatures.

Cluster SC1 2001–02–14
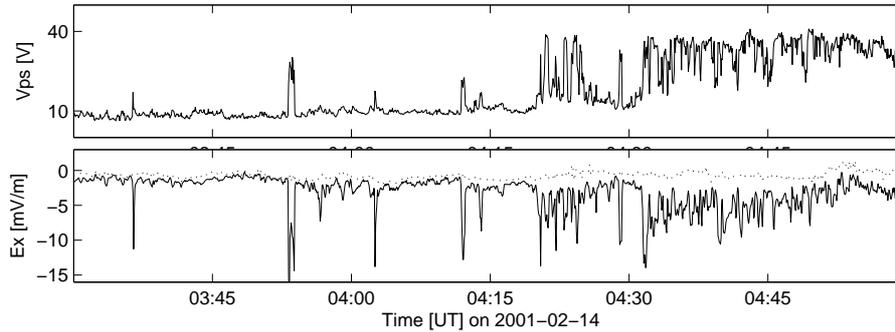
Fig. 1. EFW and EDI electric field data from Cluster 1. The top panel shows the spacecraft potential V_s, while the lower panel displays the EDI (dashed line) and EFW (solid line) estimates of the GSE X component of the electric field. Strong discrepancies between the EDI and EFW electric field estimates can be seen when V_s is high. At the time of observation Cluster was above the northern polar cap at (-2.5, 1.4, 4.9) R_E in GSE coordinates.

III. ANALYSIS OF DOUBLE-PROBE DATA

A. Sunward offset field

Since the Cluster spacecraft are spinning, the voltage difference between two oppositely mounted probes varies sinusoidally in time if there is a constant and homogeneous electric field and the instrument is ideal. However, the measured field will be smaller by a certain factor than the real ambient field, since the long booms of the double-probe instruments always to a certain extent "short circuit" the electric field in the plasma. In the data analysis below, we have chosen this factor to be 0.75.

At first, we study the apparent sunward electric field due to asymmetric photoemission, E_a. To study this effect, we choose an interval where EDI and EFW agrees on GSE E_Y, and the E_X component is small in EDI data. By Fourier analysis of the double-probe signal together with EDI data from the same period, we can understand the nature of the sunward photofield. Expressing the effect of the photofield on EFW in its most general Fourier decomposition, the effect of the total field on EFW is

$$E_{\text{tot}}(\theta) = E_x \cos\theta - E_y \sin\theta + $$
$$+ \sum_{n=1}^{\infty} (a_n^{\text{ph}} \cos(n\theta) + b_n^{\text{ph}} \sin(n\theta)) \quad (2)$$

where E_x and E_y are the electric field components given by EDI and θ is the spin angle to the boom from the positive X_{GSE} axis (the negative sign in front of E_y arises from the fact that the satellite is spinning clockwise, see Figure 6). Figure 4 shows the Fourier decomposition of one specific spin (panel (a)), the Fourier coefficients from the photofield, a_n^{ph} and b_n^{ph}, (panel (b)) and the different components of the signature (panel (c)). This example together with numerous other have shown that the photofield has the following properties:

1) The even coefficients in the Fourier expansion are negligible, as is to be expected for a differential signal.
2) The fundamental frequency is constituted almost only by $\cos\theta$ (b_1 very small, i.e. the spurious field is in the sunward-antisunward direction, as expected).
3) The odd coefficients are vanishingly small for $n > 1$.

This means that the apparent photoasymmetry signal to a very good approximation can be written as $E_a(\theta) = a_1^{\text{ph}} \cos\theta = E_a^0 \cos\theta$.

As can be seen in Figure 5, the photofield is dependent on the spacecraft potential. For this event, the photofield seems to increase with increasing satellite potential. It would be rewarding to establish an empirical relation between the photofield and the spacecraft potential to be able to routinely remove the expected photofield from EFW data. This requires a more extensive data study. It may be noted that the typical photofield value for Cluster EFW is around 1 mV/m, which is very small compared to some earlier instruments with less degree of symmetry. For instance, the typical value on GEOS was 8 mV/m [18].

B. Wake field

Knowing the photoasymmetry induced field, we can also derive properties of the wake, such as direction, depth and shape. We now assume that the impact of the wake field on EFW can be written as

$$E_w = a_{w1} \cos\theta_b + a_{w3} \cos(3\theta_b) + a_{w5} \cos(5\theta_b), \quad (3)$$

where θ_b is the angle between the boom and the direction of the wake flow in the spin plane (see Figure 6). There are only contributions from cosine, since the electric field is symmetrical along the direction of the wake. In our model, we assume no time varying fields during the spin, so that

(a)

(b)
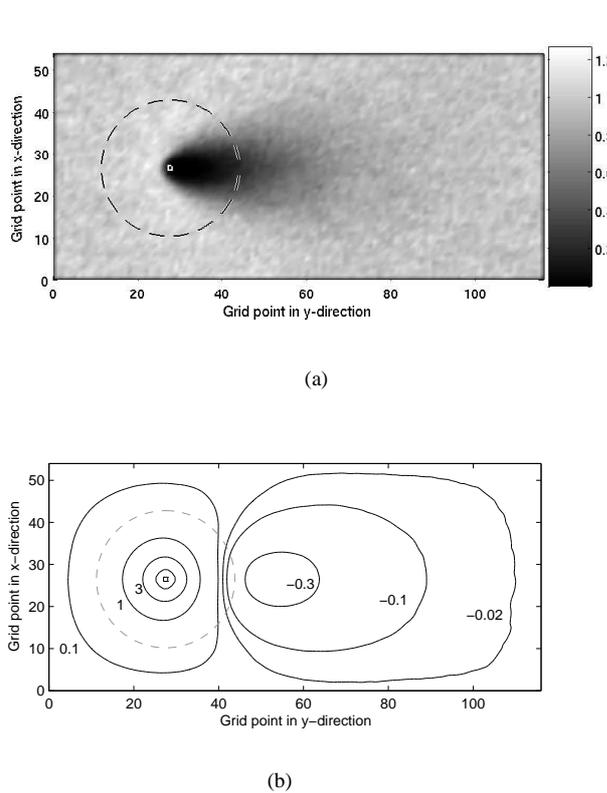
Fig. 2. Ion density and potential around the spacecraft. The dashed circles show the location of the Cluster EFW probes throughout a spin period. (The grid spacing is 2.7 m.) (a) Ion density in the $x - y$-plane through the spacecraft. (The white square shows the location of the spacecraft.) (b) Potential in the $x - y$-plane through the spacecraft, the potential of which is 35 V. The minimum value of the potential in the wake is -0.34 V. Equipotential contours are given at -0.3, -0.1, -0.01, 0.1, 1, 3, 10 and 35 V.

when equating the potential difference all even Fourier components vanish. We also neglect all terms higher than fifth, which should be accurate for wide wakes (such as in Figure 2(a)). Narrow wakes occur for example in the solar wind, but do not normally constitute a large problem since they are easily detectable in EFW data.

Introducing $\theta_{\rm w}$ as the angle between the positive $X_{\rm GSE}$ direction and the wake, the total electric field signature can be expressed as

$$
\begin{aligned}
E_{\rm tot}(\theta) = {} & (E_x + E_{\rm a}^0 + a_{\rm w1} \cos \theta_{\rm w}) \cos \theta + \\
& + (-E_y + a_{\rm w1} \sin \theta_{\rm w}) \sin \theta + \\
& + a_{\rm w3} \cos(3\theta_{\rm w}) \cos(3\theta) + a_{\rm w3} \sin(3\theta_{\rm w}) \sin(3\theta) + \\
& + a_{\rm w5} \cos(5\theta_{\rm w}) \cos(5\theta) + a_{\rm w5} \sin(5\theta_{\rm w}) \sin(5\theta).
\end{aligned}
\tag{4}
$$

From a Fourier analysis of EFW spin data, we can now retrieve the direction of the wake in the spin plane, $\theta_{\rm w}$, the wake Fourier components, $a_{\rm w1}$, $a_{\rm w3}$ and $a_{\rm w5}$, which describes the depth and shape of the wake, and the ampli-
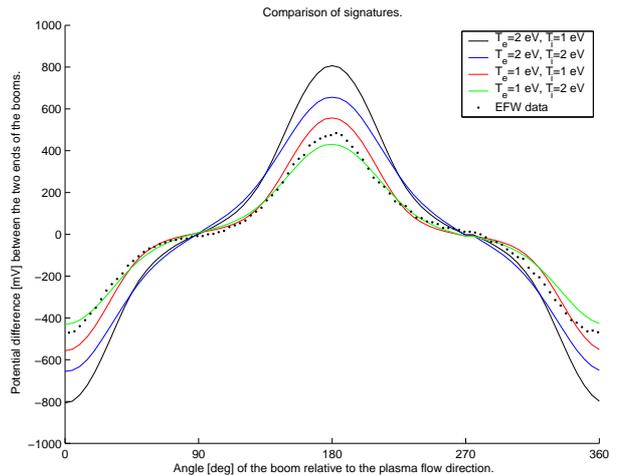
Fig. 3. Comparison of signatures from EFW data with four simulations with the spacecraft. The signatures show the potential difference between the probes at different angles of the boom relative to the flow. The EFW data is taken from the difference between the opposite probes 3 and 4 (probe pair 34) of the EFW instrument on Cluster 3 during one spin period (4 s) starting at 2002-02-13 01:48:06. In the simulations the spacecraft potential and density are constant, V_s=35 V and n_0=0.2 cm^{-3}, while the temperatures are varied: 1. $KT_e = 2$ eV, $KT_i = 1$ eV. 2. $KT_e = KT_i = 2$ eV. 3. $KT_e = KT_i = 1$ eV. 4. $KT_e = 1$ eV, $KT_i = 2$ eV. The amplitude of the spurious electric field varies from 4-10 mV/m.

tude of the photoelectron field, $E_{\rm a}^0$. We make the Fourier analysis of one spin at a time. As the EFW data gives six Fourier components, but only five variables, the system of equations is overdetermined. We choose to derive $\theta_{\rm w}$ both from the third and fifth Fourier components, since it is not uniquely determined: $\theta_{\rm w3}$ can take 6 different values ($\theta_{\rm w3} = \frac{1}{3} \arctan(b_3/a_3) + \frac{n\pi}{3}$) and $\theta_{\rm w5}$ 10 different values ($\theta_{\rm w5} = \frac{1}{5} \arctan(b_5/a_5) + \frac{n\pi}{5}$). The correct angle is found by minimising the difference between $\theta_{\rm w3}$ and $\theta_{\rm w5}$. A small difference indicates that we have found the right angle and also confirms the validity of our model of the wake stated in equation (3). Figure 7 shows the EFW data during one spin together with the photoelectron and wake fields.

Performing the Fourier analysis for a number of subsequent spins, we can see how the wake direction changes with time (see Figure 8(a)), but also investigate relations between the satellite potential and the wake field (see Figure 8(b)). As can be seen in Figure 8(a), the direction of the wake in the spin plane is almost anti-parallel with the magnetic field component in the spin plane, which is expected for small perpendicular electric fields implying a plasma flow mostly along the magnetic field. Figure 8(b) gives the ratios $a_{\rm w3}/a_{\rm w1}$ and $a_{\rm w5}/a_{\rm w1}$ as a function of the satellite potential. Both ratios tend to decrease as the satellite potential increases, which confirms the model with an enhanced wake created by potential structures around the satellite: for large potentials the wake grows bigger and the double-probe signal becomes more sinusoidal.
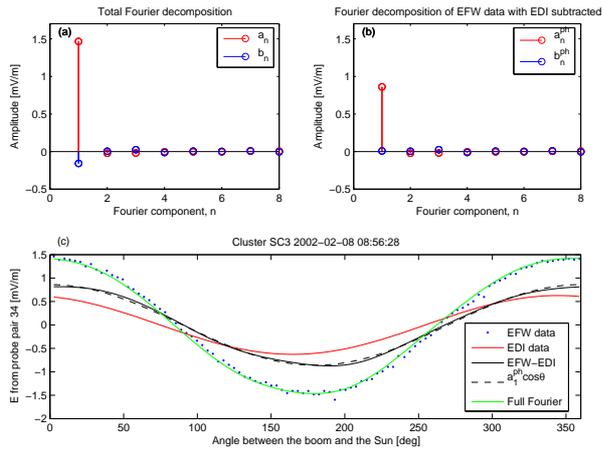
Fig. 4. Fourier decomposition of one spin from 2002-02-08 08:56:28 for probe pair 34 on spacecraft 3. Panel (a) shows the complete decomposition of the spin, while panel (b) displays the Fourier decomposition with the background electric field from EDI subtracted. In panel (c) the data (blue dots) is shown together with the complete Fourier decomposition (green), the EDI field (red), the resulting field from (b) (solid black) and $E_a^0 \cos \theta$ (dashed black).
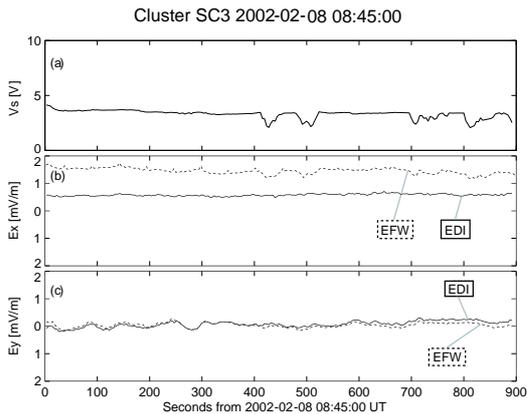
Fig. 5. EFW (dashed) and EDI (solid) data in the satellite reference system during 920 s from 2002-02-08 08:45:00. (a) Satellite potential, V_{sc}. (b) x component of electric field data from EFW and EDI. (c) y component of electric field from EFW and EDI.

IV. DISCUSSION

This study has shed new light on double-probe instruments, such as Cluster EFW, operating in cold tenuous plasmas, where the main error sources in the electric field measurements are due to asymmetric photoemission and spacecraft wakes. For the apparent sunward field, a more extensive study would be rewarding to establish a reliable dependence on the satellite potential, since it could be used to adjust EFW data. Each probe pair on all four spacecraft should then be examined separately, as the photoemission varies between the probe pairs. For the wake field, there are more yet unrevealed relations to investigate further: How does the angle of the flow out of the spin plane affect the wake signature? How do the Fourier components
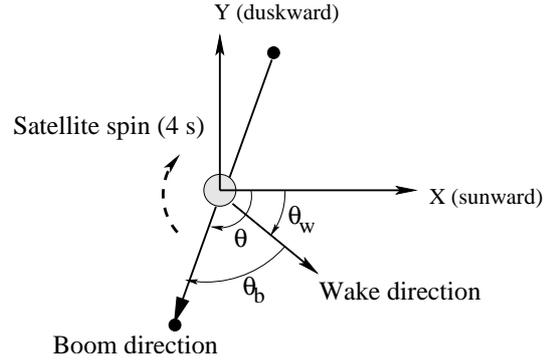
Fig. 6. Angles in the spacecraft spin plane: θ_b – angle between the boom and the direction of the wake flow, θ_w – angle between the positive X_{GSE} direction and the wake, θ – angle between the positive X_{GSE} direction and the boom.
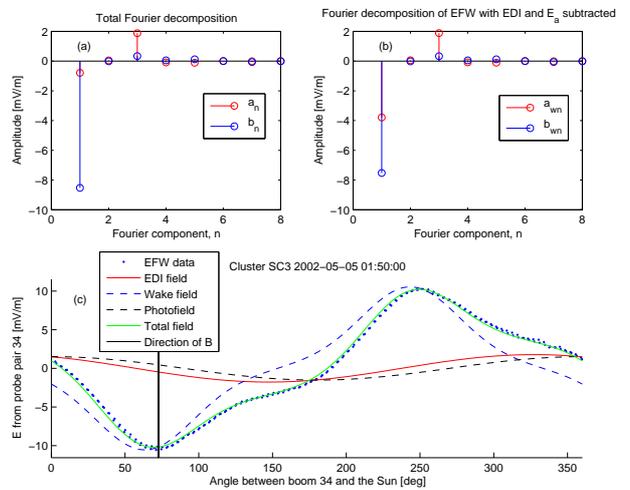
Fig. 7. Fourier decomposition of one spin for wake affected EFW data from 2002-05-05 01:50:00 for probe pair 34 on spacecraft 3. Panel (a) shows the complete decomposition of the spin, while panel (b) displays the Fourier decomposition with the background electric field from EDI and the sunward offset field subtracted. In panel (c) the data (blue) is shown together with the complete Fourier decomposition (red), the EDI field (blue), $E_a^0 \cos \theta$ (black), and the wake field (green).

of the wake signatures depend on satellite potential and plasma parameters? Could the wake signatures be used to derive other plasma parameters, such as electron and ion temperature?

Future studies could be divided into two important subdomains:

a) Removal of spurious fields in EFW data: If we get full knowledge of the spurious electric fields, they could be removed from EFW data and we would have reliable information on the electric field even without any EDI data. This requires that we can determine the dependence of the photofield on satellite potential, as well as establish a relation between the wake Fourier components and scaling parameters, such as satellite potential and plasma properties. At this stage, we are only able to identify spurious wake fields: if we find double-probe signatures with
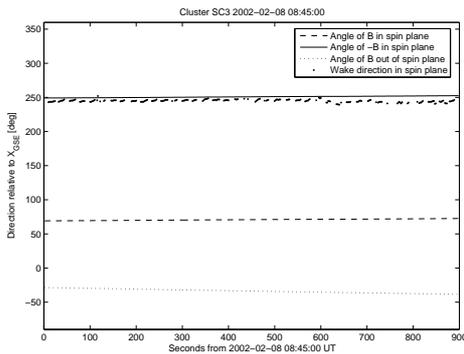
(a)
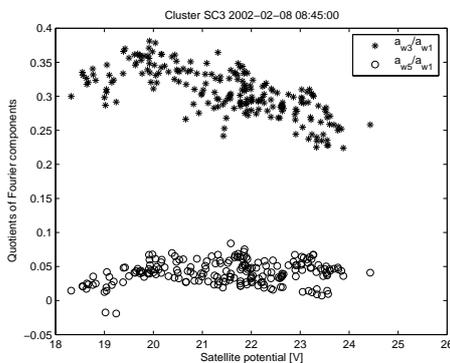
(b)

Fig. 8. (a) Angles versus time: Derived angles of the wake (points), $\alpha = 360° - \wedge(X_{\mathrm{GSE}}, \mathbf{B})$ in spin plane (dashed), $\alpha + 180°$ (solid), and elevation angle of $\mathbf{B}$ out of the spin plane (dotted). (b) Dependence of the wake Fourier components on the satellite potential. Stars corresponds to $a_{\mathrm{w3}}/a_{\mathrm{w1}}$, while circles represents $a_{\mathrm{w5}}/a_{\mathrm{w1}}$.

higher frequencies than the fundamental in the Fourier decomposition, we can suspect that a wake has formed and thus treat the data with care.

b) Information about cold ions: As described in section II-B, the simulations together with data analysis from different instruments on Cluster could be used to derive properties of the wake. A first example can be found in [15], where the ion flow speed is calculated from the wake field.

V. CONCLUSIONS

The main conclusions of the current study are:

1) We have shown that the sunward photoelectron field contaminating double-probe measurements is sinusoidal: $E_{\mathrm{a}}(\theta) = E_{\mathrm{a}}^0 \cos \theta$.
2) An enhanced wake forms downstream of a spacecraft in a flowing plasma, when the condition $KT_{\mathrm{i}} < E_{\mathrm{k}}^{\mathrm{i}} < eV_{\mathrm{s}}$ is satisfied. Such a wake will affect a double-probe electric field instrument significantly.

3) By Fourier analysis of the disturbed EFW signal, it is possible to determine the angle, width and depth of the wake.
4) The model for the wake field, $E_{\mathrm{w}} = a_{\mathrm{w1}} \cos \theta_{\mathrm{b}} + a_{\mathrm{w3}} \cos(3\theta_{\mathrm{b}}) + a_{\mathrm{w5}} \cos(5\theta_{\mathrm{b}})$, is consistent with data.
5) Simulations with PicUp3D have given more information on the enhanced wake formation and has permitted to quantify the effect on the double-probe electric field instrument, assuming that the probes perfectly couple to the plasma. The magnitude as well as the spin dependence of the wake field is in good agreement with Cluster data. These simulations together with data analysis, can in principle be used to derive properties of the cold ion flow.

VI. ACKNOWLEDGEMENTS

REFERENCES

[1] A. Pedersen, C. A. Cattell, C.-G. Fälthammar, V. Formisano, P.-A. Lindqvist, F. Mozer, and R. Torbert, "Quasistatic electric field measurements with spherical double probes on the GEOS and ISEE satellites," *Space Science Reviews*, vol. 37, pp. 269–312, 1984.
[2] L. P. Block, C.-G. Falthammar, P.-A. Lindqvist, G. Marklund, F. S. Mozer, A. Pedersen, T. A. Potemra, and L. J. Zanetti, "Electric field measurements on Viking: first results," *Geophys. Res. Lett.*, vol. 14, p. 435, 1987.
[3] G. Marklund, L. G. Blomberg, P.-A. Lindqvist, C.-G. Fälthammar, G. Haerendel, F. Mozer, A. Pedersen, and P. Tanskanen, "The double probe electric field experiment on Freja: Experiment description and first results," *Space Sci. Rev.*, vol. 70, pp. 483–508, 1994.
[4] K. Tsuruda, H. Hayakawa, M. Nakamura, T. Okada, A. Matsuoka, F. S. Mozer, and R. Schmidt, "Electric field measurements on the GEOTAIL satellite," *Journal of Geomagnetism and Geoelectricity*, vol. 46, pp. 693–711, 1994.
[5] P. Harvey, F. S. Mozer, D. Pankow, J. Wygant, N. C. Maynard, H. Singer, W. Sullivan, P. B. Anderson, R. Pfaff, T. Aggson, A. Pedersen, C.-G. Fälthammar, and P. Tanskanen, "The electric field instrument on the Polar satellite," *Space Sci. Rev.*, vol. 71, pp. 583–596, 1995.
[6] R. E. Ergun, C. W. Carlson, F. S. Mozer, G. T. Delory, M. Temerin, J. P. McFadden, D. Pankow, R. Abiad, P. Harvey, R. Wilkes, H. Primbsch, R. Elphic, R. Strangeway, R. Pfaff, and C. A. Cattell, "The FAST Satellite Fields Instrument," *Space Science Reviews*, vol. 98, pp. 67–91, Aug. 2001.
[7] A. Pedersen, F. Mozer, and G. Gustafsson, "Electric field measurements in a tenuous plasma with spherical double probes," in *Measurement Techniques in Space Plasmas: Fields*, ser. Geophysical Monograph 103. American Geophysical Union, 1998, pp. 1–12.
[8] N. C. Maynard, "Electric field measurements in moderate to high density space plasmas with passive double probes," in *Measurement Techniques in Space Plasmas: Fields (AGU Geophysical Monograph 103)*, J. Borovsky, R. Pfaff, and D. Young, Eds. American Geophysical Union, 1998, pp. 13–27.
[9] G. Gustafsson, M. André, T. Carozzi, A. I. Eriksson, C.-G. Fältham-mar, R. Grard, G. Holmgren, J. A. Holtet, N. Ivchenko, T. Karlsson, Y. Khotyaintsev, S. Klimov, H. Laakso, P.-A. Lindqvist, B. Lybekk, G. Marklund, F. Mozer, K. Mursula, A. Pedersen, B. Popielawska, S. Savin, K. Stasiewicz, P. Tanskanen, A. Vaivads, and J.-E. Wahlund, "First results of electric field and density observations by Cluster EFW based on initial months of operation," *Annales Geophysicae*, vol. 19, pp. 1219–1240, 2001.

[10] A. Eriksson, M. André, B. Klecker, H. Laakso, P.-A. Lindqvist, F. Mozer, G. Paschmann, A. Pedersen, J. Quinn, R. Torbert, K. Torkar, and H. Vaith, "Electric field measurements on Cluster: Comparing the double-probe and electron drift technique," *Annales Geophysicae*, 2006, in press.

[11] G. Paschmann, J. M. Quinn, R. B. Torbert, H. Vaith, C. E. McIlwain, G. Haerendel, O. H. Bauer, T. Bauer, W. Baumjohann, W. Fillius, M. Förster, S. Frey, E. Georgescu, S. S. Kerr, C. A. Kletzing, H. Matsui, P. Puhl-Quinn, and E. C. Whipple, "The Electron Drift Instrument on Cluster: overview of first results," *Annales Geophysicae*, vol. 19, pp. 1273–1288, 2001.

[12] E. Engwall, A. I. Eriksson, and J. Forest, "Wake formation behind positively charged spacecraft in flowing tenuous plasmas," *Physics of Plasmas*, 2006, in review.

[13] C. M. Cully and R. E. Ergun, "A quantitative look at double-probe electric field measurements," 2005, manuscript in preparation.

[14] J. Forest, L. Eliasson, and A. Hilgers, "A new spacecraft plasma simulation software, PicUp3D/SPIS," in 7th *Spacecraft Charging Technology Conference*, vol. SP-476. ESA, 2001, pp. 515–520.

[15] E. Engwall, A. I. Eriksson, M. André, I. Dandouras, G. Paschmann, J. Quinn, and K. Torkar, "Low-energy (order 10 ev) ion flow in the magnetotail inferred from spacecraft wake observations," *Geophysical Research Letters*, 2006, accepted.

[16] P. M. E. Décréau, P. Fergeau, V. Krasnoselskikh, E. Le Guirriec, M. Lévêque, P. Martin, O. Randriamboarison, J. L. Rauch, F. X. Sené, H. C. Séran, J. G. Trotignon, P. Canu, N. Cornilleau, H. de Féraudy, H. Alleyne, K. Yearby, P. B. Mögensen, G. Gustafsson, M. André, D. C. Gurnett, F. Darrouzet, J. Lemaire, C. C. Harvey, P. Travnicek, and Whisper experimenters, "Early results from the WHISPER instrument on Cluster: an overview," *Annales Geophysicae*, vol. 19, pp. 1241–1258, 2001.

[17] Y.-J. Su, J. L. Horwitz, T. E. Moore, B. L. Giles, M. O. Chandler, P. D. Craven, M. Hirahara, and C. J. Pollock, "Polar wind survey with the Thermal Ion Dynamics Experiment/Plasma Source Instrument suite aboard POLAR," *Journal of Geophysical Research*, vol. 103, pp. 29 305–29 337, 1998.

[18] A. Pedersen, R. Grard, K. Knott, D. Jones, A. Gonfalcone, and U. Fahleson, "Measurements of quasi-static electric fields between 3 and 7 Earth radii on Geos-1," *Space Science Reviews*, vol. 22, pp. 333–346, 1978.

Paper III

Low-energy (order 10 eV) ion flow in the magnetotail lobes inferred from spacecraft wake observations

E. Engwall,[1, 2] A. I. Eriksson,[2] M. André,[2] I. Dandouras,[3] G. Paschmann,[4] J. Quinn,[5] and K. Torkar[6]

Cold ionospheric ions with eV energies are common in the magnetosphere and can travel far out in the magnetotail. However, they are difficult to measure with conventional ion spectrometers mounted on spacecraft, since the potential of a sunlit spacecraft often reaches several tens of volts. In this paper we present two alternative methods of measuring the cold-ion flow with the Cluster spacecraft and apply them on one case in the magnetotail at 18 R_E: 1. Ion spectrometer in combination with artificial spacecraft potential control; 2. Deriving ion flow velocity (both perpendicular and parallel) from electric field instruments. The second method takes advantage of the effect on the double-probe instrument of the wake formed behind a spacecraft in a plasma flow. The results from the two methods show good agreement and are also consistent with polar wind models and previous measurements at lower altitudes, confirming the continuation of low-energy ion outflows.

1. Introduction

Cold ions with kinetic energies of a few to tens of eV are injected into the terrestrial magnetosphere through ion outflow processes from the ionosphere. From theoretical estimates supported by observations in combination with simulations, *Chappell et al.* [1987, 2000] have shown that the ionospheric outflows could be the dominant source of plasma supply to the magnetosphere.

Cold plasma of ionospheric origin is therefore common in the magnetosphere, including the magnetotail lobes. However, due to the very low densities in the lobes, the spacecraft potential, V_{sc}, usually is several tens of volts positive, so that ions below the corresponding energy in eV cannot reach the onboard particle detectors. When the ions are accelerated to energies above eV_{sc}, e.g. by the plasma motion of the Pc 5 wave events observed with Geotail [*Hirahara et al.*, 2004], or by convection and associated centrifugal acceleration, they become visible onbord spacecraft. In the tail, this has allowed a wealth of investigations like the plasma sheet injection studies using data from ISEE [*Orsini et al.*, 1990], Geotail [*Seki et al.*, 2002] and Cluster [*Sauvaud et al.*, 2004] data, to mention just a few: the reader is refered to these works for further references.

While there thus is a substantial literature concerning the flow in the magnetotail of cold ions with a total energy above about 50 eV, relatively little is known about the population at very low energies, around a few tens of eV or less. Special circumstances sometimes allow such ions to be seen. Early measurements with the ISEE spacecraft [*Etcheto and Saint-Marc*, 1985] found an "anomalously" high plasma density in the plasma sheet boundary layer revealed by a relaxation sounder. Since then, other event studies have provided evidence of what *Olsen* [1982] termed the "hidden" cold-ion population in the geomagnetic tail. *Seki et al.* [2003] reported very low-energy ions in the deep tail plasma sheet observed on the Geotail spacecraft. At the time of observation the spacecraft was in eclipse, resulting in a negative spacecraft potential allowing ions at any energy to reach the detectors on the satellite. Nevertheless, only by artificially regulating the potential of the Polar satellite has it been possible to gather significant statistics on ions at or below a few tens of eV, presented by *Moore et al.* [1997] and *Su et al.* [1998] in their studies of ionospheric cold plasma flows out to 8 R_E. To our knowledge, no study has been able to establish the flow properties of ions below some 50 eV further out than the Polar apogee at 8 R_E.
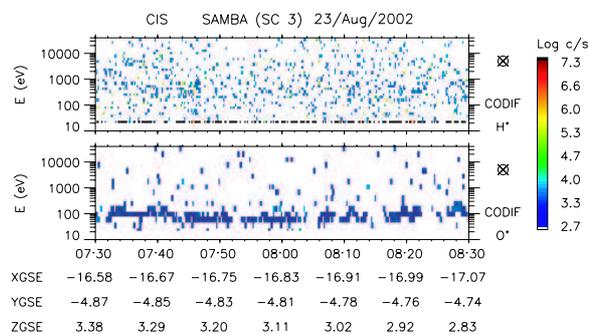
Figure 1. CODIF data from Cluster SC3: 8/23/2002 $07:30 - 08:30$. CODIF has detected an O^+ ion beam, in the anti-sunward direction (essentially in the direction of the magnetic field). The satellite potential (see Figure 2) is too high for the detection of the H^+ ions which have typical energies around 10 eV. The thin stripe around the lowest energy in the proton data is an artefact from onboard data compression.

In this paper we present a case study of cold ions in the magnetotail with Cluster. The protons are so low in energy that they are only detectable with the onboard ion spectrometer CIS when the artificial spacecraft potential control (ASPOC) is activated, and even then most of the population is hidden from CIS. However, these ions can simultaneously

---

[1]Department of Astronomy and Space Physics, Uppsala University, Uppsala, Sweden.

[2]Swedish Institute of Space Physics, Uppsala, Sweden.

[3]Centre d'Etude Spatiale des Rayonnements/Centre National de la Recherche Scientifique, ToulouseNRS, Toulouse, France.

[4]International Space Science Institute, Bern, Switzerland.

[5]Space Science Center, University of New Hampshire, Durham, NH, USA.

[6]Space Research Institute of the Austrian Academy of Science, Graz, Austria.

be indirectly detected with the electric field instruments, EFW and EDI, from the wake formed behind another of the four Cluster spacecraft. We first show evidence for cold-ion flows in both ion and electric field data, and then derive the flow properties from these data.

2. Analysis of Particle Data

CIS consists of two different instruments: the mass-separating instrument CODIF, which was used in this study, and the hot-ion analyzer, HIA [*Rème et al.*, 2001]. Figure 1 shows CODIF data from spacecraft 3 (henceforth denoted SC3) collected during 1 hour, when the Cluster spacecraft are around [-17, -3, 5] R_E GSM, i.e. in the northern lobe of the geomagnetic tail. The CODIF data show no outflowing protons, but a distinct 100 eV (relative to the spacecraft potential) cold oxygen flow directed mainly anti-parallel to the magnetic field ($\mathbf{B} \approx [37, 1, 7]$ nT in GSE coordinates). As can be seen in Figure 2, the satellite potential on SC3 varies between 40 V and over 60 V, making it impossible for CODIF to detect any ions at lower energies. As a result, the plasma densities inferred from the HIA (Figure 2(b), solid lines) are much lower than the plasma density derived from the spacecraft potential by the method of *Pedersen et al.* [2001] (Figure 2(b), dashed line). On SC4 ASPOC [*Torkar et al.*, 2001] is operating reducing the spacecraft potential to 7 V and the data thus reveal a population of cold H^+ ions. In addition, CODIF on SC4 is in retarding potential analyzer (RPA) mode, making it possible to measure low energies (0.7-25 eV) with high resolution [*Dandouras*, 2005]. We assumed that the plasma properties were constant over spacecraft separation distances of typically 3400 km (on field lines around 3000 km).
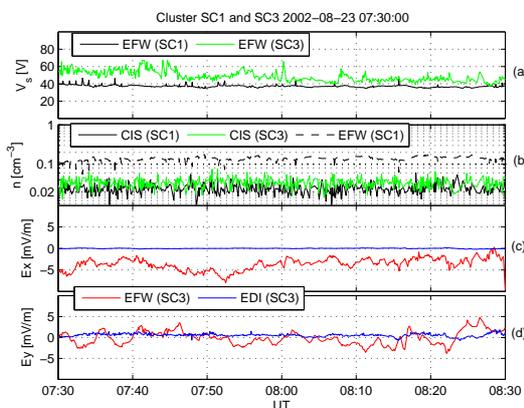
Figure 2. Data from Cluster SC1 and SC3: 8/23/2002 07:30 – 08:30. (a) Spacecraft potential derived from EFW. (The spacecraft potential is higher on SC3 than on SC1 due to the operation of EDI on SC3.) (b) HIA density measurements together with the density estimated from the spacecraft potential on SC1 according to *Pedersen et al.* [2001]. (c), (d) Electric field measurements.

Figure 3 shows the distribution function from SC4 for H^+ in the GSE $v_x - v_z$-plane ($v_y = 0$). The distribution function has been corrected for the spacecraft potential of 7 V, since CODIF measures the energy of the ions relative to the spacecraft potential. From the figure we see that the hydrogen flow is aligned with the magnetic field, and has a velocity of 40 km/s (corresponding to 9 eV flow energy).

The oxygen flow has too high an energy to be measured by CODIF on SC4 (in RPA mode), and was therefore determined from the distribution function on SC3. After correction for the 40-60 V spacecraft potential, we obtained a flow velocity with an anti-sunward component of around 30 to 35 km/s (v_z is not reliable due to anode problems on SC3, and we therefore disregarded this component; and v_y fluctuates around 0 km/s).
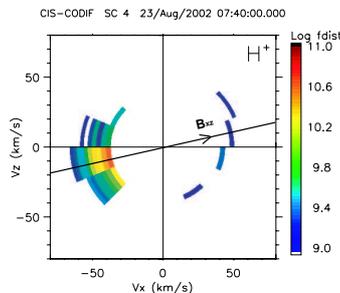
Figure 3. The distribution function for H^+ cut in the $v_x - v_z$-plane for $v_y = 0$, averaged over 75 spins from 07:40 to 07:45 on SC4. The velocities have been corrected for the spacecraft potential of 7 V. The lowest velocities are missing due to the instrument low-energy cutoff at 0.7 eV. $\mathbf{B}_{xz}$ is the magnetic field projected in the $x - z$-plane.

3. Analysis of Electric Field Data

Evidence of cold flowing ions can also be found in electric field data from SC3 for the same event. Cluster carries two instruments for measurements of electric fields using different techniques: the double-probe instrument EFW [*Gustafsson et al.*, 1997] and the electron drift instrument EDI [*Paschmann et al.*, 1997]. The difference between the EDI and EFW data, which can be seen in Figure 2(c) and (d), is due to a potential created in a wake behind the spacecraft.

A wake will form behind a spacecraft for supersonic ion flows, i.e. $W_i > KT_i$, where W_i is the bulk ion flow energy and KT_i the thermal energy. If, in addition, the plasma is sufficiently tenuous, the spacecraft potential will exceed the ion flow energy, resulting in $eV_s > W_i > KT_i$. This creates an enhanced wake, since in this case the ions are deflected by the potential structures around the spacecraft [*Eriksson et al.*, 2006]. For Debye lengths greater than the spacecraft dimensions the wake can be significantly enlarged, as has been verified by particle-in-cell simulations [*Engwall*, 2004; *Engwall and Eriksson*, 2006]. Figure 4 shows schematically the wake formation in supersonic flows. In the case of an enhanced wake the ion density will be largely depleted behind the spacecraft. The ion wake will, to a large extent, be filled with subsonic electrons, creating a negative potential in the wake. The EFW probes, which are mounted on 44 m wire booms (probe-to-probe separation 88 m), will observe this negative potential, while the keV electron beam from EDI is unaffected.
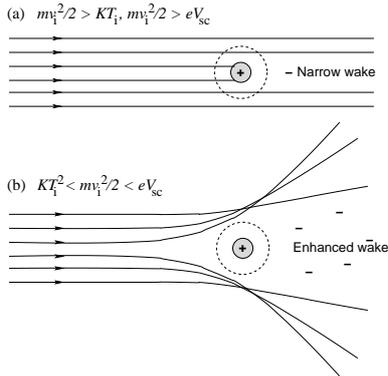
Figure 4. Sketch of wake formation in supersonic flows. (a) Narrow wake. (b) Enhanced wake.

The wake can provide the plasma flow speed through the application of a simple model. We assume that the ions are unmagnetized on the wake length scale, so that the wake field measured by EFW is in the flow direction. Then, $\mathbf{E}^{\mathrm{w}} = \mathbf{E}^{\mathrm{EFW}} - \mathbf{E}^{\mathrm{EDI}} = g\mathbf{u}$, where $\mathbf{u}$ is the flow velocity and the scalar g may be a function of, for example, V_{s}, T_{i} and the flow speed u, but should be independent of the flow direction. Decomposing the components of $\mathbf{u}$, we obtain:

$$\mathbf{E}^{\mathrm{w}} = g\mathbf{u}_{\perp} + gu_{\parallel}\frac{\mathbf{B}}{B}, \qquad (1)$$

where $\mathbf{u}_{\perp}$ is known from EDI data, $\mathbf{u}_{\perp} = \mathbf{E}^{\mathrm{EDI}} \times \mathbf{B}/B^2$. Since $\mathbf{E}^{\mathrm{w}}$ has two measured components, we have two equations for the two unknowns g and $u_{\parallel}$:

$$\begin{cases} g = \dfrac{(\mathbf{B} \times \mathbf{E}^{\mathrm{w}})_z}{E_z^{\mathrm{EDI}}} = \dfrac{B_x E_y^{\mathrm{w}} - B_y E_x^{\mathrm{w}}}{E_z^{\mathrm{EDI}}} \\[2ex] u_{\parallel} = \dfrac{\mathbf{B} \cdot \mathbf{E}^{\mathrm{w}}}{gB} = \dfrac{E_x^{\mathrm{w}} B_x + E_y^{\mathrm{w}} B_y}{B_x E_y^{\mathrm{w}} - B_y E_x^{\mathrm{w}}}\dfrac{E_z^{\mathrm{EDI}}}{B} \end{cases} \qquad (2)$$

When calculating g special care has to be taken for values of E_z^{EDI} approaching zero. In the analysis, we have removed the points for calculated values of g and $u_{\parallel}$ where $E_z^{\mathrm{EDI}} < 0.05$ mV/m.

We can not apply our model to electric field data from SC4 for this event, since ASPOC reduces the spacecraft potential below the ion flow energy, thereby removing the wake. Instead, we used the electric field data from SC3 (Figure 2(c)-(d)), giving an anti-parallel velocity ranging between approximately 20 and 30 km/s (see Figure 5).

The perpendicular drift velocity is the same for all ion species, when the "frozen-in" condition applies. While the parallel velocity of different ion species should be the same if centrifugal acceleration is dominating [*Cladis*, 1986], other energization processes may lead to parallel velocity depending on particle mass. In this case, u_{par} must be interpreted as a weighted average of the parallel velocities of the different particle species. The weighting will be in favour of the lighter species since they are more affected by the spacecraft potential due to their lower energy and hence more effective for creating the wake. In a case like in Figure 1, where the oxygen ions are sufficiently energetic to reach the ion detectors on the spacecraft, they obviously do not contribute to the wake and the derived u_{par} in 2 is the parallel velocity of the protons.

The parallel flow velocity derived from the electric fields should therefore be compared to the H^+ velocity from

CODIF on SC4. It is not possible to compare the two methods on the same spacecraft, as either V_{s} is low, so that the ions can be measured by the particle detectors, but no wake is formed, or V_{s} is high, in which case we can derive the flow velocity from the wake observed by the electric field instruments, but the ions are prevented from reaching the CODIF detectors. Comparing the two derived velocities from SC3 and SC4 (panels (b) and (c) in Figure 5), we see that the mean value and the size of the variations show good agreement, although details of course differ between the two spacecraft.
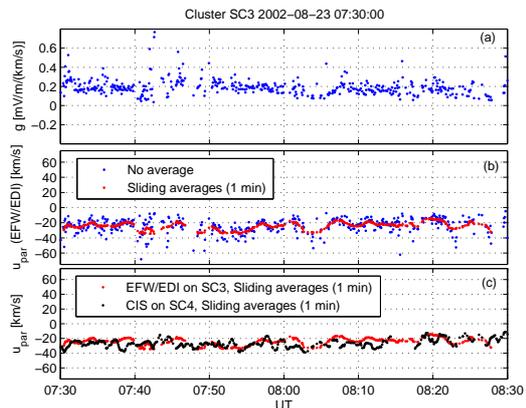
Figure 5. Flow velocities of H^+ from electric field instruments on SC3 and from ion spectrometers on SC4. Panels (a) and (b) show the two derived quantities from the wake behind SC3: g relates the parallel flow velocity, $u_{\parallel}$ to the wake field. $u_{\parallel}$ is consistent with the corrected H^+ flow velocity obtained from CODIF on SC4 (panel (c)). The negative sign corresponds to an outflow, since the spacecraft are in the northern hemisphere. Data have been smoothed by a 1 minute sliding average filter.

4. Discussion and Conclusions

We have used Cluster data to study the cold plasma in the northern lobe of the terrestrial magnetotail for one event using two different methods. One method employs a particle detector, CODIF, whose range of accessible energies was extended down to around 7 eV by using the artificial spacecraft potential control ASPOC. Only when ASPOC was activated, and by running the CODIF detector in RPA mode, it was possible to measure the cold flowing protons. The cold flowing O^+ ions with much higher energy could also be detected on the Cluster satellites where ASPOC was not operating.

The other method we developed to study the cold-ion flow at locations where it is inaccessible to ordinary particle instruments exploits the fact that a wake forms behind a spacecraft in a supersonic ion flow, and that this wake can be observed by the double-probe electric field instrument EFW. The electron drift instrument EDI observes the unperturbed electric field, and the two instruments together can then provide the direction of the wake, and hence of the flow. We can also calculate the full flow speed, including its parallel component. Comparison to the flow derived from particle data shows very good agreement.

As the wake method only works in situations where the flowing ions are deflected by the spacecraft potential before reaching the spacecraft and hence cannot be detected by a

particle detector, it is intrinsically impossible to use the two methods simultaneously on the same spacecraft. However, thanks to the particular configuration of the Cluster spacecraft (ASPOC activated and CODIF in RPA mode on SC4, ASPOC off and EDI on for SC3) in this particular event, it was possible to compare the results of the two methods on two different spacecraft. Events where such a comparison can be made are rare: in fact, we found only a couple of other events when scanning the complete Cluster database of the tail lobes beyond 5 R_E, from June 2001 through September 2004, where the instrument setup as well as the geophysical setting (presence of low-energy ions) was suitable. Nevertheless, the presented event is sufficient to establish that the new method of cold plasma flow detection by observation of the spacecraft wake actually works, and that it can be used in future studies.

The flow measurements obtained with both methods at 18 R_E are in accordance with the polar wind flow properties measured using the Polar satellite at 8 R_E by *Su et al.* [1998], although our event appears to show an unusually high oxygen flow speed. Geotail was used to observe cold plasma in the central plasma sheet at and beyond our location at 18 R_E [*Seki et al.*, 2003] and has also provided a wealth of observations on cold plasmas flowing at energies of several hundreds eV and above. However, our event is the first velocity measurement of low-energy plasma flows beyond 8 R_E. While we cannot directly measure the ion temperature, the fact that a wake is observed shows that the ion flow is supersonic, so that the temperature must be below the flow kinetic energy. As the derived drift speed of 20-40 km/s in Figure 5 corresponds to a proton flow energy 2-8 eV, the proton temperature must be of the order of 1 eV or less for a wake to be created. Plasmas with these low temperatures could only originate from the ionosphere and we thus show the continuation of the cold ionospheric outflows studied by *Su et al.* [1998] at 8 R_E to at least 18 R_E.

Our main conclusions are:

1. Low-energy (order 10 eV) ion outflows with general properties as observed at 8 R_E in previous studies extend to at least 18 R_E.

2. Data from double-probe and electron drift instruments can be combined with a simple model for the wake behind a spacecraft to estimate the flow velocity (magnitude and direction) of a tenuous, supersonic plasma flow.

References

Chappell, C. R., T. E. Moore, and J. H. Waite, The ionosphere as a fully adequate source of plasma for the Earth's magnetosphere, *J. Geophys. Res.*, *92*(11), 5896–5910, 1987.

Chappell, C. R., et al., The adequacy of the ionospheric source in supplying magnetospheric plasmas, *Journal of Atmospheric and Solar-Terrestrial Physics*, *62*, 421–436, 2000.

Cladis, J. B., Parallel acceleration and transport of ions from polar ionosphere to plasma sheet, *Geophys. Res. Lett.*, , *13*, 893–896, 1986.

Dandouras, I., et al., Multipoint observations of ionic structures in the plasmasphere by CLUSTER-CIS and comparisons with IMAGE-EUV observations and with model simulations, *Yosemite 2004 AGU Monograph: Global Physics of the Coupled Inner Magnetosphere*, in press, 2005.

Engwall, E., Numerical studies of spacecraft-plasma interaction: Simulations of wake effects on the Cluster electric field instruments EFW, *IRF Scientific Report 284*, Swedish Institute of Space Physics, 2004.

Engwall, E., and A. I. Eriksson, Double-probe measurements in cold flowing tenuous space plasmas, *IEEE Trans. Plasma Sci.*, in review, 2006.

Eriksson, A., et al., Electric field measurements on cluster: Comparing the double-probe and electron drift technique, *Annales Geophysicae*, in press, 2006.

Etcheto, J., and A. Saint-Marc, Anomalously high plasma densities in the plasma sheet boundary layer, *J. Geophys. Res.*, *90*, 5338–5344, 1985.

Gustafsson, G., et al., The Electric Field and Wave Experiment for the Cluster Mission, *Space Science Reviews*, *79*, 137–156, 1997.

Hirahara, M., K. Seki, Y. Saito, and T. Mukai, Periodic emergence of multicomposition cold ions modulated by geomagnetic field line oscillations in the near-Earth magnetosphere, *J. Geophys. Res.*, *109*, 2004.

Moore, T. E., et al., High-altitude observations of the polar wind, *Science*, *277*, 349–351, 1997.

Olsen, R. C., The hidden ion population of the magnetosphere, *J. Geophys. Res.*, *87*, 3481–3488, 1982.

Orsini, S., M. Candidi, M. Stockholm, and H. Balsiger, Injection of ionospheric ions into the plasma sheet, *J. Geophys. Res.*, , *95*, 7915–7928, 1990.

Paschmann, G., et al., The Electron Drift Instrument for Cluster, *Space Science Reviews*, *79*, 233–269, 1997.

Pedersen, A., et al., Four-point high time resolution information on electron densities by the electric field experiments (EFW) on Cluster, *Annales Geophysicae*, *19*, 1483–1489, 2001.

Rème, H., et al., First multispacecraft ion measurements in and near the Earth's magnetosphere with the identical Cluster ion spectrometry (CIS) experiment, *Annales Geophysicae*, *19*, 1303–1354, 2001.

Sauvaud, J.-A., et al., Case studies of the dynamics of ionospheric ions in the Earth's magnetotail, *J. Geophys. Res.*, *109*, 2004.

Seki, K., et al., A new perspective on plasma supply mechanisms to the magnetotail from a statistical comparison of dayside mirroring O^+ at low altitudes with lobe/mantle beams, *J. Geophys. Res. (Space Physics)*, *107*, 7–1, 2002.

Seki, K., et al., Cold ions in the hot plasma sheet of Earth's magnetotail, *Nature*, *422*, 589–591, 2003.

Su, Y.-J., J. L. Horwitz, T. E. Moore, B. L. Giles, M. O. Chandler, P. D. Craven, M. Hirahara, and C. J. Pollock, Polar wind survey with the Thermal Ion Dynamics Experiment/Plasma Source Instrument suite aboard POLAR, *J. Geophys. Res.*, *103*, 29,305–29,337, 1998.

Torkar, K., et al., Active spacecraft potential control for Cluster - implementation and first results, *Annales Geophysicae*, *19*, 1289–1302, 2001.

E. Engwall, Department of Astronomy and Space Physics, Uppsala University, Sweden. (Erik.Engwall@irfu.se)